Astronomy Letters, Vol. 31, No. 11, 2005, pp. 713–728. Translated from Pis'ma v Astronomicheskiĭ Zhurnal, Vol. 31, No. 11, 2005, pp. 803–818.

On the Content of Cold Electrons in Blazar and Microquasar Jets

V. V. Zheleznyakov and S. A. Koryagin*

Institute of Applied Physics, Russian Academy of Sciences, ul. Ul'yanova 46, Nizhni Novgorod, 603950 Russia

Received May 5, 2005

Abstract—We explore the possibility of determining the corpuscular composition of the plasma in the relativistic jets of blazars and microquasars from data on the polarization and intensity of their radio synchrotron emission. We have constructed a universal diagram that allows the relative content of nonrelativistic electrons to be established in specific objects using information about their frequency spectra and polarization at individual frequencies. As a result, we have found that the electron plasma component in the jets of the blazars 3C 279 and BL Lac is relativistic. In the jets of the microquasar GRS 1915+105, the cold plasma density may be comparable to or considerably higher than the relativistic particle density.
© *2005 Pleiades Publishing, Inc.*

Key words: *jet theory; active galactic nuclei, quasars, and radio galaxies.*

1. INTRODUCTION

The electromagnetic radiation from active galactic nuclei (AGNs) accounts for a sizeable proportion of or even exceeds the level of radiation from the rest of the galaxy. Quasars, BL Lacertae objects, and Seyfert and radio galaxies belong to AGNs. Blazars, including BL Lac objects (Lacertids) and flat-spectrum radio-loud quasars (Urry and Padovani 1995), are particularly distinguished among AGNs. Blazars exhibit intense continuum emission from the radio to X-ray and gamma-ray ranges. The radio emission from these objects is attributable to the synchrotron radiation of relativistic particles. High-angular-resolution radio observations of blazars have revealed collimated jets in them, in which matter moves away from the core at speeds close to the speed of light. The latter causes the brightness of the jet moving toward the observer to increase compared to its rest-frame brightness. In our Galaxy, microquasars, X-ray binaries in which matter is ejected in the form of jets, constitute a smaller-scale analogue of quasars. Superluminal motion is also detected in microquasar jets, although the angle between the jet axis and the line of sight is not always small as in observed blazars.

One of the outstanding problems in the theory of jets is the corpuscular composition of their plasma: an ordinary electron–proton plasma or an electron–positron plasma. This problem stems from the fact that the jets are formed close to a black hole. The matter accreting onto a black hole may be processed in its neighborhood and ejected with a different corpuscular composition than in the accretion disk. The solution of the problem is of great importance in elucidating the jet formation mechanism.

The presence of positrons in a jet can be evidenced by the gamma-ray electron–positron annihilation line. Annihilation was considered as a possible radiation mechanism of the so-called MeV blazars, in which the bulk of the radiation is emitted at photon energies of the order of several MeV (Bloemen *et al.* 1995; Blom *et al.* 1995; Boettcher and Schlickeiser 1996; Skibo *et al.* 1997). However, the radiation from the MeV blazars can also be explained in terms of the inverse Compton model (Sikora *et al.* 2002). The latter approach combines the MeV blazars with a larger class of blazars in which the bulk of the energy is emitted at ∼1 GeV. At the same time, the annihilation line can be masked by the bremsstrahlung of electron–positron pairs at certain jet parameters (Boettcher and Schlickeiser 1995; Kaiser and Hannikainen 2002).

The intense continuum emission from the jets of blazars masks their atomic spectral lines. The detection of spectral lines is also complicated by their Doppler broadening and frequency shift. In contrast, pairs of narrow hydrogen and iron lines are clearly seen in the optical and X-ray spectra of the microquasar SS 433 (Margon 1984; Kotani *et al.* 1994; Fender *et al.* 2003). These lines are associated with the approaching and receding (from the observer) jets, whose emission is shifted in frequency due to the Doppler effect. The presence of these spectral lines is indicative of a normal plasma composition in the jets

*E-mail: koryagin@appl.sci-nnov.ru

of the microquasar SS 433. However, no similar lines have been observed in other microquasars so far.

An alternative solution of the fundamental problem of the corpuscular composition of relativistic jets can be based on radio-astronomical studies of these objects. Thus, for example, we showed previously (Zheleznyakov and Koryagin 2002) that the plasma composition in jets could be judged from the polarization frequency spectra of their synchrotron radiation. The synchrotron radiation of individual electrons and positrons is known to have a high linear polarization ($\sim$70%) and a negligible circular polarization (of the order of the inverse Lorentz factor of the emitting electrons). The polarizations of the synchrotron radiation from electrons and positrons are virtually identical. However, the polarization of the radiation emerging from a jet also depends on the polarizations and refractive indices of the normal (ordinary and extraordinary) electromagnetic waves, which differ significantly in electron–proton and electron–positron plasmas. Therefore, the corpuscular plasma composition can affect the net polarization of the radio emission from the jet. Unfortunately, detailed studies of the polarization spectra are outside the scope of currently available radio-astronomical facilities. The attention in radio astronomy is primarily focused on increasing the angular resolution of antenna systems. Studies of the radiation frequency spectra, which provide important information about the emission generation mechanism, rank next. Finally, polarization studies of the cosmic radio emission are the last in the list of priorities.

Since there are no detailed data on the polarization spectra, the possibilities for determining the jet plasma composition should be analyzed by combining the available information about the polarization at certain frequencies with the characteristics of the frequency spectra of the synchrotron radiation from the jets. This approach is used here. The method for calculating the relative content of cold electrons is described in Sections 2 and 3. Numerical estimates for specific sources are obtained in Section 4. Our main results are summarized in the Conclusions. Note that limited information about the observed radio emission allows us to estimate only the relative content of cold electrons in the jet plasma (and, thus, to identify one of the limiting cases: a cold plasma with an admixture of relativistic particles or a relativistic plasma with a possible admixture of cold electrons). However, the presence (or absence) of relativistic positrons in jets cannot be judged from the available observational data.

2. BASIC RELATIONS FOR A SYNCHROTRON SOURCE

The homogeneous model of a synchrotron radiation source in a jet adopted here is reduced to the following (Zheleznyakov and Koryagin 2002). The jet plasma consists of cold electrons with density n_c in the frame of the jet and of relativistic electrons and positrons with densities n_- and n_+, respectively. The electric charge difference between the electrons and positrons is compensated for by protons. The isotropic energy distribution $f(E)$ of the relativistic electrons and positrons is assumed to be a power law in the energy range from $E_{\min} = \gamma_{\min} mc^2$ to $E_{\max} = \gamma_{\max} mc^2 \gg E_{\min}$:

$$f(E) = \frac{n(p-1)(E/E_{\min})^{-p}}{4\pi E_{\min}} \times \begin{cases} 1 & \text{at } E_{\min} < E < E_{\max} \\ 0 & \text{at } E < E_{\min} \text{ or } E > E_{\max}, \end{cases} \quad (1)$$

where $p > 1$ is the index of the power-law distribution, $\gamma_{\min}$ and $\gamma_{\max}$ are the corresponding Lorentz factors, m is the electron rest mass, c is the speed of light in a vacuum, $n = n_-$ for electrons, and $n = n_+$ for positrons. The magnetic field $\mathbf{B}$ is assumed to be uniform along the propagation path of the radiation and to make angle φ with the line of sight in the frame of the jet.

We assume that the frequency of the observed radiation lies above the turnover frequency for electrons with minimum Lorentz factor $\gamma_{\min}$, but below this frequency for electrons with maximum Lorentz factor $\gamma_{\max}$. In this case, the existence of upper and lower limits in power-law energy distribution (1) has an effect only on the normalization factors of the radiative transfer coefficients, but does not affect their power-law frequency profiles. The above condition constrains the magnetic field for which our study is valid by the following inequalities:

$$B \gg B_{\min} = \frac{2\pi mc\nu}{3e\gamma_{\max}^2 \sin\varphi} \quad (2)$$

$$= 1.68 \times 10^{-6} \left(\frac{\nu}{1\ \text{GHz}}\right) \left(\frac{\gamma_{\max}}{10^4}\right)^{-2} \left(\frac{\sin\varphi}{1/\sqrt{2}}\right)^{-1} \text{G},$$

$$B \ll B_{\max} = \frac{2\pi mc\nu}{3e\gamma_{\min}^2 \sin\varphi} \quad (3)$$

$$= 1.68 \times 10^{-2} \left(\frac{\nu}{1\ \text{GHz}}\right) \left(\frac{\gamma_{\min}}{10^2}\right)^{-2} \left(\frac{\sin\varphi}{1/\sqrt{2}}\right)^{-1} \text{G},$$

where ν is the frequency of the observed radiation in the frame of the jet and $e > 0$ is the elementary charge. The frequency ν is related to the corresponding frequency ν_{obs} in the observer's frame

by the Doppler formula: $\nu = \nu_{\rm obs}(1+z)/\delta$, where z is the cosmological redshift of the source, $\delta = (1 - v_{\rm j}^2/c^2)^{1/2}/[1 - v_{\rm j}\cos(\theta_{\rm j})/c]$ is the Doppler factor attributable to the plasma motion in the jet with bulk velocity $v_{\rm j}$, and $\theta_{\rm j}$ is the angle between the jet axis and the line of sight in the observer's frame.

At high frequencies, where the optical depth of the jet (Zheleznyakov 1996, § 7.4.2),

$$\tau = \frac{\sqrt{3}\alpha}{18}\Gamma\left(\frac{6\alpha+5}{12}\right)\Gamma\left(\frac{6\alpha+25}{12}\right) \times \frac{e^2(n_- + n_+)L}{mc\gamma_{\rm min}^5\nu_B\sin\varphi}\left(\frac{3\gamma_{\rm min}^2\nu_B\sin\varphi}{\nu}\right)^{\alpha+5/2}, \quad (4)$$

is small, the intensity of the observed radiation (per unit solid angle) has a power-law frequency profile, $I_\nu \propto \nu^{-\alpha}$. The spectral index α is uniquely related to the index p of power-law distribution (1): $\alpha = (p-1)/2$. In what follows, the radiation frequency spectrum in the range where $\tau \ll 1$ is assumed to fall off, implying that $\alpha > 0$. In Eq. (4) and below, $\nu_B = eB/(2\pi mc)$ is the nonrelativistic electron cyclotron frequency, L is the ray path length in the jet, and $\Gamma(x)$ is the gamma function. In the frame of the jet, the radiation intensity is described by the following expression (Zheleznyakov 1996, § 5.2.5):

$$I_\nu = \frac{\sqrt{3}\alpha}{2(\alpha+1)}\Gamma\left(\frac{3\alpha+1}{6}\right)\Gamma\left(\frac{3\alpha+11}{6}\right) \times \frac{e^2(n_- + n_+)L}{c(\nu_B\sin\varphi)^{-1}}\left(\frac{3\gamma_{\rm min}^2\nu_B\sin\varphi}{\nu}\right)^{\alpha}. \quad (5)$$

In the observer's frame, the radiation intensity is (Zheleznyakov 1996, § 1.3.1)

$$I_{\nu{\rm obs}} = I_\nu[\delta/(1+z)]^3. \quad (6)$$

Expressing the ray path length L in the jet from Eq. (5) and substituting it into (4), we can find that the smallness condition for the optical depth is satisfied in magnetic field range (3) if the parameter

$$\tau_{\rm max} = \frac{2(\alpha+1)\Gamma\left(\frac{6\alpha+5}{12}\right)\Gamma\left(\frac{6\alpha+25}{12}\right)}{\Gamma\left(\frac{3\alpha+1}{6}\right)\Gamma\left(\frac{3\alpha+11}{6}\right)}\frac{k_{\rm B}T_{\rm rad}}{\gamma_{\rm min}mc^2} \ll 1. \quad (7)$$

In what follows, it is convenient to use the brightness temperature $T_{\rm rad} = I_\nu c^2/(2\nu^2 k_{\rm B})$ in the frame of the jet ($k_{\rm B}$ is the Boltzmann constant) as a measure of the radiation intensity. The brightness temperature of the radiation is recalculated between the frames of the jet and the observer using the same formula as that for the radiation frequency:

$$T_{\rm rad} = T_{\rm rad\ obs}(1+z)/\delta. \quad (8)$$

In the case of $\alpha = 1/2$ typical of blazar jets (see Section 4), condition (7) takes the form

$$\tau_{\rm max} = 3.69\times10^{-2}\left(\frac{T_{\rm rad}}{10^{10}\ {\rm K}}\right)\left(\frac{\gamma_{\rm min}}{10^2}\right)^{-1} \ll 1. \quad (9)$$

The radiation intensity distribution $I_{\nu{\rm obs}}$ for a bright component in a jet is commonly modeled in the form of a Gaussian distribution,

$$I_{\nu{\rm obs}}(x,y) = \frac{4\ln(2)F_{\nu{\rm obs}}}{\pi\theta_x\theta_y} \times \exp\left(-\frac{4\ln(2)x^2}{\theta_x^2} - \frac{4\ln(2)y^2}{\theta_y^2}\right), \quad (10)$$

where $F_{\nu{\rm obs}}$ is the observed flux density from the entire component, x and y are the angular coordinates measured from the center of the component in mutually perpendicular directions, and θ_x and θ_y are the angular sizes of the component at half maximum. The brightness temperature $T_{\rm rad\ obs}$ corresponding to the radiation intensity at the center of the component $I_{\nu{\rm obs}}(0,0)$ is then given by (Wehrle *et al.* 2001)

$$T_{\rm rad\ obs} = \frac{2\ln(2)F_{\nu{\rm obs}}c^2}{\pi k_{\rm B}\nu_{\rm obs}^2\theta_x\theta_y} = 1.22\times10^{12}\left(\frac{F_{\nu{\rm obs}}}{1\ {\rm Jy}}\right)\left(\frac{\nu_{\rm obs}}{1\ {\rm GHz}}\right)^{-2}\left(\frac{\theta}{0''.001}\right)^{-2}{\rm K}, \quad (11)$$

where $\theta = \sqrt{\theta_x\theta_y}$ is the mean angular size of the component. We will use Eq. (11) below.

In a uniform magnetic field, the polarization of the radiation emerging from a jet is determined by the polarization of the normal waves in the jet and by the phase difference ϕ acquired by the normal waves on the jet length. These quantities can be characterized using the so-called Faraday depth F and the conversion depth H (Zheleznyakov and Koryagin 2002). The latter are related to the phase difference ϕ and the axial ratio of the polarization ellipse $\tan\sigma$ for the normal waves by

$$\phi = \sqrt{H^2+F^2}, \quad \cos(2\sigma) = \frac{H}{\sqrt{H^2+F^2}}, \quad \sin(2\sigma) = \frac{F}{\sqrt{H^2+F^2}}. \quad (12)$$

The polarization ellipses of the extraordinary and ordinary waves are elongated, respectively, across and

along the projection of the magnetic field onto the plane of the sky.[1] .

The Faraday depth F is proportional to the nondiagonal elements ε_{xy} in the Hermitian part of the permittivity tensor written in the coordinate system where the z axis is directed along the wave vector and the y axis is directed along the projection of the magnetic field onto the plane of the sky (Sazonov 1969; Zheleznyakov and Koryagin 2002). It is equal to the sum

$$F = F_{\rm c} + F_{\rm rel}, \tag{13}$$

where the term

$$F_{\rm c} = \frac{2e^2 n_{\rm c} L \cot\varphi}{mc\nu_B \sin\varphi}\left(\frac{\nu_B \sin\varphi}{\nu}\right)^2 \tag{14}$$

is specified by the cold electrons and the term

$$F_{\rm rel} = \frac{2e^2(n_- - n_+)L\cot\varphi}{mc\nu_B\sin\varphi}\frac{\alpha\ln\gamma_{\rm min}}{(\alpha+1)\gamma_{\rm min}^2} \times\left(\frac{\nu_B\sin\varphi}{\nu}\right)^2 \tag{15}$$

is specified by the relativistic electrons and positrons in the jet plasma.[2]

The conversion depth H is proportional to the difference between the diagonal elements $\varepsilon_{yy} - \varepsilon_{xx}$ of the Hermitian part of the permittivity tensor. The quantity H is specified mainly by the relativistic particles, while the contribution of the cold electrons is negligible (much smaller than $F_{\rm c}$):

$$H \approx H_{\rm rel} = \frac{4e^2(n_- + n_+)L}{mc\nu_B\sin\varphi}(\alpha\gamma_{\rm min}\mathcal{H})\left(\frac{\nu_B\sin\varphi}{\nu}\right)^3, \tag{16}$$

where the numerical factor (Sazonov 1969)

$$\mathcal{H} \approx \frac{1 - [\gamma_{\rm min}^2\nu_B\sin(\varphi)/\nu]^{\alpha-1/2}}{2\alpha - 1}. \tag{17}$$

The polarization plane of the synchrotron radiation from the elementary sources in the jet (electrons and positrons) is perpendicular to the projection of the magnetic field onto the plane of the sky. Along the propagation path in the jet, the polarization plane of the radiation undergoes rotation that is determined by the plasma parameters on the line of sight. As a result, the polarization plane of the observed radiation differs from the polarization plane of the radiation from the elementary sources. This difference is characterized by the rotation angle $\Delta\chi$. In observations, $\Delta\chi$ can be defined as the angle between the polarizations of the observed radiation at a given frequency and at higher frequencies where the Faraday depth may be assumed to be zero. The rotation angle $\Delta\chi$ is the same in the frames of the jet and the observer.

In our model, we assume that the rotation of the polarization plane of the observed radiation is produced only by the jet plasma. For nearly circular polarization of the normal waves, when $H \ll F$, the rotation angle $\Delta\chi$ is proportional to the Faraday depth F (Zheleznyakov 1996, § 4.2.3):

$$\Delta\chi = F/4, \tag{18}$$

where $\Delta\chi$ is measured in radians.[3] The Faraday depth (13) and the angle $\Delta\chi$ are proportional to the square of the wavelength $\lambda_{\rm obs} = c/\nu_{\rm obs}$:

$$\Delta\chi = {\rm RM}_{\rm obs}\lambda_{\rm obs}^2, \tag{19}$$

where the proportionality factor ${\rm RM}_{\rm obs}$ is the so-called rotation measure (Zheleznyakov 1996, § 4.2.1), which can be estimated from observations. In the case where the polarization plane rotates in the emission generation region, the rotation measure (given the contribution from the relativistic plasma component) is

[1] If the polarization of the normal waves in a jet is circular ($H = 0$, as, e.g., in a cold electron–proton plasma), then the linear polarization of the radiation on the propagation path in the jet undergoes Faraday rotation. In this case, the polarization of the radiation emerging from the jet remains purely linear. Elliptical polarization of the normal waves (different from purely circular polarization, i.e., $H \neq 0$) leads to the so-called conversion of the linearly polarized synchrotron radiation of elementary sources into partially circular polarization of the radiation emerging from the jet. This conversion is a generalization of the Faraday effect to elliptically polarized normal waves (Pacholczyk 1973; Zheleznyakov 1996, § 4.2.1) Elliptical polarization of the normal waves is typical of a relativistic electron plasma at low frequencies.

[2] A number of authors (Jones and O'Dell 1977a, 1977b; Wardle 1977) use $F_{\rm rel}$ that is a factor of $2\alpha + 3$ larger than (15). This increase in $F_{\rm rel}$ is valid if power-law particle distribution (1) decreases smoothly at low energies $E < E_{\rm min}$. Expression (15) exactly corresponds to distribution (1) with a sharp break at $E = E_{\rm min}$ (for a discussion of the various expressions for $F_{\rm rel}$, see Appendix C in Jones and O'Dell (1977a)).

[3] If the rotation of the polarization plane is produced by the plasma outside the emitting jet, then the rotation angle is $\Delta\chi = F/2$ (Zheleznyakov 1996, § 4.2.1).

$$\mathrm{RM}_{\mathrm{obs}} = \frac{e^2\nu_B L\cos\varphi}{2mc^3}\left(\frac{\delta}{1+z}\right)^2 \times \left[n_{\mathrm{c}} + \frac{\alpha\ln\gamma_{\min}}{(\alpha+1)\gamma_{\min}^2}(n_- - n_+)\right]$$
$$= 0.41\left(\frac{\delta}{1+z}\right)^2\left(\frac{B}{10^{-2}\ \mathrm{G}}\right)\left(\frac{L\cos\varphi}{1\ \mathrm{pk}}\right) \times \left[\frac{n_{\mathrm{c}} + \frac{\alpha}{\alpha+1}\gamma_{\min}^{-2}\ln(\gamma_{\min})(n_- - n_+)}{1\ \mathrm{cm}^{-3}}\right]\frac{\mathrm{rad}}{\mathrm{cm}^2}.$$

Relation (18) also roughly holds for arbitrarily polarized normal waves as long as the phase difference $\phi = \sqrt{H^2+F^2} \ll 1$.

The cases where the polarization plane also rotates outside the jet—in the accretion disk, in the narrow line regions of blazars, and in the boundary layer between the jet and the interstellar or intergalactic medium—are considered in the literature when interpreting the observations (Zavala and Taylor 2002, 2003a, 2003b; Gabuzda and Chernetskiĭ 2003). The observed value of $\mathrm{RM}_{\mathrm{obs}}$ should then be considered as an upper limit for the rotation measure produced by the plasma in the jet.

Let us express the relative content of cold electrons $n_{\mathrm{c}}/(n_- + n_+)$ in terms of the observed quantities and model jet parameters. The cold electron density is determined by the Faraday depth (13), while the relativistic particle density $n_- + n_+$ is specified by the radiation intensity (5). Therefore, taking the ratio of Eqs. (13) and (5) yields

$$\frac{n_{\mathrm{c}}}{n_- + n_+} = \frac{\sqrt{3}}{8}\frac{\alpha}{\alpha+1}\Gamma\left(\frac{3\alpha+1}{6}\right) \times \Gamma\left(\frac{3\alpha+11}{6}\right)\left(\frac{3\gamma_{\min}^2\nu_B\sin\varphi}{\nu}\right)^{\alpha}\frac{mc^2F}{k_{\mathrm{B}}T_{\mathrm{rad}}\cot\varphi} - \frac{n_- - n_+}{n_- + n_+}\frac{\alpha}{\alpha+1}\frac{\ln\gamma_{\min}}{\gamma_{\min}^2}. \quad (20)$$

In Eq. (20), the frequency ν, the spectral index α, the brightness temperature T_{rad}, and the Faraday depth $F = 4\Delta\chi$ can be determined from observations if the redshift z of the source and the Doppler factor δ of the jet are known. In this case, Eq. (20) represents the dependence of $n_{\mathrm{c}}/(n_- + n_+)$ on the magnetic field B in the jet (proportional to the frequency ν_B) at fixed minimum Lorentz factor of the relativistic particles $\gamma_{\min}$ and angle φ. The ratio $n_{\mathrm{c}}/(n_- + n_+)$ increases with B at $\alpha > 0$ (which is assumed to be satisfied). At the same time, the magnetic field B in the jet should not exceed $B_{\max}$ (3) for the observed radiation to be determined by particles with Lorentz factors $\gamma \gg \gamma_{\min}$. Therefore, dependence (20) together with constraint (3) specify an upper limit for the relative content of cold electrons[4],

$$\left(\frac{n_{\mathrm{c}}}{n_- + n_+}\right)_{\max} = \frac{\sqrt{3}}{8}\frac{\alpha}{\alpha+1}\Gamma\left(\frac{3\alpha+1}{6}\right) \times \Gamma\left(\frac{3\alpha+11}{6}\right)\frac{mc^2F}{k_{\mathrm{B}}T_{\mathrm{rad}}\cot\varphi}. \quad (21)$$

When passing from (20) to (21), we discarded the last term in (20) to simplify the resulting estimate (21), in particular, to make it valid for any plasma composition with $n_- \geq n_+$. Indeed, retaining the discarded term can only decrease the above upper limit (21) for the ratio $n_{\mathrm{c}}/(n_- + n_+)$. Limit (21) is determined only by the brightness temperature T_{rad} and the rotation angle $\Delta\chi = F/4$ of the polarization plane of the radiation emerging from the jet at a certain frequency at which the source's optical depth $\tau \ll 1$. Expression (21) for the spectral index $\alpha = 1/2$ and the inclination angle of the magnetic field $\varphi = \pi/4$ takes the form

$$\left(\frac{n_{\mathrm{c}}}{n_- + n_+}\right)_{\max} = 9.45\times10^{-2}F\left(\frac{T_{\mathrm{rad}}}{10^{10}\ \mathrm{K}}\right)^{-1} = 5.94\times10^{-1}\left(\frac{\Delta\chi}{90^\circ}\right)\left(\frac{T_{\mathrm{rad}}}{10^{10}\ \mathrm{K}}\right)^{-1}. \quad (22)$$

It is clear from Eq. (21) that the maximum relative content of cold electrons decreases with increasing brightness temperature of the jet radiation and with decreasing Faraday rotation of the polarization plane. Therefore, a predominance of the relativistic component in the plasma might be expected for bright jets with a small rotation angle of the polarization plane. However, it should be emphasized that the cold electron plasma component can determine the polarization and refractive indices of the normal waves even at a low relative density $n_{\mathrm{c}}/(n_- + n_+)$. This is because the inertia of the cold electrons is lower than that of the relativistic electrons and positrons.

3. A UNIVERSAL DIAGRAM

It is convenient to analyze the possible ratios of the densities of the cold electrons n_{c} and the relativistic component $n_- + n_+$ using a special diagram shown in Fig. 1 in two versions, for an electron–proton plasma (Fig. 1a) and for a plasma with equal relativistic electron and positron densities (Fig. 1b), in

[4] An expression similar to (21) (to within a numerical factor) was derived by Wardle (1977), who assumed that $\Delta\chi = F/2$ and limited the magnetic field in the jet above by a value that is a factor of 3 larger than (3).

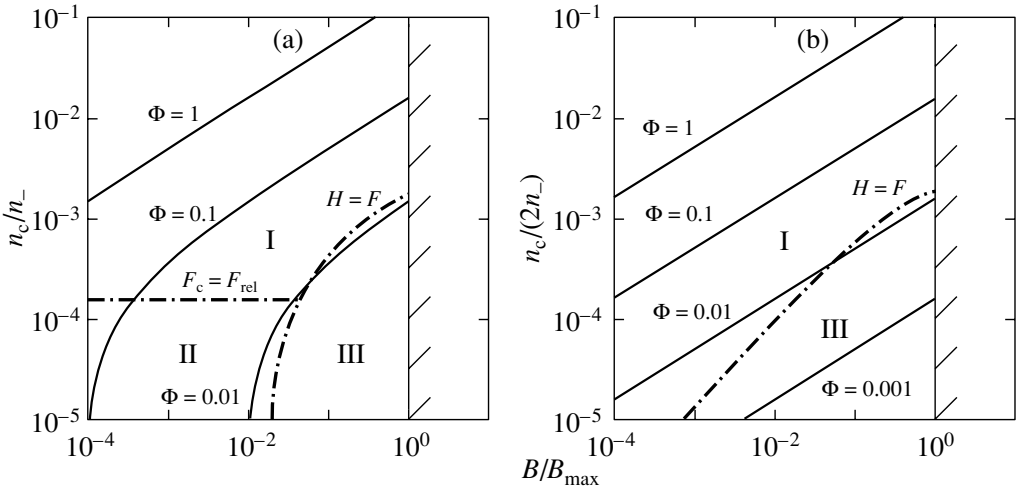

Fig. 1. The $n_c/(n_- + n_+)$—B/B_{max} plane for $\gamma_{min} = 10^2$, $\alpha = 1/2$, $\varphi = \pi/4$: (a) for an electron–proton plasma ($n_+ = 0$) and (b) for a plasma with equal relativistic electron and positron densities ($n_- = n_+$). The dash-dotted $H = F$ lines separate the regions of circular (I, II) and linear (III) polarizations of the normal waves. The horizontal straight $F_c = F_{rel}$ line (Fig. 1a) separates the regions where the circular polarization of the normal waves is determined by the cold (region I) and relativistic (region II) plasma components. The solid lines are specified by Eq. (20) at various values of the parameter Φ (26).

the plane of the dimensionless parameters $n_c/(n_- + n_+)$ and

$$\frac{B}{B_{max}} = \frac{3\nu_B\gamma_{min}^2\sin\varphi}{\nu}, \qquad (23)$$

where B_{max} is the upper limit of the magnetic field range (3) under consideration. The first parameter specifies the relative content of cold electrons and relativistic particles (electrons and positrons) in the radiation source. The second parameter characterizes the magnetic field in the jet at given minimum Lorentz factor of the relativistic particles γ_{min}, angle φ, Doppler factor of the jet δ, and redshift of the source z, which fix B_{max}. The regions with different polarization of the normal waves are indicated in the diagram. In the limiting cases, this polarization is close to the circular polarization determined by cold electrons (region I), to the circular polarization attributable to relativistic electrons (region II), and to the linear polarization specified by relativistic electrons and by the possible presence of relativistic positrons (region III).

The mutual arrangement of the regions with different polarizations is obvious. Indeed, at a fairly high cold electron density, the normal waves have circular polarization (region I). At a low cold electron density, the polarization of the normal waves is determined by relativistic particles (regions II and III). If the relativistic component consists only of electrons, then the polarization of the normal waves in weak magnetic fields remains circular (region II). As the magnetic field increases, the conversion depth $H \propto B^2$ becomes larger than the Faraday depth $F \propto B$ and the polarization of the normal waves proves to be linear (region III). If the relativistic component is represented by electrons and positrons with equal densities, then the circular polarization of the normal waves is determined only by cold electrons (therefore, region II is absent). When the effect of the cold component is negligible, the polarization of the normal waves in a plasma of relativistic electron–positron pairs can be only linear.

The above regions of circular (I, II) and linear (III) polarization of the normal waves are separated by the $H = F$ line where the Faraday (13) and conversion (16) depths are equal in absolute value:

$$\left(\frac{n_c}{n_- + n_+}\right)_{H=F} = \frac{2\alpha\gamma_{min}\nu_B\sin\varphi}{\nu|\cot\varphi|}\mathcal{H} - \frac{n_- - n_+}{n_- + n_+}\frac{\alpha}{\alpha+1}\frac{\ln\gamma_{min}}{\gamma_{min}^2}. \qquad (24)$$

The $F_c = F_{rel}$ line on which contributions (14) and (15) from the cold and relativistic plasma components to the Faraday depth (13) are identical,

$$\left(\frac{n_c}{n_- + n_+}\right)_{F_c=F_{rel}} = \frac{n_- - n_+}{n_- + n_+}\frac{\alpha}{\alpha+1}\frac{\ln\gamma_{min}}{\gamma_{min}^2}, \qquad (25)$$

separates (inside the region of circular polarization) regions I and II, where the refractive indices of the normal waves are specified by the cold and relativistic plasma components, respectively.

The locations of the $H = F$ and $F_c = F_{rel}$ lines in the diagram under consideration depend mainly on

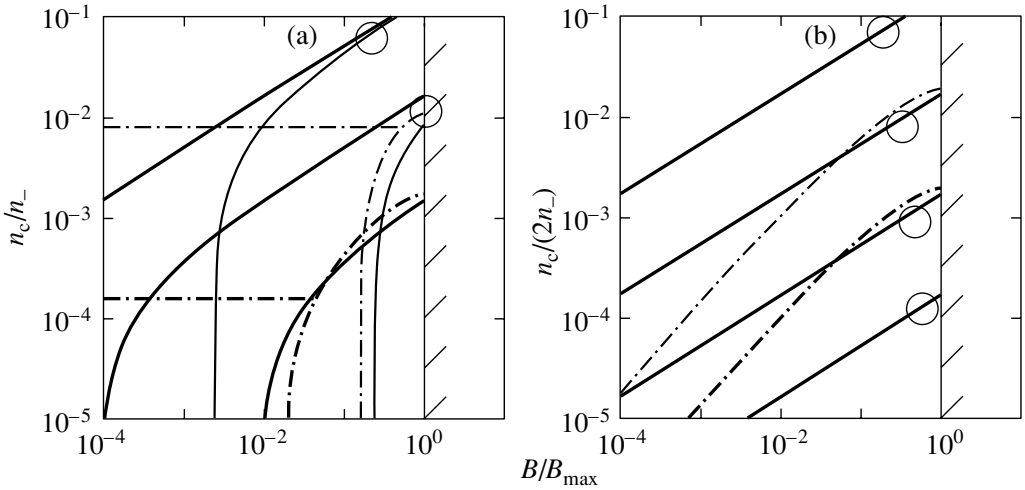

Fig. 2. Change in the universal diagram as the minimum Lorentz factor γ_{min} is varied: (a) for an electron–proton plasma and (b) for a plasma with equal relativistic electron and positron densities. The parameters $\alpha = 1/2$ and $\varphi = \pi/4$ are fixed. The thick lines correspond to $\gamma_{min} = 10^2$ and retrace the curves in Fig. 1; the thin lines correspond to $\gamma_{min} = 10$. The circles mark lines (20) with equal values of the parameter Φ (26) at different γ_{min}. For a plasma with equal relativistic electron and positron densities (Fig. 2b), solid lines (20) do not move over the $n_c/(n_- + n_+) - B/B_{max}$ plane as γ_{min} is varied. For an electron–proton plasma (Fig. 2a), lines (20) do not change only in region I above the dash–dotted lines where the polarization of the normal waves is specified by the cold plasma.

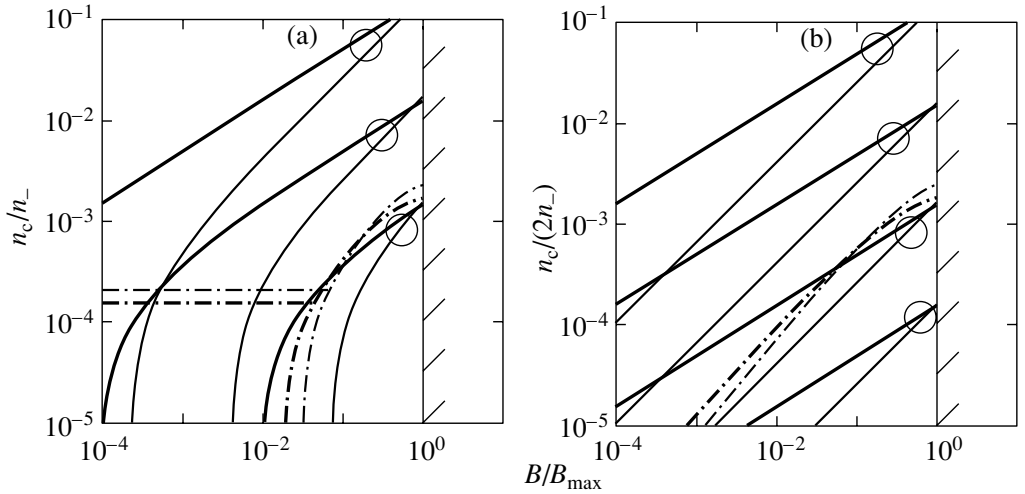

Fig. 3. Change in the universal diagram as the spectral index α is varied: (a) for an electron–proton plasma and (b) for a plasma with equal relativistic electron and positron densities. The parameters $\gamma_{min} = 10^2$ and $\varphi = \pi/4$ are fixed. The thick lines correspond to $\alpha = 1/2$ and retrace the curves in Fig. 1; the thin lines correspond to $\alpha = 0.8$. The circles mark lines (20) with equal values of the parameter Φ (26) at different α. The dash–dotted lines separating the regions with different polarization of the normal waves change only slightly, while solid lines (20) change appreciably the slope and the point of intersection with the horizontal coordinate axis as α is varied. The ratio $[n_c/(n_- + n_+)]_{max}$ at the point of intersection of lines (20) with the vertical straight $B/B_{max} = 1$ line depends weakly on α.

the minimum Lorentz factor γ_{min} (see Fig. 2). To a lesser degree, they depend on the spectral index α (see Fig. 3) and the angle φ (provided that α is not too close to zero and φ differs markedly from 0 and $\pi/2$). For definiteness, we took $\gamma_{min} = 10^2$, $\alpha = 1/2$, and $\varphi = \pi/4$ to construct the diagrams in Fig. 1. As the Lorentz factor γ_{min} increases, the $H = F$ and $F_c = F_{rel}$ lines are displaced downward in the diagram along the logarithmic $n_c/(n_- + n_+)$ axis (see Fig. 2). The peak of the $H = F$ line sinks more slowly than the horizontal $F_c = F_{rel}$ line. At the same time, the point of intersection of the $H = F$ and $F_c = F_{rel}$ lines is displaced leftward in the diagram along the B/B_{max} axis for an electron–proton plasma. In particular,

at $\alpha > 1/2$, $n_c/(n_- + n_+)$ at the point of intersection of the $H = F$ line with the vertical $B/B_{max} = 1$ boundary of the diagram decreases proportionally to γ_{min}^{-1} for any composition of the relativistic plasma component (if $\gamma_{min} \gg 1$). The $n_c/(n_- + n_+)$ level on the horizontal $F_c = F_{rel}$ line varies proportionally to $\gamma_{min}^{-2} \ln\gamma_{min}$. The parameter B/B_{max} at the point of intersection of the $H = F$ line with the horizontal coordinate axis (where $n_c/(n_- + n_+) = 0$) is proportional to $\gamma_{min}^{-1} \ln\gamma_{min}$ for an electron–proton plasma.

The brightness temperature of the radiation T_{rad} and the rotation angle of the polarization plane $\Delta\chi$ determined from the observations of a specific object specify line (20) in the diagram on which the possible jet plasma parameters lie. If the observed value of $\Delta\chi$ is considered as an upper limit for the rotation angle of the polarization plane in the jet plasma, then the admissible values of $n_c/(n_- + n_+)$ and B/B_{max} lie below curve (20). Figure 1 indicates several lines (20) corresponding to different values of the parameter

$$\Phi = \frac{mc^2F}{k_B T_{rad}\cot\varphi} = 5.93\times10^{-1} \times \left(\frac{F}{\cot\varphi}\right)\left(\frac{T_{rad}}{10^{10}\ \mathrm{K}}\right)^{-1}. \quad (26)$$

The intersection of line (20) with the vertical line of the maximum magnetic field, $B/B_{max} = 1$, determines the maximum relative content of cold electrons for a given plasma composition. The maximum possible value of $[n_c/(n_- + n_+)]_{max}$ (21) among all of the plasma compositions is reached for a plasma with equal relativistic electron and positron densities ($n_- = n_+$).

Line (20) intersects the horizontal $n_c/(n_- + n_+) = 0$ axis at a nonzero magnetic field,

$$B_c = \frac{2\pi mc\nu}{3e\gamma_{min}^2\sin\varphi}\left(\frac{8}{\sqrt{3}\Gamma\left(\frac{3\alpha+1}{6}\right)\Gamma\left(\frac{3\alpha+11}{6}\right)} \times \frac{n_- - n_+}{n_- + n_+}\frac{\ln\gamma_{min}}{\gamma_{min}^2}\frac{k_B T_{rad}\cot\varphi}{mc^2F}\right)^{1/\alpha}, \quad (27)$$

if $n_- \neq n_+$. As a result, the admissible magnetic field in a jet for a fixed plasma composition is limited below by (27). In a weaker magnetic field ($B < B_c$), including only the relativistic plasma component leads to a rotation of the polarization plane that exceeds the observed value. This excludes the magnetic fields $B < B_c$ from the admissible region of parameters for a fixed plasma composition. In a plasma with equal relativistic electron and positron densities ($n_- = n_+$), the relativistic component gives a zero contribution (15) to the Faraday depth F, the value of (27) becomes zero, and the magnetic field can take on arbitrarily low values.

Thus, if the magnetic field B in a jet is weaker than (27) for a plasma with $n_+ = 0$, then positrons must be present in this jet. Since (27) increases sharply with decreasing minimum Lorentz factor γ_{min}, the presence of positrons might be expected in jets with low γ_{min}. In the case of an electron–proton plasma for $\alpha = 1/2$ and $F = 4\Delta\chi$, the minimum magnetic field (27) is

$$B_c = 1.07\times10^{-5}\left(\frac{\nu}{1\ \mathrm{GHz}}\right)\left(\frac{\ln\gamma_{min}}{5}\right)^2 \times \left(\frac{\gamma_{min}}{10^2}\right)^{-6}\left(\frac{T_{rad}}{10^{10}\ \mathrm{K}}\right)^2\left(\frac{\Delta\chi}{1^\circ}\right)^{-2}\left(\frac{\cot^2\varphi}{\sqrt{2}\sin\varphi}\right)\ \mathrm{G}. \quad (28)$$

The magnetic field B in a jet can be determined from radio observations if the turnover frequency ν_t of the identified component in the jet is known. If the turnover in the frequency spectrum at $\nu < \nu_t$ is attributable to the reabsorption of synchrotron radiation, then the optical depth τ at the turnover frequency ν_t is of the order of unity. We find from the ratio of the intensity of the radiation (5) recorded at frequency $\nu \gg \nu_t$ and from Eq. (4) for the optical depth at frequency ν_t that the magnetic field in a jet is

$$B = \left[\frac{\Gamma\left(\frac{3\alpha+1}{6}\right)\Gamma\left(\frac{3\alpha+11}{6}\right)}{2\sqrt{3}(\alpha+1)\Gamma\left(\frac{6\alpha+5}{12}\right)\Gamma\left(\frac{6\alpha+25}{12}\right)}\right]^2 \times \frac{2\pi mc\nu}{e\sin\varphi}\left(\frac{mc^2}{k_B T_{rad}}\right)^2\left(\frac{\nu_t}{\nu}\right)^{2\alpha+5}\tau_t^2, \quad (29)$$

where the optical depth of the jet τ_t at frequency ν_t can be determined from the equation $[1 + (1 + 2\alpha/5)\tau_t] \times \exp(-\tau_t) = 1$ and the brightness temperature of the radiation T_{rad} corresponds to the frequency ν. In particular, Eq. (29) at $\alpha = 1/2$ takes the form

$$B = 1.55\left(\frac{\nu}{1\ \mathrm{GHz}}\right)\left(\frac{T_{rad}}{10^{10}\ \mathrm{K}}\right)^{-2} \times \left(\frac{\nu_t}{\nu}\right)^6\left(\frac{\sin\varphi}{1/\sqrt{2}}\right)^{-1}\ \mathrm{G}. \quad (30)$$

If the magnetic field B (29) is larger than B_c (27), then the intersection of curve (20) and vertical line (29) determines a possible value of the parameter $n_c/(n_- + n_+)$ lower than the maximum value (21). Otherwise ($B < B_c$), curve (20) does not intersect line (29); i.e., magnetic field (29) is outside the admissible range of values for the chosen plasma composition.

The above scenario for the formation of a maximum in the frequency spectrum and a low-frequency

turnover due to reabsorption is realized if the synchrotron radiation of relativistic particles with minimum Lorentz factor $\gamma_{\min}$ occurs at frequencies below ν_t, and, hence, $\gamma_{\min}$ does not exceed

$$\gamma_t = \left(\frac{\nu_t}{3\nu_B \sin\varphi}\right)^{1/2} = \frac{2(\alpha+1)\Gamma\left(\frac{6\alpha+5}{12}\right)\Gamma\left(\frac{6\alpha+25}{12}\right)}{\Gamma\left(\frac{3\alpha+1}{6}\right)\Gamma\left(\frac{3\alpha+11}{6}\right)} \times \left(\frac{k_B T_{\rm rad}}{mc^2}\right)\left(\frac{\nu}{\nu_t}\right)^{\alpha+2}\tau_t^{-1}, \quad (31)$$

where the cyclotron frequency ν_B is expressed in terms of magnetic field (29). At $\alpha = 1/2$, (31) can be rewritten as

$$\gamma_t = 10.4\left(\frac{T_{\rm rad}}{10^{10}\ {\rm K}}\right)\left(\frac{\nu}{\nu_t}\right)^{5/2}. \quad (32)$$

The constraint $\gamma_{\min} < \gamma_t$ allows us to formulate a more stringent (sufficient) condition for the presence of positrons in a jet that does not depend on the model parameter $\gamma_{\min}$. Indeed, the lower limit B_c (27) for the admissible magnetic field increases with decreasing Lorentz factor $\gamma_{\min}$. Therefore, if the condition for the presence of positrons in a jet ($B < B_c$ at $n_+ = 0$) is satisfied at $\gamma_{\min} = \gamma_t$, then it is definitely also satisfied for $\gamma_{\min} < \gamma_t$. Consequently, the inequality $B/B_c < 1$, in which the magnetic field B is defined by Eq. (29) and B_c is defined by Eq. (27) at $n_+ = 0$ and $\gamma_{\min} = \gamma_t$ (see Eq. (31)), serves as a sufficient condition for the presence of positrons in a jet:

$$\frac{\sqrt{3}\left[(\alpha+1)\Gamma\left(\frac{6\alpha+5}{12}\right)\Gamma\left(\frac{6\alpha+25}{12}\right)\right]^2}{2\Gamma\left(\frac{3\alpha+1}{6}\right)\Gamma\left(\frac{3\alpha+11}{6}\right)} \times \left(\frac{k_B T_{\rm rad}}{mc^2}\right)\left(\frac{F}{\cot\varphi}\right)\left(\frac{\nu}{\nu_t}\right)^{\alpha+4}\frac{1}{\tau_t^2 \ln\gamma_t} < 1. \quad (33)$$

At $\alpha = 1/2$ and $F = 4\Delta\chi$, condition (33) can be written as

$$\frac{0.43}{\cot\varphi}\left(\frac{\ln\gamma_t}{5}\right)^{-1}\left(\frac{T_{\rm rad}}{10^{10}\ {\rm K}}\right)\left(\frac{\Delta\chi}{1^\circ}\right)\left(\frac{\nu}{\nu_t}\right)^{9/2} < 1. \quad (34)$$

It should be emphasized that the calculation of the magnetic field using Eq. (29) and the sufficient condition for the presence of positrons in a jet (33) suggest that the turnover of the synchrotron radiation is attributable to reabsorption at low frequencies, $\nu < \nu_t$. It is also possible that the optical depth at the turnover frequency ν_t is $\tau \ll 1$ and the spectral turnover appears due to the absence of relativistic particles with Lorentz factors $\gamma < \gamma_{\min}$ and the corresponding decrease in the plasma synchrotron emissivity at frequencies $\nu < \nu_t$. In this case, the turnover frequency ν_t is close to $0.5\gamma_{\min}^2\nu_B \sin\varphi$, the frequency of the synchrotron emissivity maximum for electrons with Lorentz factor $\gamma_{\min}$ (Zheleznyakov 1996, § 5.1.5). These two cases differ by the pattern of the spectrum at frequencies $\nu < \nu_t$. The spectrum is rather steep ($I_\nu \propto \nu^{5/2}$) in the former case and very flat ($I_\nu \propto \nu^{1/3}$) in the latter case (Zheleznyakov 1996, § 5.1.5, § 7.4.2).

The maxima in the low-frequency radiation spectra of individual components in blazar jets can be reliably detected very rarely (Unwin *et al.* 1997; Piner *et al.* 2000). This is because these maxima commonly occur at frequencies of a few GHz or lower. In this frequency range, the angular resolution of ground-based interferometric arrays is too low to reliably separate the radiation from the core (the base of the jet) and the component moving in the jet along the entire trajectory of the latter. Ground-based observations allow the turnover frequency of an individual component in a jet to be determined only in a small segment of its trajectory near the core where the turnover frequency is high enough to ensure an acceptable angular resolution (see, e.g., the observations of the quasar 3C 345 by Unwin *et al.* 1997). At larger distances where the turnover frequency is lower, interferometric observations with a very large baseline where one of the antennae is based on a satellite are required (Piner *et al.* 2000).

Knowledge of the magnetic field in a jet allows the relationship between the relativistic particle and magnetic field energy densities to be determined. In the $n_c/(n_- + n_+) - B$ plane for the specific objects considered in the next section, the magnetic field $B_{\rm eq}$ separates the region $B < B_{\rm eq}$, where the relativistic particle energy density

$$W_e = \frac{2\alpha}{2\alpha - 1} \times [1 - (\gamma_{\min}/\gamma_{\max})^{2\alpha-1}]mc^2\gamma_{\min}(n_- + n_+) \quad (35)$$

is higher than the magnetic field energy density

$$W_{\rm mag} = B^2/(8\pi), \quad (36)$$

and the region $B > B_{\rm eq}$ where the magnetic field energy dominates.[5]

[5] For simplicity, the pressure of the cold electrons and protons is disregarded. This approximation is definitely valid over a wide range of density ratios $n_c/(n_- + n_+) \ll \gamma_{\min}$, where the maximum possible pressure of the cold electrons, of the order of $mc^2 n_c$, does not exceed the characteristic pressure of the relativistic particles, of the order of $\gamma_{\min}mc^2(n_- + n_+)$. Including the cold particle pressure would increase $B_{\rm eq}$.

Let us calculate $B_{\rm eq}$. The magnetic field and relativistic particle energy densities are equal at the electron and positron density

$$(n_- + n_+)_{\rm eq} = \frac{B^2}{8\pi mc^2\gamma_{\rm min}}\frac{2\alpha-1}{2\alpha} \times [1-(\gamma_{\rm min}/\gamma_{\rm max})^{2\alpha-1}]^{-1}. \quad (37)$$

Substituting density (37) into Eq. (5) for the intensity of the jet radiation yields the magnetic field $B_{\rm eq}$ that corresponds to an equipartition of energy between the particles and the magnetic field:

$$B_{\rm eq} = \frac{2\pi mc\nu}{3e\gamma_{\rm min}^2\sin\varphi}\left[\frac{144\sqrt{3}}{\pi}\frac{\alpha+1}{2\alpha-1} \times [1-(\gamma_{\rm min}/\gamma_{\rm max})^{2\alpha-1}]\Gamma^{-1}\left(\frac{3\alpha+1}{6}\right) \times \Gamma^{-1}\left(\frac{3\alpha+11}{6}\right)\frac{c\gamma_{\rm min}^7\sin^2\varphi}{\nu L}\frac{k_{\rm B}T_{\rm rad}}{mc^2}\right]^{1/(\alpha+3)}. \quad (38)$$

In the special case of the spectral index $\alpha = 1/2$, Eq. (38) takes the form

$$B_{\rm eq} = 1.09\times10^{-2}\left(\frac{\ln(\gamma_{\rm max}/\gamma_{\rm min})}{5}\right)^{2/7} \times \left(\frac{\sin\varphi}{1/\sqrt{2}}\right)^{-3/7}\left(\frac{\nu}{1\ {\rm GHz}}\right)^{5/7}\left(\frac{T_{\rm rad}}{10^{10}\ {\rm K}}\right)^{2/7} \times \left(\frac{L}{1\ {\rm pc}}\right)^{-2/7}\ {\rm G}. \quad (39)$$

Note that the magnetic field $B_{\rm eq}$ (39) for $\alpha = 1/2$ depends logarithmically weakly on the model parameters $\gamma_{\rm min}$ and $\gamma_{\rm max}$.

At present, it is hard to tell how nonuniform the magnetic field is within the radiation source located in a jet. We can only note that in a randomly nonuniform magnetic field, the projection of the magnetic field onto the line of sight can change sign along the propagation path of the radiation in the source several times. At the same time, the beam of the receiving antenna can capture several regions with different magnetic field directions. If N is the number of regions with opposite signs of the magnetic field projection onto the line of sight the radiation from which falls within the antenna beam, then the rotation angle of the polarization plane is a factor of $\sqrt{N}$ smaller than its value defined by Eq. (18) for a uniform magnetic field (provided that $\Delta\chi \ll 1$). Therefore, for a random magnetic field, Eqs. (20)–(22) given here are suitable for use as estimates of the ratio $n_{\rm c}/(n_- + n_+)$ if we substitute the angle $\Delta\chi$, which is a factor of $\sqrt{N}$ larger than the observed one, into them.

4. ANALYSIS OF SPECIFIC OBJECTS

In this section, we will estimate the relative content of cold electrons and specify the characteristic regions of parameters in the $n_{\rm c}/(n_- + n_+)-B$ plane in the jets of two extragalactic and one Galactic source based on radio observations. In all our calculations, for definiteness, we assume the angle between the line of sight and the magnetic field to be $\varphi = \pi/4$ and the minimum Lorentz factor of the relativistic electrons and positrons to be $\gamma_{\rm min} = 10^2$. As an estimate of the ray path length in the jet L in Eq. (38), we take the transverse scale length of the emitting component $L_\perp = \theta d$, where d is the distance to the source. For extragalactic sources (blazars), the distance d is determined by the cosmological redshift z and can be calculated using the formula

$$d = \frac{c}{H_0(1+z)}\int_{1/(1+z)}^{1}\frac{{\rm d}a}{\sqrt{\Omega_{\rm M}a+\Omega_\Lambda a^4}}.$$

This formula corresponds to a flat universe with a nonzero cosmological constant (see, e.g., Pen 1999). For our calculations, we take the Hubble constant $H_0 = 70$ km s^{-1} Mpc^{-1}, the nonrelativistic matter density in units of the critical density $\Omega_{\rm M} = 0.3$, and the normalized cosmological constant $\Omega_\Lambda = 0.7$.

The quasar 3C 279. Radiation from this object was detected in a wide frequency range, from radio waves to gamma rays (Hartman *et al.* 2001). Superluminal motion was detected in it for the first time, indicative of a relativistic velocity in the jet (Whitney *et al.* 1971; Cohen *et al.* 1971).

A core and a jet composed of several components (compact sources) receding from the core are seen in the radio images of 3C 279. The components usually fade at a distance of $\sim0\overset{''}{.}001$ from the core, where the stationary component C5 is located (Wehrle *et al.* 2001). At the same time, a bright long-lived component (C4) is identified at a larger distance, $\sim0\overset{''}{.}003$, in the jet.

Using component C4 as an example, let us estimate the relative content of cold electrons in the jet. The rotation measure ${\rm RM}_{\rm obs}$ toward C4 was $(7\pm4)\times10^{-3}$ rad cm^{-2}, as derived by Taylor (1998) on January 25, 1997, in the observer's frame. This rotation measure corresponds to the rotation of the polarization plane through an angle of $\Delta\chi \approx 0\overset{\circ}{.}7$ and to a Faraday depth of $F \approx 0.05$ at the observed frequency $\nu_{\rm obs} = 22$ GHz (see Eqs. (18) and (19)). Having analyzed the radio and X-ray emission from the jet approximately at the same time, January 15, 1997, Piner *et al.* (2003) determined the Doppler factor of the component, $\delta \approx 25$, and its spectral index, $\alpha = 0.5$. At that time, component C4 had angular sizes of $0\overset{''}{.}0003\times0\overset{''}{.}0001$ and produced a flux density

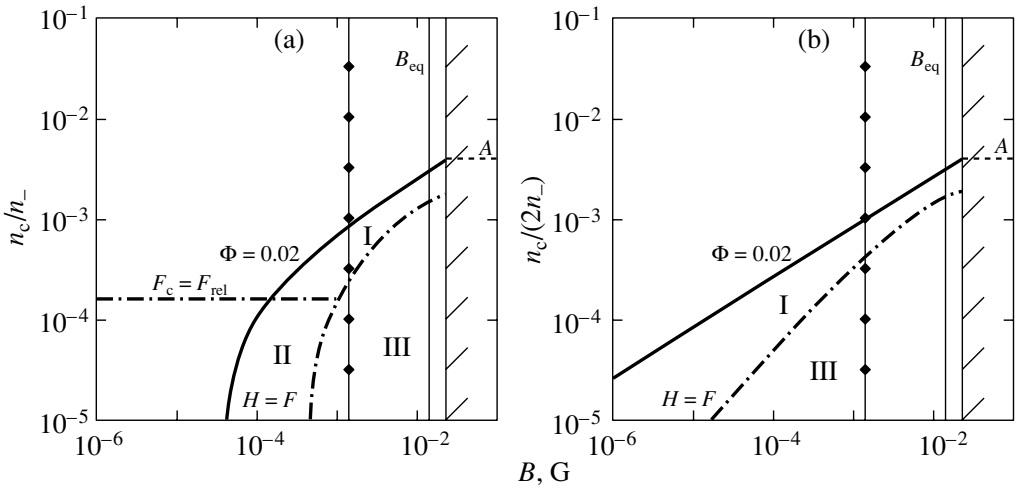

Fig. 4. The $n_c/(n_- + n_+) - B$ plane for component C4 of the quasar 3C 279: (a) for an electron–proton plasma and (b) for a plasma with equal relativistic electron and positron densities. The admissible region of parameters lies below the thick $\Phi = 0.02$ line and to the left of the vertical straight line with hatching corresponding to the magnetic field $B = B_{max}$ (3). The magnetic field $B = 1.4 \times 10^{-3}$ G that corresponds to the observed turnover frequency $\nu_{t\,obs} = 7$ GHz is indicated by the vertical line with diamonds. The maximum ratio $[n_c/(n_- + n_+)]_{max}$ (21) is marked by point A. The dash-dotted $H = F$ lines separate the regions of circular (I, II) and linear (III) polarization of the normal waves. The horizontal straight $F_c = F_{rel}$ line in Fig. 4a separates regions I and II where the circular polarization of the normal waves is determined by the cold (region I) and relativistic (region II) plasma components.

of $F_{\nu obs}(22\ \mathrm{GHz}) \approx 2.3$ Jy (Wehrle *et al.* 2001).[6] It thus follows that the brightness temperature of the radiation is $T_{rad\,obs} \approx 2 \times 10^{11}$ K in the observer's frame (see Eq. (11)) and $T_{rad} = 1.3 \times 10^{10}$ K in the frame of the jet (see Eq. (8)). When the brightness temperature of the radiation is recalculated to the frame of the jet, the cosmological redshift of the blazar, $z \approx 0.54$ (Burbidge and Rosenberg 1965), is taken into account. As a result, we obtain the maximum relative content of cold electrons from Eqs. (21) and (22), $[n_c/(n_- + n_+)]_{max} \approx 4 \times 10^{-3}$. The low value of $[n_c/(n_- + n_+)]_{max}$ implies that the electron plasma component in the jet of the quasar 3C 279 is mainly relativistic.

The $n_c/(n_- + n_+) - B$ diagram for component C4 (see Fig. 4) is obtained from the universal diagram in Fig. 1 if, of all solid lines (20), only the line with $\Phi = 0.02$ (26), which corresponds to the above values of $T_{rad} = 1.3 \times 10^{10}$ K and $F \approx 0.05$, is retained on the latter diagram. At the same time, the variable B/B_{max} (23) along the horizontal axis in Fig. 1 was recalculated to the magnetic field B in Fig. 4 given that $B_{max} = 2.3 \times 10^{-2}$ G (3).

In the diagram, condition (7), (9) of a small optical depth ($\tau \ll 1$) is satisfied for component C4 in the entire range of parameters $B < B_{max}$ under consideration. For the sources BL Lac and GRS 1915+105 analyzed below, condition (7) is also satisfied in the corresponding ranges $B < B_{max}$.

If $F \approx 0.05$ is considered as an upper limit for the Faraday depth determined by the plasma in the jet, then the admissible relative cold electron densities and magnetic fields lie in the diagram below thick line (20) with $\Phi = 0.02$ and to the left of the vertical $B = B_{max}$ line with hatching. These values of $n_c/(n_- + n_+)$ and B fall within all regions I, II, and III with different polarization of the normal waves (see Section 3). Therefore, the polarization of the normal waves in component C4 can be arbitrary and be determined by both the cold and relativistic plasma components.

A year later, Piner *et al.* (2000) performed low-frequency interferometric observations of the quasar 3C 279 at 1.6 and 5 GHz in which one of the antennae was based on a satellite. These observations supplemented with the corresponding ground-based observations yielded the turnover frequency $\nu_{t\,obs} = 7$ GHz of component C4 (Piner *et al.* 2003). Substituting the frequency $\nu = \nu_{obs}(1+z)/\delta$ and the ratio $\nu_t/\nu = \nu_{t\,obs}/\nu_{obs}$ into Eqs. (29), (30), we obtain an estimate of the magnetic field for C4, $B \approx 1.4 \times 10^{-3}$ G. Given the magnetic field, Eq. (20) can be used to estimate the relative content of cold electrons: $n_c/(n_- + n_+) < 9 \times 10^{-4}(\gamma_{min}/10^2)$ for $\varphi = \pi/4$. The latter estimate of $n_c/(n_- + n_+)$ is a factor

[6] According to Wehrle *et al.* (2001), component C4 breaks up into two subcomponents with flux densities of 2.3 and 0.7 Jy. We take into account only the brighter part.

of 4 smaller than the value of $[n_c/(n_- + n_+)]_{max} \approx 4 \times 10^{-3}$ obtained above from (21), (22), but it depends on the chosen $\gamma_{min} = 10^2$.

At the same time, the known turnover frequency limits γ_{min} above by $\gamma_t \approx 2 \times 10^2$ (Eqs. (31), (32)). The Lorentz factor $\gamma_{min} = 10^2$ chosen for our calculations satisfies this condition.

The parameters of component C4 do not satisfy sufficient condition (33), (34) for the presence of positrons in a jet. In particular, we see from the diagram in Fig. 4a that the magnetic field estimated above, $B \approx 1.4 \times 10^{-3}$ G, falls within the range of admissible magnetic fields for a plasma without positrons. Thus, the available radio observations allow for the existence of both an electron–proton plasma without positrons and a plasma with positrons in the jet of 3C 279. The case of a plasma without positrons may be excluded at $\gamma_{min} < 50$. Lower limit (27), (28) of the magnetic field admissible for an electron–proton plasma is larger than the magnetic field in the jet, $B \approx 1.4 \times 10^{-3}$ G, only in this case.

Let us estimate magnetic field B_{eq} (38), (39) that corresponds to an equipartition of energy between the relativistic particles and the magnetic field. For a redshift $z \approx 0.54$ of the quasar 3C 279 (Burbidge and Rosenberg 1965), the typical angular size $\theta \approx 0''.00017$ of component C4 corresponds to a ray path length in the jet of $L \approx 1.1$ pc. In this case, $B_{eq} \approx 1.4 \times 10^{-2}[\ln(\gamma_{max}/\gamma_{min})/5]^{2/7}$ G, which is approximately a factor of 10 larger than the magnetic field strength $B = 1.4 \times 10^{-3}$ G estimated above from the frequency ν_t. The derived relationship $B \ll B_{eq}$ implies that the relativistic particle energy dominates in the jet over the the magnetic field energy. As a result, the magnetic field in C4 can be nonuniform. As we noted in Section 3, for a randomly nonuniform magnetic field, the angle $\Delta\chi$, which is a factor of $\sqrt{N}$ larger than the observed angle, should be substituted into the formulas for a uniform magnetic field. However, this would not affect the qualitative conclusion that the relativistic electron (and, possibly, positron) density exceeds significantly the cold electron density in the jet of 3C 279.

The blazar BL Lac. Its spectrum exhibits no detectable emission lines (Vermeulen *et al.* 1995), while the flux and polarization of its radiation vary rapidly on time scales of several days (see, e.g., Denn *et al.* 2000).

Let us determine the constraints on the corpuscular composition of the plasma in the jet of BL Lac using component K3 observed by Gabuzda and Cawthorne (2000) on July 30, 1995, at a frequency of 22 GHz as an example. At that time, K3 was the brightest component in the jet. Its flux density was $F_{\nu obs} \approx 0.7$ Jy, and its angular size was $\theta \approx 0''.0004$. Denn *et al.* (2000) observed BL Lac approximately at the same time, on August 2, 1995, at the same frequency, but with a lower angular resolution. Two bright components, S7 and S8, were identified in the jet; the parameters of component S8 closer to the core corresponded in order of magnitude to the above parameters of component K3. Modeling the motion of component S8 yielded a Doppler factor of $\delta \approx 5$ (Denn *et al.* 2000). We will use this value in our calculations. The above parameters corrected for the redshift of BL Lac, $z = 0.07$ (Miller *et al.* 1978), allow the brightness temperature of the radiation from the component to be estimated in the frames of the observer and the jet, $T_{rad\,obs} \approx 10^{10}$ K and $T_{rad} \approx 2 \times 10^9$ K, respectively (see (8) and (11)).

We failed to find the exact spectral index α for component K3 on July 30, 1995, and use $\alpha = 0.5$. In particular, it characterizes the radiation from component S9 that appeared later in the jet when S9 was at the same distance from the core as component K3 on July 30, 1995 (Denn *et al.* 2000).

The subsequent observations on April 6, 1997, and the analysis performed by Reynolds *et al.* (2001) showed that the rotation measure RM_{obs} was almost constant along the jet of BL Lac, $\sim 10^{-2}$ rad cm^{-2} (in the core, the rotation measure is larger: 5.5×10^{-2} rad cm^{-2} as estimated by Reynolds *et al.* (2001) and 0.2–1 rad cm^{-2} as derived by Stirling *et al.* (2003)). Reynolds *et al.* (2001) attributed the constancy of the rotation measure along the jet to the fact that the main rotation of the polarization plane takes place not in the jet of BL Lac, but in our Galaxy. In this case, the rotation measure RM_{obs} in the jet of BL Lac is much lower than 10^{-2} rad cm^{-2}. We use 10^{-2} rad cm^{-2} as an upper limit for the rotation measure RM_{obs} in the jet. This rotation measure corresponds to the rotation of the polarization plane through an angle $\Delta\chi \approx 1°.1$ at a frequency of 22 GHz and to a Faraday depth $F \approx 8 \times 10^{-2}$ (see Eqs. (18) and (19)). According to Eqs. (21) and (22), the relative content of cold electrons in the jet of BL Lac then does not exceed $[n_c/(n_- + n_+)]_{max} \approx 3 \times 10^{-2}$, i.e., it is much smaller than unity, as for the quasar 3C 279.

The $n_c/(n_- + n_+)$–B diagram for component K3 (see Fig. 5) is obtained from the universal diagram in Fig. 1 given that $\Phi = 0.2$ (26) and the maximum magnetic field $B_{max} = 8 \times 10^{-2}$ G (3) for the above parameters of K3. In the diagram of Fig. 5, line (20) with $\Phi = 0.2$ encloses all three regions I, II, and III with different polarization of the normal waves. Therefore, the polarization of the normal waves in the jet of BL Lac can be determined by both a small fraction of cold electrons and the relativistic component.

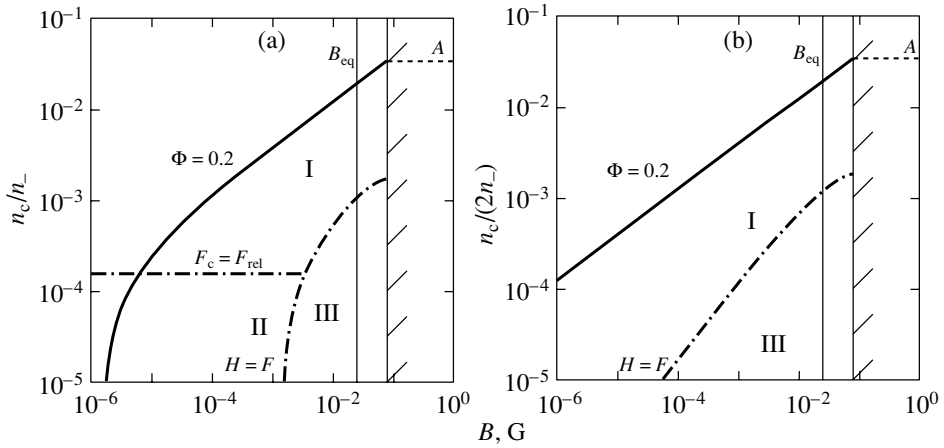

Fig. 5. Same as Fig. 4 for component K3 of the blazar BL Lac: (a) for an electron–proton plasma and (b) for a plasma with equal relativistic electron and positron densities.

The typical ray path length L in the jet of BL Lac is 0.55 pc for the redshift $z = 0.07$ (Miller *et al.* 1978) and the adopted angular size $\theta = 0''.0004$ of component K3. According to Eqs. (38) and (39), an equipartition of energy between the particles and the magnetic field is then achieved at $B_{eq} = 3 \times 10^{-2}[\ln(\gamma_{max}/\gamma_{min})/5]^{2/7}$ G. The derived value of B_{eq} falls within range (3) of magnetic fields $B < B_{max} = 8 \times 10^{-2}$ G under consideration. Therefore, the energy transferred in the jet of BL Lac can be concentrated in both the particles (for $B < B_{eq}$) and the magnetic field (for $B > B_{eq}$).

The microquasar GRS 1915+105. The radio observations by Mirabel and Rodriguez (1994) revealed superluminal motion of bright components away from the core of this source, indicative of relativistic velocities in the microquasar. In contrast to blazars, both oppositely directed jets are detected in the microquasar GRS 1915+105.

We will calculate the plasma parameters in the jet approaching the observer using the observations of component SE performed by Fender *et al.* (1999) on October 31, 1997, 2 days after its ejection. Its flux density at 5 GHz $F_{\nu obs}$ was 0.08 Jy. We assume the angular size of the component to be equal to the typical beam width of the antenna system, $0''.04$ (Fender *et al.* 1999).[7] The observed angular velocity of the separation of symmetric components SE and NW in the approaching and receding jets yields a Doppler factor $\delta \approx 0.34$ for component SE (Fender *et al.* 1999) for a distance d to the microquasar of 11 kpc.

The multifrequency observations of the microquasar with a low angular resolution performed by Rodriguez *et al.* (1995) and Fender *et al.* (2002) (without identifying the individual components) both before and after the ejection of component SE under consideration point to significant variations in the spectral index α during the first days after the ejection of another plasma blob (up to negative values of α corresponding to an inverted spectrum). As a result, a typical value of $\alpha = 0.8$ is usually established, which we will take for our calculations.

In the observations by Rodriguez *et al.* (1995) on March 24, 1994, when the radiation from the microquasar was determined by the jet approaching the observer, the polarization plane of the radiation was kept constant within $\pm 9°$ at frequencies of 4.9, 8.4, and 15 GHz. The possible rotation of the polarization plane through a typical angle of $\Delta\chi = 10°$ at $\nu_{obs} = 5$ GHz corresponds to a rotation measure of $RM_{obs} \approx 5 \times 10^{-3}$ rad cm^{-2} (Fender *et al.* 1999). For component SE, this value corresponds to a Faraday depth of $F \approx 0.7$ (see Eqs. (18) and (19)). This rotation measure agrees in order of magnitude with the more recent observations by Fender *et al.* (2002), in which the angle between the polarization planes when passing from 4.8 to 8.6 GHz changes in the range from 0° to 30°, and, hence, the rotation measure did not exceed 2×10^{-2} rad cm^{-2}.

For the above parameters, the brightness temperature of the radiation from component SE is $T_{rad\ obs} \approx 2.4 \times 10^6$ K in the observer's frame and $T_{rad} \approx 7.2 \times 10^6$ K in the frame of the jet (see Eqs. (8) and (11)). The relative content of cold electrons then

[7] The point is that there are no clear indications of the angular size of component SE in the paper by Fender *et al.* (1999): they consider both a continuous jet and a localized component with angular sizes that are several times smaller than the antenna beam width. At the same time, the previous observations of GRS 1915+105 by Mirabel and Rodriguez (1994) suggest that the typical diameters of the components were several tens of milliarcseconds several days after their ejection.

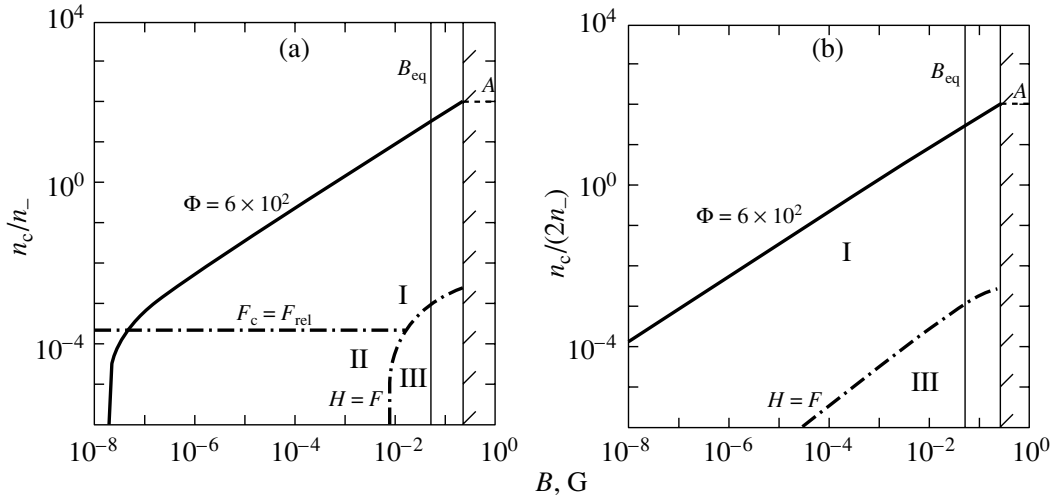

Fig. 6. Same as Fig. 4 for component SE in the microquasar GRS 1915+105: (a) for an electron–positron plasma and (b) for a plasma with equal relativistic electron and positron densities.

does not exceed $[n_c/(n_- + n_+)]_{max} = 10^2$ (Eq. (21)). Such a high value of $[n_c/(n_- + n_+)]_{max}$ suggests that the relative cold electron density in microquasar jets could be much higher than that in blazars and, probably, exceeds significantly the content of relativistic particles.

The cold electron density n_c is lower than the relativistic particle density $n_- + n_+$ only if the magnetic field $B < 8 \times 10^{-4}$ G for the chosen $\gamma_{min} = 10^2$. For such a magnetic field, the ratio $n_c/(n_- + n_+)$ defined by Eq. (20) is less than unity for any plasma composition.

To obtain the $n_c/(n_- + n_+) - B$ diagram for component SE (see Fig. 6), $\Phi = 6 \times 10^2$ (26) and $B_{max} \approx 2 \times 10^{-1}$ G (3) should be taken in the universal diagram at $\alpha = 0.8$ (see Fig. 3). The admissible parameters in Fig. 6 lie below solid line (20) specified by $\Phi = 6 \times 10^2$ (26). This line encloses all regions I, II, and III with different polarization of the normal waves. Consequently, the polarization of the normal waves in the jet can be determined by both the cold and relativistic electrons (and, possibly, positrons).

The diagrams in Fig. 6 were extended to a magnetic field strength of $B = 10^{-8}$ G to indicate the intersection of solid line (20) with the horizontal axis $n_c/(n_- + n_+) = 0$. At the same time, it is unlikely that the magnetic field in the microquasar jet is weaker than the interstellar magnetic field of several microgauss.

The typical ray path length in component SE is $L \approx 2 \times 10^{-3}$ pc for an assumed distance to the microquasar of $d \approx 11$ kpc. In this case, the magnetic field B_{eq} (38) that corresponds to an equipartition of energy between the magnetic field and the particles is 5×10^{-2} G. Since this value of B_{eq} lies within the range of magnetic fields $B < B_{max}$ under consideration, whose upper limit $B_{max} \approx 2 \times 10^{-1}$ G is defined by Eq. (3), the bulk of the energy transferred in the jet of the microquasar GRS 1915+105 can be accounted for by both the relativistic particles and the magnetic field.

5. CONCLUSIONS

In the previous section, our analysis of the maximum relative content of cold electrons in the jets of the blazars 3C 279 and BL Lac led us to the conclusion (consistent with the results of the works by Wardle (1977) and Jones and O'Dell (1977b))[8] that the plasma in their jets is relativistic. However, despite their relatively low content, the cold electrons can determine the polarization and refractive indices of the normal electromagnetic waves in the radio sources. In contrast, in the jets of the microquasar GRS 1915+105, the cold electron density can exceed significantly the relativistic particle density. This is in agreement with the observations of hydrogen lines and lines of other elements from the jets of the microquasar SS 433 by Margon (1984), Kotani

[8] When these papers appeared, there were no observations of the radio sources with a sufficiently high angular resolution that would clearly separate the emissions from the jet and the core. Therefore, many parameters of the jets were unavailable. In particular, Wardle (1977) and Jones and O'Dell (1977b) disregarded the plasma motion in the jets with a relativistic velocity, which increases significantly the brightness temperature of the observed radiation compared to its value in the frame of the jet.

et al. (1994), and Fender *et al.* (2003), which are indicative of a normal plasma composition: a cold electron–proton plasma with an admixture of relativistic particles. The electron plasma component in the jets of the microquasar GRS 1915+105 can be relativistic only in the case of a weak magnetic field in the jets, $B < 8 \times 10^{-4}$ G.

The positron content in the jets cannot be judged from the radio observations considered here. Therefore, we emphasize the importance of low-frequency radio observations with a high angular resolution that would include frequencies of the order of and lower than the turnover frequency of the jet. Such observations allow the magnetic field strength to be estimated (as was done for component C4 of the quasar 3C 279) without resorting to any *a priori* judgments about the relationship between the particle and magnetic field energy densities in the jet. If the magnetic field in a jet is lower than the minimum possible value of Eq. (27) for a plasma without positrons, then this jet must necessarily contain positrons. At the same time, radio-astronomical data on the low-frequency turnover in the jet radiation spectrum allow definitive conclusions about the dynamics of the magnetized plasma in the jet to be also reached.

In principle, the presence of positrons cannot be ruled out owing to the assumption of profound processing of the accreting plasma in the vicinity of a black hole, near the event horizon, followed by the ejection of this plasma in the form of jets. At the same time, note the detection of relativistic jets in the Galactic object Cir X-1, which is an accreting neutron star rather than a black hole (Fender *et al.* 2004). At least, the appearance of an electron–positron plasma in the relativistic jets of this object seems unlikely.

Our calculations did not include the data on weak circular polarization of the radiation from blazar and microquasar jets (see, e.g., Wardle *et al.* 1998; Fender *et al.* 2002), mainly because the generation mechanism of such polarization is unclear. In a uniform magnetic field, circular polarization arises only if the electron density is higher than the positron density. At the same time, in a nonuniform magnetic field (in the presence of a shear), circular polarization also emerges in an electron–positron plasma (see Zheleznyakov and Koryagin 2002; Zheleznyakov *et al.* 1983). Therefore, to interpret the circular polarization of the synchrotron radiation and to invoke it to determine the corpuscular composition of the plasma in jets, it is important to know the magnetic field structure in the source. This, in particular, requires observations with a higher angular resolution that would allow the transverse jet structure to be determined.

ACKNOWLEDGMENTS

This work was supported by the Russian Foundation for Basic Research (project no. 05-02-17525), the Council for Grants from the Presidential program "In Support of Young Russian Scientists and Leading Scientific Schools" (project nos. NSh-1744.2003.2 and MK-2161.2003.02), the "Nonstationary Phenomena in Astronomy" program of the Presidium of the Russian Academy of Sciences, and the "Astronomy" program of the Ministry of Industry, Science, and Technology (contract 40.022.1.1.1102).

REFERENCES

1. H. Bloemen, K. Bennett, J. J. Blom, *et al.*, Astron. Astrophys. **293**, L1 (1995).
2. J. J. Blom, K. Bennett, H. Bloemen, *et al.*, Astron. Astrophys. **298**, L33 (1995).
3. M. Boettcher and R. Schlickeiser, Astron. Astrophys. **302**, L17 (1995).
4. M. Boettcher and R. Schlickeiser, Astron. Astrophys., Suppl. Ser. **120**, 575 (1996).
5. E. M. Burbidge and F. D. Rosenberg, Astrophys. J. **142**, 1673 (1965).
6. M. H. Cohen, W. Cannon, G. H. Purcell, *et al.*, Astrophys. J. **170**, 207 (1971).
7. G. R. Denn, R. L. Mutel, and A. P. Marscher, Astrophys. J., Suppl. Ser. **129**, 61 (2000).
8. R. P. Fender, S. T. Garrington, D. J. McKay, *et al.*, Mon. Not. R. Astron. Soc. **304**, 865 (1999).
9. R. P. Fender, D. Rayner, D. G. McCormick, *et al.*, Mon. Not. R. Astron. Soc. **336**, 39 (2002).
10. R. Fender, S. Migliari, and M. Mendez, New Astron. Rev. **47**, 481 (2003).
11. R. Fender, K. Wu, H. Johnston, *et al.*, Nature **427**, 222 (2004).
12. D. C. Gabuzda and T. V. Cawthorne, Mon. Not. R. Astron. Soc. **319**, 1056 (2000).
13. D. C. Gabuzda and V. A. Chernetskiĭ, Mon. Not. R. Astron. Soc. **339**, 669 (2003).
14. R. C. Hartman, M. Böttcher, G. Aldering, *et al.*, Astrophys. J. **553**, 683 (2001).
15. T. W. Jones and S. L. O'Dell, Astrophys. J. **214**, 522 (1977a).
16. T. W. Jones and S. L. O'Dell, Astron. Astrophys. **61**, 291 (1977b).
17. C. R. Kaiser and D. C. Hannikainen, Mon. Not. R. Astron. Soc. **330**, 225 (2002).
18. T. Kotani, N. Kawai, T. Aoki, *et al.*, Publ. Astron. Soc. Jpn. **46**, L147 (1994).
19. B. Margon, Annu. Rev. Astron. Astrophys. **22**, 507 (1984).
20. J. S. Miller, H. B. French, and S. A. Hawley, Astrophys. J. Lett. **219**, L85 (1978).
21. I. F. Mirabel and L. F. Rodriguez, Nature **371**, 46 (1994).
22. A. G. Pacholczyk, Mon. Not. R. Astron. Soc. **163**, 29P (1973).
23. U. Pen, Astrophys. J., Suppl. Ser. **120**, 49 (1999).

24. B. G. Piner, P. G. Edwards, A. E. Wehrle, *et al.*, Astrophys. J. **537**, 91 (2000).
25. B. G. Piner, S. C. Unwin, A. E. Wehrle, *et al.*, Astrophys. J. **588**, 716 (2003).
26. C. Reynolds, T. V. Cawthorne, and D. C. Gabuzda, Mon. Not. R. Astron. Soc. **327**, 1071 (2001).
27. L. F. Rodriguez, E. Gerard, I. F. Mirabel, *et al.*, Astrophys. J., Suppl. Ser. **101**, 173 (1995).
28. V. N. Sazonov, Zh. Éksp. Teor. Fiz. **56**, 1075 (1969) [Sov. Phys. JETP **56**, 578 (1969)].
29. M. Sikora, M. Blazejowski, R. Moderski, and G. M. Madejski, Astrophys. J. **577**, 78 (2002).
30. J. G. Skibo, C. D. Dermer, and R. Schlickeiser, Astrophys. J. **483**, 56 (1997).
31. A. M. Stirling, T. V. Cawthorne, J. A. Stevens, *et al.*, Mon. Not. R. Astron. Soc. **341**, 405 (2003).
32. G. B. Taylor, Astrophys. J. **506**, 637 (1998).
33. S. C. Unwin, A. E. Wehrle, A. P. Lobanov, *et al.*, Astrophys. J. **480**, 596 (1997).
34. C. M. Urry and P. Padovani, Publ. Astron. Soc. Pac. **107**, 803 (1995).
35. R. C. Vermeulen, P. M. Ogle, H. D. Tran, *et al.*, Astrophys. J. Lett. **452**, L5 (1995).
36. J. F. C. Wardle, Nature **269**, 563 (1977).
37. J. F. C. Wardle, D. C. Homan, R. Ojha, and D. H. Roberts, Nature **395**, 457 (1998).
38. A. E. Wehrle, B. G. Piner, S. C. Unwin, *et al.*, Astrophys. J., Suppl. Ser. **133**, 297 (2001).
39. A. R. Whitney, I. I. Shapiro, A. E. E. Rogers, *et al.*, Science **173**, 225 (1971).
40. R. T. Zavala and G. B. Taylor, Astrophys. J. Lett. **566**, L9 (2002).
41. R. T. Zavala and G. B. Taylor, Astrophys. J. **589**, 126 (2003a).
42. R. T. Zavala and G. B. Taylor, New Astron. Rev. **47**, 589 (2003b).
43. V. V. Zheleznyakov, *Radiation in Astrophysical Plasmas* (Kluwer Academic Publishers, Dordrecht, 1996).
44. V. V. Zheleznyakov and S. A. Koryagin, Pis'ma Astron. Zh. **28**, 809 (2002) [Astron. Lett. **28**, 727 (2002)].
45. V. V. Zheleznyakov, V. V. Kocharovskiĭ, and Vl. V. Kocharovskiĭ, Usp. Fiz. Nauk **141**, 257 (1983) [Sov. Phys. Usp. **26**, 877 (1983)].

Translated by V. Astakhov

Astronomy Letters, Vol. 31, No. 11, 2005, pp. 729–747. Translated from Pis'ma v Astronomicheskiĭ Zhurnal, Vol. 31, No. 11, 2005, pp. 819–839.

Hard Spectra of X-ray Pulsars from INTEGRAL Data

E. V. Filippova[1*], S. S. Tsygankov[1], A. A. Lutovinov[1], and R. A. Sunyaev[1,2]

[1] *Space Research Institute, Russian Academy of Sciences, Profsoyuznaya ul. 84/32, Moscow, 117810 Russia*

[2] *Max-Planck-Institut für Astrophysik, Karl-Schwarzschild-Str. 1, Postfach 1317, D-85741 Garching, Germany*

Received May 16, 2005

Abstract—We present spectra for 34 accretion-powers X-ray pulsars and one millisecond pulsar that were within the field of view of the INTEGRAL observatory over two years (December 2002–January 2005) of its in-orbit operation and that were detected by its instruments at a statistically significant level ($> 8\sigma$ in the energy range 18–60 keV). There are seven recently discovered objects of this class among the pulsars studied: 2RXP J130159.6–635806, IGR/AX J16320–4751, IGR J16358–4726, AX J163904–4642, IGR J16465–4507, SAX/IGR J18027–2017, and AX J1841.0–0535. We have also obtained hard X-ray (>20 keV) spectra for the accretion-powered pulsars RX J0146.9+6121, AX J1820.5–1434, and AX J1841.0–0535 for the first time. We analyze the evolution of spectral parameters as a function of the intensity of the sources and compare these with the results of previous studies. © *2005 Pleiades Publishing, Inc.*

Key words: *X-ray pulsars, neutron stars, spectra.*

INTRODUCTION

Accretion-powered X-ray pulsars were discovered more than 30 years ago (Giacconi *et al.* 1971), and some 100 such objects are known to date. A qualitative understanding of the nature of the observed pulsed emission came almost at once (see, e.g., Pringle and Rees 1972; Lamb *et al.* 1973). X-ray pulsars are rapidly rotating neutron stars with a strong magnetic field ($B > 10^{11}$ G) that are members of binary systems and that accrete matter from their stellar companion. As the plasma approaches a neutron star, it is stopped by the pressure of the magnetic field (which, to a first approximation, is in the form of a dipole), is frozen into the latter, and moves along the field lines toward the magnetic poles of the star to produce two hot spots (at these locations, the captured matter releases its gravitational energy in the form of X-ray and gamma-ray radiation). If the rotation axis of the neutron star does not coincide with its magnetic axis (an oblique rotator), then these spots will periodically cross the line of sight at a certain orientation of the binary relative to a remote observer and, thus, give rise to pulsed emission.

X-ray pulsars are a unique laboratory for studying the behavior of matter under extreme conditions—at high temperatures and in strong magnetic and gravitational fields. Analysis of their energy spectra gives an idea of the physical processes in the emitting region, the structure of the accreting matter, and the parameters of the compact object. For example, the detection of cyclotron lines in the spectrum of a pulsar allows the magnetic field of a neutron star to be measured (Gnedin and Sunyaev 1974). The magnetic field was first measured by this method for the pulsar Her X-1 (Truemper *et al.* 1978).

Many papers devoted to various sources of this class have been published over the period of research on X-ray pulsars; here, we mention only a few review articles in which particular properties of these objects were discussed. Such an attempt was first made by White *et al.* (1983), who summarized the spectra and pulse profiles for the then known X-ray pulsars and suggested an empirical model to describe their spectra. Subsequently, Nagase (1989) gave an overview of accretion-powered pulsars using new Hakucho, TENMA, EXOSAT, and GINGA observations. Based on data from the KVANT module, Gilfanov *et al.* (1989) analyzed the evolution of the pulsation periods for pulsars. GRANAT (Lutovinov *et al.* 1994) and ComptonGRO (Bildsten *et al.* 1997) data were used to investigate in detail the pulse profiles and the evolution of the pulsation periods. Coburn *et al.* (2002) and Orlandini and Dal Fiume (2001) used, respectively, RXTE and BeppoSAX data to analyze the pulsars whose spectra exhibited the cyclotron lines attributable to the resonant scattering of photons by electrons in a magnetic field; in certain cases, several harmonics were detected from objects.

*E-mail: kate@hea.iki.rssi.ru

Despite the long period of research, as yet there is no convincing theoretical model that would describe the spectra of accretion-powered X-ray pulsars. The most popular model used to fit the spectra yields a power-law spectral shape with an exponential cutoff (models (1) and (2) in Data Analysis). For most sources, the photon index, the cutoff energy, and the e-folding energy lie within the ranges 0.3–2, 7–30, and 9–40 keV, respectively. The sensitivity of the IBIS instrument at these energies is well suited for determining the e-folding energy in the spectrum. The spectra also often exhibit the following: low-energy absorption that can be attributed both to the interstellar medium and to internal absorption in the binary system with the column density $N_{\rm H}$ varying within the range 10^{21}–10^{24} atoms cm^{-2}, iron emission lines at 6–7 keV, and gyrolines at the energies corresponding to the electron cyclotron frequency and its harmonics.

The INTEGRAL observatory, whose main instruments have a high sensitivity and a large field of view, allows one not only to study known sources, but also to discover new objects, including X-ray pulsars, and to analyze their behavior over a wide energy range. In this paper, we provide an overview of the X-ray pulsars observed by the INTEGRAL observatory and construct their broadband spectra. Some 70 known and recently discovered pulsars were within the field of view of the INTEGRAL instruments. For 35 of these, we were able to reconstruct their energy spectra; the remaining sources were either not detected, or detected but the data on these are not publicly accessible at present (e.g., the pulsar 4U 0115+63 from which the INTEGRAL observatory detected an outburst in August 2004; see Lutovinov *et al.* 2004a).

OBSERVATIONS

The international gamma-ray observatory INTEGRAL (Winkler *et al.* 2003) was placed in orbit by a Russian Proton launcher on October 17, 2002 (Eismont *et al.* 2003). It carries four instruments: the SPI gamma-ray spectrometer, the IBIS gamma-ray telescope, the JEM-X X-ray monitor, and the OMC optical monitor, which allow the emission from astrophysical objects to be analyzed over a wide wavelength range. In this paper, we use data from the ISGRI detector of the IBIS telescope (Ubertini *et al.* 2003) and from the JEM-X monitor. Both instruments operate on the principle of a coded aperture. The ISGRI effective energy range is 20–200 keV (the energy resolution is ~7% at 100 keV), the field of view is 29° × 29° (the fully coded zone is 9° × 9°), and the nominal space resolution is ~12′ (the angular size of the mask element). A more detailed description of the detector can be found in Lebrun *et al.* (2003). The JEM-X monitor consists of two identical modules, JEM-X1 and JEM-X2 (Lund *et al.* 2003). Each of the modules of the telescope has the following technical characteristics: the energy range is 3–35 keV, the field of view (the fully coded zone) is 13.°2 (4.°8) in diameter, the geometrical area of the detector is 500 cm^2, and the nominal space resolution is ~3′.

Here, we used the INTEGRAL observations from orbit 23 (MJD 52 629, December 21, 2002) to orbit 239 (MJD 53 276, September 28, 2004); these are the currently publicly accessible data and the data of the Russian quota obtained as part of the Galactic plane scanning (GPS), the Galactic center deep exploration (GCDE), and the observations in the "General Program". Only the publicly accessible observations of the X-ray pulsar V0332+53 that were performed from orbit 272 (MJD 53 376, January 6, 2005) to orbit 278 (MJD 53 394, January 24, 2005) constitute an exception.

DATA ANALYSIS

For all of the detected X-ray pulsars, we constructed light curves in the energy range 18–60 keV and analyzed their variability. We constructed average spectra for persistent sources and analyzed the dependence of the spectrum on the source's state for pulsars with variable fluxes: if the spectrum did not change, we also provided an average spectrum; otherwise, we gave the spectra of different states. The fluxes from the pulsars determined from these light curves are given in mCrabs (1 mCrab = 1.36 × 10^{-11} erg cm^{-2} s^{-1} in the energy range 18–60 keV under the assumption of a power-law spectrum for the Crab Nebula with an index of 2.1 and a normalization of 10 at 1 keV).

The image reconstruction method and the spectral analysis of the ISGRI/IBIS data used here were described by Revnivtsev *et al.* (2004) and Lutovinov *et al.* (2003a). Analysis of a large number of calibration observations for the Crab Nebula revealed that the method yields a systematic error in measuring the absolute flux from the source of ~10% over a wide energy range and that the spectral shape is reconstructed with an accuracy up to 2–5%. To take into account this peculiarity, we added a systematic error of 5% when analyzing the spectra in the XSPEC package. As an example, Fig. 1 shows the energy spectrum for the Crab Nebula reconstructed by this method from the data of orbit 170. The response matrix was constructed from the data of orbit 102. In fitting this spectrum by a power law, we added a systematic error of 2% and obtained the following parameters: $\Gamma = 2.13 \pm 0.02$ and Norm $= 11.27 \pm 0.35$. All of the errors given here are statistical and correspond to one standard deviation.

The data of the Russian quota for the pulsar were arbitrarily divided into two groups, before and after orbit 200, because our ISGRI response matrix was constructed from calibration measurements of the Crab Nebula. After orbit 200, the flux (in counts) from the Crab Nebula increased due to a change in the ISGRI operating parameters; our response matrix constructed from the data of orbit 239 changed accordingly. We reconstructed the spectra separately for each data group and analyzed the variability of their shape.

For our spectral analysis of the JEM-X data, we used the standard OSA 4.2 software package provided by the INTEGRAL Science Data Center (http://isdc.unige.ch). It should be borne in mind that the JEM-X field of view is considerably smaller than the IBIS one. Therefore, the effective exposure for the observations of sources by this instrument is also shorter and, in certain cases, no sources fell within its field of view or the sensitivity of the instrument was not enough for their detection at a statistically significant level.

Since the absolute fluxes from the sources are reconstructed from the JEM-X data not quite accurately, the normalization of the JEM-X data was left free when simultaneously fitting the JEM-X and ISGRI spectra of the sources in the XSPEC package. It is also worth mentioning that there are a number of features near energies 5–7 keV in the spectra reconstructed from the JEM-X data that are attributable to the flaws in the current response matrix of the instrument. These features make it difficult to study in detail a source's spectrum, in particular, to identify the iron emission line and to determine its parameters[1].

To fit the spectra, we used a standard (for pulsars) empirical model that includes a power law with a high-energy cutoff (White *et al.* 1983):

$$\mathrm{PLCUT}(E) = AE^{-\Gamma} \times \begin{cases} 1, & E \le E_{\mathrm{cut}} \\ \exp^{-(E-E_{\mathrm{cut}})/E_{\mathrm{fold}}}, & E > E_{\mathrm{cut}}, \end{cases} \quad (1)$$

where Γ is the photon index and E_{cut} and E_{fold} are the cutoff energy and the e-folding energy, respectively. For several pulsars for which we failed to set a reasonable limit on the parameter E_{cut} when fitting their spectra by model (1), we used the following model:

$$\mathrm{CUTOFF}(E) = AE^{-\Gamma} \times \exp^{-E/E_{\mathrm{fold}}}. \quad (2)$$

In certain cases, the standard model did not describe the pulsar's spectral shape quite accurately.

[1]Private correspondence with Carol Anne Oxborrow and Peter Kretschmar.

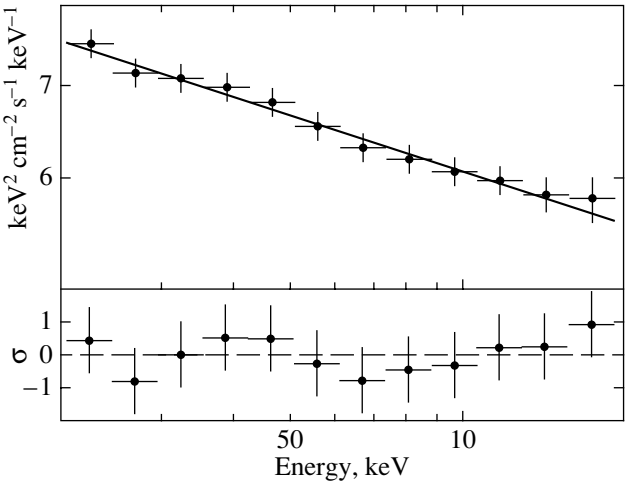

Fig. 1. Energy spectrum for the Crab Nebula. The solid line represents the power-law best fit to the spectrum with the following parameters: $\Gamma = 2.130 \pm 0.002$ and Norm $= 11.27 \pm 0.35$. The errors correspond to one standard deviation.

Therefore, we introduced additional components when fitting the spectrum:

—low-energy photoelectron absorption described by the formula

$$\mathrm{WABS}(E) = \exp(-N_{\mathrm{H}} \times \sigma(E)), \quad (3)$$

where $\sigma(E)$ is the cross section for the process (Morrison and McCammon 1983);

—an iron emission line described by a Gaussian profile

$$\mathrm{GAUS}(E) = \frac{A}{\sqrt{(2\pi)\sigma_{\mathrm{Fe}}}} \times \exp\{(-[(E - E_{\mathrm{Fe}})/2\sigma_{\mathrm{Fe}}]^2\}, \quad (4)$$

where E_{Fe} is the line center and σ_{Fe} is the line width;

—a resonance cyclotron absorption line whose model is

$$\mathrm{CYCL}(E) = \frac{\exp[-\tau_{\mathrm{cycl}}(\sigma_{\mathrm{cycl}}/E_{\mathrm{cycl}})^2]}{(E - E_{\mathrm{cycl}})^2 + \sigma_{\mathrm{cycl}}^2}, \quad (5)$$

where E_{cycl} is the line center, τ_{cycl} is the line depth, and σ_{cycl} is the line width.

To find features related to the resonance cyclotron absorption line in the radiation spectrum for those sources in which this feature was not observed previously, we added the corresponding component to the model fit (see above). The energy of the line center E_{cycl} was varied over the range 20–90 keV at 5-keV steps, while the line width was fixed at 5 keV. The choice of an energy range for the search of these lines was dictated by the presence of systematic features

in the JEM-X response matrix and by the fact that the standard X-ray range has been well studied using data from other missions. We found the most probable position of the possible cyclotron line and its significance in units of the standard deviation using the $\Delta\chi^2$ test.

RESULTS

The X-ray pulsars that fell within the field of view of the INTEGRAL observatory and that were detected at a statistically significant level by its instruments are listed in Table 1. This table also gives their parameters, the parameters of the corresponding binaries, and references to the papers from which these were taken (P is the spin period of the neutron star, $P_{\rm orb}$ is the orbital period of the binary, HMXB stands for a high-mass X-ray binary, and LMXB stands for a low-mass X-ray binary). The spectra of the sources are shown in Fig. 2, and the best-fit parameters for the spectra are presented in Tables 2 and 3. Table 2 gives the parameters for the standard model and lists the exposures of the observations from which the average spectrum was constructed and the fluxes from the pulsars in the energy ranges 6–20 and 18–60 keV determined by analyzing the spectra. Table 3 gives the parameters of the models that describe the features in the spectra of the pulsars, more specifically, the iron emission line and the cyclotron absorption line and its harmonics. Below, we briefly describe the results obtained for each of the pulsars.

A0114+650. The X-ray pulsar A0114+650 is one of the longest-period accretion-powered pulsars. The data from January through July 2003 (MJD 52 653–52 835) were used to analyze the source. The source was not detected in the observations performed from MJD 52 653 to MJD 52 655; the upper (1σ) limit on its 18–60 keV flux was 1 mCrab. In the remaining time, the mean flux in the same energy range was ~8 mCrab. The pulsar's average spectrum was reconstructed from these observations. Since JEM-X did not detect the source, we were able to reconstruct its spectrum only in the hard X-ray energy range. The pulsar's spectrum is typical of this class of objects and is described in the soft X-ray energy range by a power law with a high-energy cutoff with the following parameters: $\Gamma \sim 1.3$, $E_{\rm cut} \sim 8$ keV, and $E_{\rm fold} \sim 20$ keV (Bonning and Falanga, 2005, Masetti *et al.* 2005). Since the IBIS exposure for the source was short, we failed to fit the spectrum obtained by models (1) or (2); therefore, it was fitted by a simple power law with an index of 2.3 ± 0.4.

SMC X-1 (4U 0115–73). The source SMC X-1 was within the JEM-X/IBIS field of view during the observations of the Small Magellanic Cloud region from July 24 through July 27, 2003 (MJD 52 843–52 846).

We used standard model (1) in our spectral analysis. Fitting the spectrum by this model yielded the parameters given in Table 2. Moon *et al.* (2003) showed the constancy of the spectral parameters with the source's flaring activity, which is also confirmed by their agreement with our parameters. However, note a slightly higher e-folding energy in the source's spectrum obtained from the INTEGRAL data. Based on our spectral analysis, we also obtained an upper limit on the presence of a resonance cyclotron absorption line in the source's spectrum by the method described in the section Data Analysis. No such feature was found at a confidence level higher than $\sim 1\sigma$.

RX J0146.9+6121. To analyze the source RX J0146.9+6121, we used the publicly accessible INTEGRAL observations covering the period from MJD 52 636 to MJD 53 018. Because of the low flux from the source (in the energy range 18–60 keV, it was ~3 mCrab), the JEM-X monitor did not detect the pulsar in this period. Since the source is weak, we used a simple power law with the estimated photon index $\Gamma = 2.9^{+1.1}_{-0.8}$ to fit its spectrum. It should be noted that the hard X-ray spectrum of the source has not been analyzed until now.

V0332+53. As part of the Galactic plane scanning by the INTEGRAL observatory, its instruments detected an intense X-ray outburst from the source V0332+53 that began at the very end of 2004 (Swank *et al.* 2004). In this paper, we analyze the observations performed by the INTEGRAL observatory from January 6 through January 24, 2005 (MJD 53 376–53 394), with a total exposure of ~180 ks. In this period, the source was in a very bright state and its 18–60 keV flux did not fall below ~350 mCrab.

In our analysis, the model fit was chosen using the results of previous studies and consisted of a power law with low-energy absorption (the hydrogen column density was taken from Makishima *et al.* 1990), a high-energy cutoff, and three resonance cyclotron absorption lines ($E_{\rm cycl1} = 24.25$ keV, $E_{\rm cycl2} = 46.8$ keV, $E_{\rm cycl3} = 67.9$ keV). The derived positions of the cyclotron lines are confirmed by the analysis of RXTE data (Coburn *et al.* 2005) and the first ~100 ks of INTEGRAL observations of the pulsar under study (Kreykenbohm *et al.* 2005).

As the X-ray luminosity of the pulsar decreased, we found a change in the shape of its radiation spectrum. Thus, for example, when the mean 3–100 keV luminosity of the source fell from 14.9×10^{37} to 5.2×10^{37} erg s^{-1}, the photon index in the model used slightly decreased (from 0.76 ± 0.03 to 0.59 ± 0.03), but the cutoff parameters remained the same, within

Table 1. List of pulsars

Name	Binary type	P, s	P_{orb}, days	Companion type	References
A0114+650	HMXB	10008	11.6	B1 Ia	[1], [2], [3]
SMC X-1	HMXB	0.71	3.89	B0	[4], [5], [6]
RX J0146.9+6121	HMXB	1408	–	B5IIIe	[7], [8]
V0332+53	HMXB	4.4	34.25	O8–9Ve	[9], [10]
4U 0352+309	HMXB	837	–	Be(XPer)	[11]
LMC X-4	HMXB	13.5	1.4	07 III–V	[12], [13], [14]
A0535+260	HMXB	103	111	O9.7 IIIe Be	[15], [16], [17]
Vela X-1	HMXB	283	8.96	B0.5Ib	[18], [19]
CEN X-3	HMXB	4.82	2.1	O6–8f	[20], [21]
4U 1145–619	HMXB	292	187	B1Vne	[22], [23]
1E 1145.1–6141	HMXB	297	14.365	B2Iae	[24], [25]
GX 301-2	HMXB	680	41.5	Be	[26], [27]
2RXP J130159.6–635806	HMXB?	704	–	–	[28]
4U 1538–52	HMXB	528	3.7	B0Iab	[29], [30]
4U 1626–67	LMXB	7.66	0.0289	low-mass dwarf	[31], [32]
IGR/AX J16320–4751	HMXB	1300	–	–	[33], [34]
IGR J16358–4726	HMXB	5980	–	–	[35], [36]
AX J163904–4642	HMXB	900	–	–	[37]
IGR J16465–4507	HMXB	228	–	–	[35]
OAO 1657–415	HMXB	37.7	10.4	B0–6Iab	[38], [39]
EXO 1722–363	HMXB	413	9.7	Be?	[40], [41]
GX 1+4	LMXB	115	303.8	M6III	[42], [43], [44]
SAX/IGR J18027–2017	HMXB	139	4.6	–	[45], [46]
XTE J1807–294	LMXB	0.00525	0.0278	–	[47], [48]
AX J1820.5–1434	HMXB	152.3	–	Be?	[49]
AX J1841.0–0535	HMXB	4.74	–	Be	[50], [51]
GS 1843+009	HMXB	29.477	–	B0–B2 IV–Ve	[52], [53], [54]
A1845–024	HMXB	94.8	242	–	[55], [56], [57]
XTE J1855–026	HMXB	360.741	6.067	–	[58], [59]
XTE 1858	HMXB	221	–	–	[60]
X1901+031	–	2.763	–	–	[61], [62]
4U 1907+097	HMXB	438	8.38	B I	[63], [64], [65]
KS 1947+300	HMXB	18.7	40.415	B0Ve	[66], [67], [68], [69]
EXO 2030+375	HMXB	41.7	46	Be	[70], [71]
SAX J2103.5+4545	HMXB	355	12.68	O–B	[72], [73]

Note: [1] Finley *et al.* (1992); [2] Crampton *et al.* (1985); [3] Reig *et al.* (1996); [4] Price *et al.* (1971); [5] Reynolds *et al.* (1993b); [6] Levine *et al.* (1993); [7] Meregetti *et al.* (2000); [8] Slettebak (1985); [9] Stella *et al.* (1985); [10] Negueruela *et al.* (1999); [11] White *et al.* (1976); [12] Sanduleak and Philip (1976); [13] Li *et al.* (1978); [14] Kelley *et al.* (1983a); [15] Rosenberg *et al.* (1975); [16] Priedhorsky and Terrell (1983); [17] Giangrande *et al.* (1980); [18] van Kerkwijk *et al.* (1995); [19] Hiltner *et al.* (1972); [20] Kelley *et al.* (1983b); [21] Krzeminski (1974); [22] Warwick *et al.* (1985); [23] Stevens *et al.* (1997); [24] Ray and Chakrabarty (2002); [25] Ilovaisky *et al.* (1982); [26] Sato *et al.* (1986); [27] Parkes *et al.* (1980); [28] Chernyakova *et al.* (2005); [29] Clark (2000); [30] Parkes *et al.* (1978); [31] Chakrabarty *et al.* (2001); [32] McClintok *et al.* (1977); [33] Lutovinov *et al.* (2005b); [34] Rodriguez *et al.* (2003); [35] Lutovinov *et al.* (2005c); [36] Patel *et al.* (2003); [37] Walter *et al.* (2004); [38] Chakrabarty *et al.* (1993); [39] Chakrabarty *et al.* (2002); [40] Markwardt and Swank (2003); [41] Lutovinov *et al.* (2004b); [42] Lewin *et al.* (1971); [43] Pereira *et al.* (1999); [44] Sharma *et al.* (1993); [45] Augello *et al.* (2003); [46] Lutovinov *et al.* (2005a); [47] Markwardt *et al.* (2003); [48] Kirsch *et al.* (2004); [49] Kinugasa *et al.* (1998); [50] Bamba *et al.* (2001); [51] Halpen *et al.* (2004); [52] Koyama *et al.* (1990a); [53] Israel *et al.* (2001); [54] Piraino *et al.* (2000); [55] Koyama *et al.* (1990b); [56] Zhang *et al.* (1996); [57] Finger *et al.* (1999); [58] Corbet *et al.* (1999); [59] Corbet *et al.* (2002); [60] Takeshima *et al.* (1998); [61] Forman *et al.* (1976); [62] Galloway *et al.* (2003); [63] Marshall and Ricketts (1980); [64] van Kerkwijk *et al.* (1989); [65] Iye (1986); [66] Borozdin *et al.* (1990); [67] Galloway *et al.* (2004); [68] Tsygankov *et al.* (2005b); [69] Negueruela *et al.* (2003); [70] Stollberg *et al.* (1999); [71] Coe *et al.* (1988); [72] Baykal *et al.* (2000); [73] Filippova *et al.* (2004).

Table 2. Exposure times, fluxes, and best-fit parameters for the spectra of the pulsars

Pulsar name	Exposure time, ks		Flux, 10^{-9} erg cm^{-2} s^{-1}		N_H, 10^{22} cm^{-2}	Photon index Γ	E_{cut}, keV	E_{fold}, keV	χ^2
	JEM-X	IBIS	6–20 keV	18–60 keV					
A0114+650	–	40.4	–	0.09	–	2.3 ± 0.4	–	–	0.42(6)
SMC X-1	70	104	1.05	0.76	–	1.48 ± 0.02	$20.5^{+1.0}_{-1.8}$	$12.9^{+0.6}_{-0.7}$	0.98(124)
RX J0146.9+6121	–	250	–	0.03	–	$2.9^{+1.1}_{-0.8}$	–	–	0.31(3)
V0332+53	178	187.4	17.87	6.22	4[a]	0.77 ± 0.02	$24.3^{+0.5}_{-0.7}$	$14.0^{+0.5}_{-0.7}$	0.35(127)
4U 0352+309	–	50	–	0.56	–	1.92 ± 0.19	50 ± 16	77 ± 27	0.36(9)
LMC X-4	93	176	0.79	0.78	–	0.2 ± 0.15	9.1 ± 0.8	11.0 ± 0.6	0.93(117)
A 0535+26	–	77	–	0.24	–	1.2[a]	24[a]	$13.8^{+4.5}_{-3.2}$	0.07(5)
Vela X-1 (eclipse)	–	203.6	–	0.1	–	3.1 ± 0.3	–	–	0.83(7)
Vela X-1 (outside eclipse)	897.2	560	3.2	3.6	–	0.88 ± 0.01	25.5 ± 0.2	13.0 ± 0.1	0.34(131)
CEN X-3 (quiescent state)	266.1	250	0.39	0.2	–	0.87 ± 0.06	16.4 ± 0.6	7.1 ± 0.2	1.5(120)
CEN X-3 (outbursts)	15	47	1.57	0.66	–	1.16 ± 0.04	15.3 ± 0.2	7.8 ± 0.2	1.4(116)
4U 1145–619	11	77.3	0.39	0.33	–	1.5 ± 0.1	6.7 ± 1.4	30 ± 4	1(142)
1E 1145.1–614	11	345.2	0.39	0.4	3.3[a]	1.08 ± 0.07	8 ± 1	$21.9^{+1.8}_{-0.8}$	0.98(139)
GX 301–2 (high state)	–	31	–	6.04	–	$0.74^{+0.32}_{-0.09}$	$23.3^{+0.3}_{-0.5}$	8.3 ± 0.7	0.74(8)
GX 301–2 (low state)	62	710	0.96	0.99	10.6 ± 2.5	0.30 ± 0.06	17.8 ± 0.2	9.7 ± 0.7	0.9(118)
2RXP130159.6–635806	–	10.3	–	0.2[c]	2.56[a]	0.69[a]	24.3 ± 3.4	$8.5^{+0.2}_{-0.1}$	–[d]
4U 1538–52	23	894.4	0.46	0.2	1.63[a]	1.37 ± 0.06	28.7 ± 0.8	9.9 ± 0.7	0.94(119)
4U 1626–67	–	218.2	–	0.15	–	0.87[a]	$23.9^{+1.0}_{-1.4}$	7 ± 1	1.25(5)
IGR/AX J16320–4752[b]	–	1000	–	0.2[c]	18[a]	0.7 ± 0.2	–	13 ± 1	–[d]
IGR J16358–4726[b]	–	1000	–	0.04[c]	40[a]	0.7 ± 0.5	–	16 ± 5	–[d]
AX J163904–4642[b]	–	1000	–	0.06[c]	58[a]	1.3 ± 1.0	–	11 ± 1	–[d]
IGR J16465–4507[b]	–	1000	–	0.12[c]	72[a]	1.0 ± 0.5	–	30[a]	–[d]
OAO 1657–415	29	1663.7	0.8	1.03	$15.2^{+0.7}_{-1.4}$	1.57 ± 0.02	$26.3^{+0.7}_{-1.8}$	$29.2^{+1.2}_{-0.5}$	0.73(119)
EXO 1722–363	–	2960.9	–	0.6	–	3.5[a]	–	–	2.7(5)
GX 1+4 (low state)	9	2315	0.08	0.07	–	$2.24^{+0.06}_{-0.12}$	–	–	0.93(126)
GX 1+4 (intermediate state)	3.5	385	0.11	0.14	–	$1.54^{+0.35}_{-0.22}$	$24.8^{+5.8}_{-3.0}$	$47.0^{+15.2}_{-10.7}$	1.16(125)
GX 1+4 (high state)	5	164	0.76	1.62	–	$0.93^{+0.12}_{-0.14}$	$25.1^{+1.1}_{-1.7}$	30.4 ± 2.4	1.19(136)
IGR/SAX J18027–2017[b]	–	1274	–	0.06	–	0.1[a]	–	$\sim$10	–
XTE J1807–294	–	711	–	0.11	–	1.96[a]	$48.1^{+7.6}_{-9.9}$	$75.7^{+58.1}_{-24.5}$	0.92(7)
AX J1820.5–1434	–	2322.3	–	0.1	–	0.9[a]	25 ± 3	17.0 ± 2.7	0.37(9)
AX J1841.0–0.535	–	77.19	–	0.11	–	2.2 ± 0.3	–	–	0.42(9)
GS 1843+009	–	62	–	0.17	–	0.34[a]	5.95[a]	17.4 ± 1.4	1.2(8)
A 1845–024	–	691.8	–	0.06	–	2.62 ± 0.19	–	–	0.46(7)
XTE J1855–026	9	652	0.16	0.17	–	1.69 ± 0.23	$23.99^{+2.88}_{-6.73}$	$38.49^{+10.35}_{-7.38}$	1.08(112)
XTE J1858+034	137	360	1.13	0.99	14.3 ± 0.7	1.38 ± 0.02	25.16 ± 0.33	7.92 ± 0.22	0.95(144)
X 1901+031	150	330	6.1	1.8	–	2.035 ± 0.015	11.27 ± 0.19	13.22 ± 0.11	0.82(127)
4U 1907+097	180	478.3	0.6	0.18	–	1.26 ± 0.07	7.0 ± 0.3	$9.0^{+0.3}_{-0.6}$	0.75(131)
KS 1947+300	2	6	1.09	1.17	–	$1.07^{+0.24}_{-0.13}$	$8.6^{+3.4}_{-1.2}$	$23.6^{+5.3}_{-2.3}$	1.18(104)
EXO 2030+375	2	25.3	0.84	0.85	–	1.71 ± 0.09	$25.2^{+2.5}_{-3.7}$	33^{+6}_{-4}	1.06(137)
SAX J2103.5+4545	33	196.6	0.38	0.38	0.9[a]	1.04 ± 0.15	8.5 ± 2.4	21.37 ± 2.75	1.21(120)

[a] The parameter is fixed.
[b] The cutoffpl model was used to fit the spectrum.
[c] In the energy range 20–60 keV.
[d] Lutovinov *et al.* (2005c) fitted the pulsar's spectrum over a wide energy range together with data from other observatories (see the text).

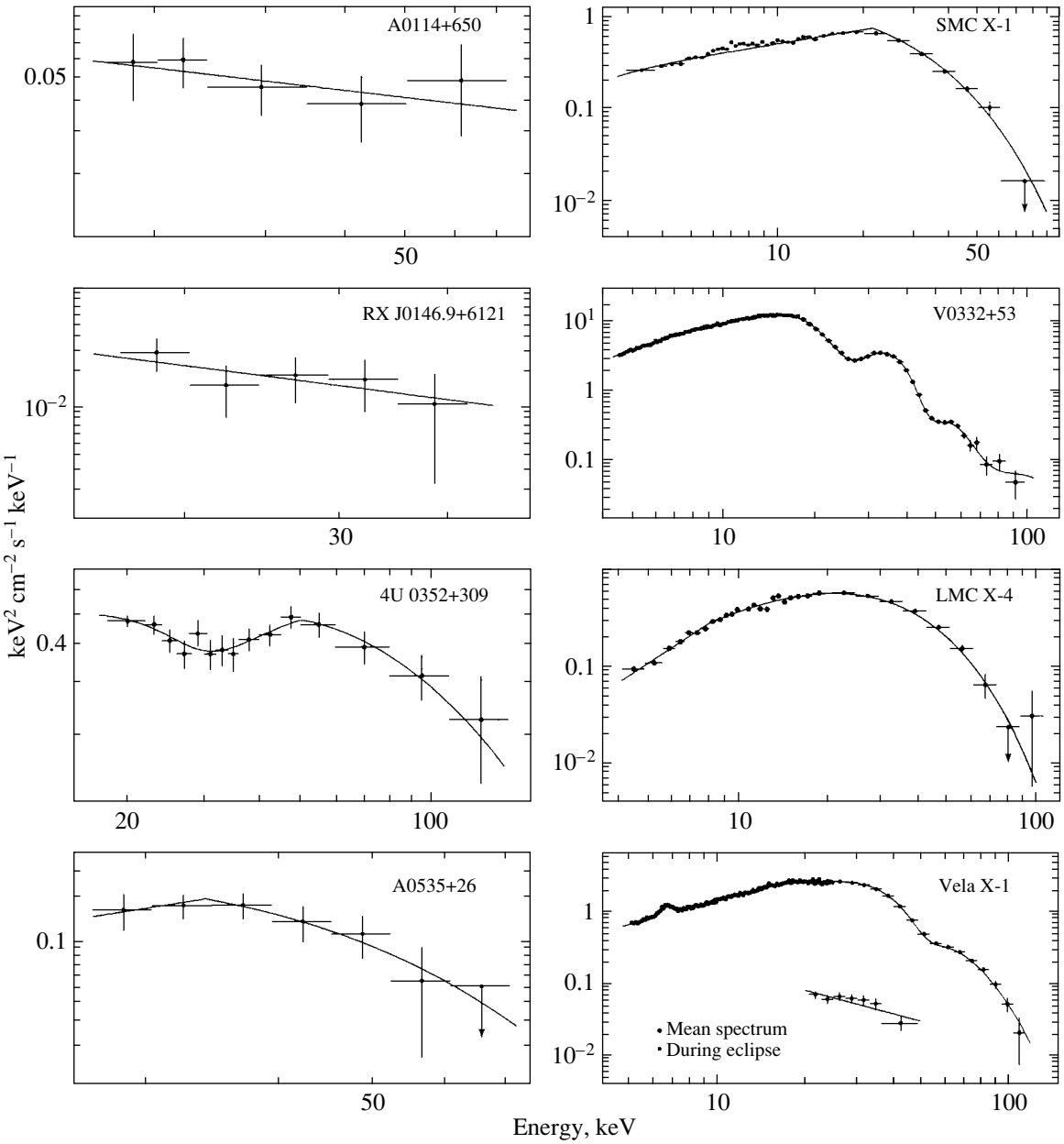

Fig. 2. INTEGRAL energy spectra for the X-ray pulsars. The solid lines represent the best fit to the spectrum. The errors correspond to one standard deviation.

the error limits. More detailed temporal and spectral analyses will be performed in a special paper.

4U 0352+309 (X Per). The pulsar was within the field of view of the IBIS X-ray telescope during the calibration observations of the Crab Nebula performed on August 14, 2003 (MJD 52 865). The mean 20–100 keV flux from the source was ~40 mCrab. We used model (1) with the inclusion of a resonance cyclotron absorption line to fit the pulsar's radiation spectrum. The source's spectrum (Fig. 2) and the best-fit parameters (Tables 2 and 3) were taken from Lutovinov *et al.* (2004b).

LMC X-4 (4U 0532–664). The X-ray pulsar LMC X-4 was observed by the INTEGRAL observatory in January 2003 as part of the "General Program." The total exposure was more than a million seconds for both instruments of the observatory (IBIS and JEM-X). These observations covered almost the entire superorbital period (~30.5 days) related to accretion disk precession.

Irrespective of the state in which the object under study was, its radiation spectrum was constant, within the error limits, although all of the main parameters are slightly lower than those obtained by other

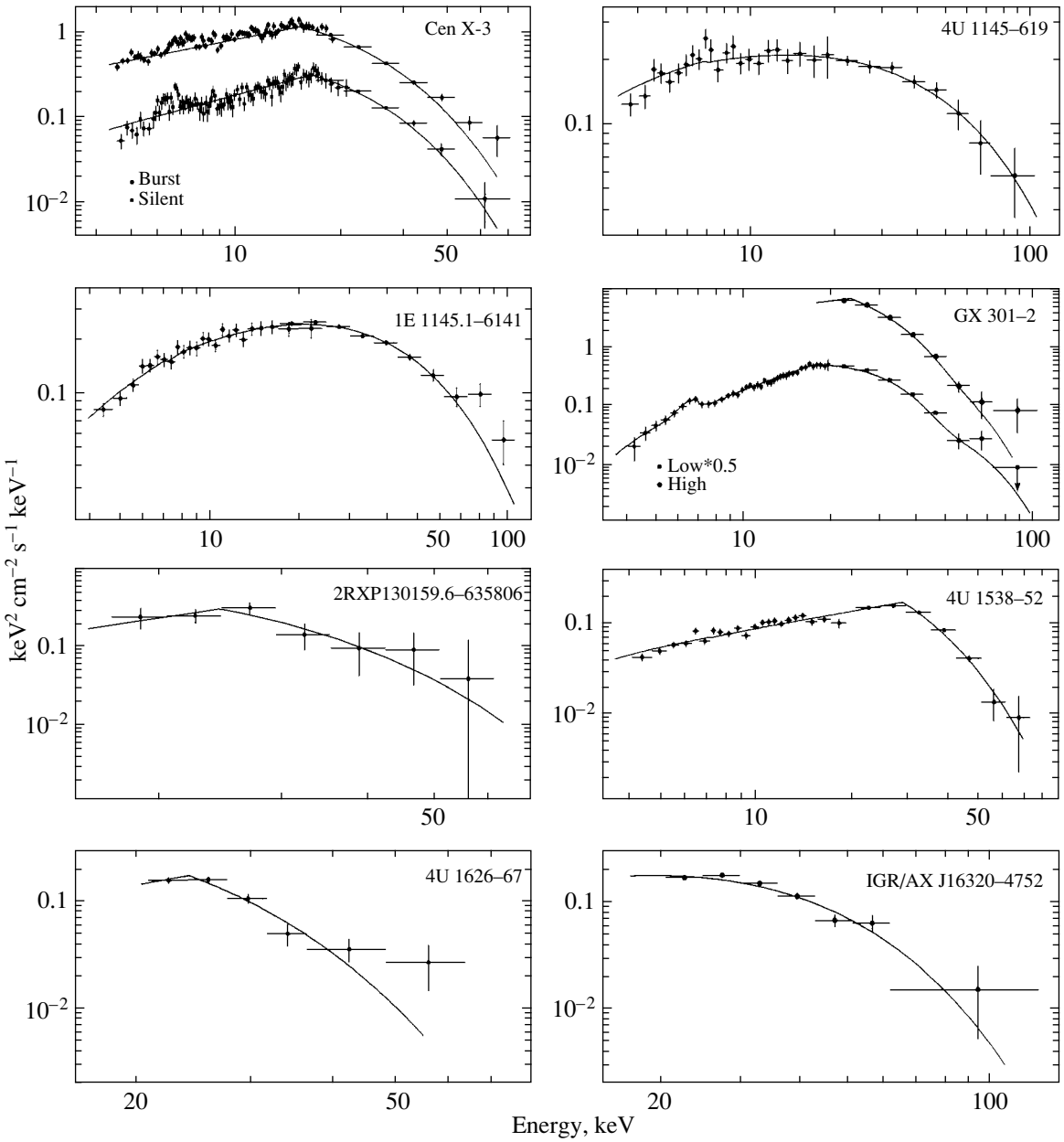

Fig. 2. (Contd.)

authors (see, e.g., La Barbera *et al.* 2001). Based on INTEGRAL data, Tsygankov and Lutovinov (2005a) studied the spectral properties of the pulsar LMC X-4 in more detail.

A0535+260. The pulsar A0535+260 is a transient source. On October 26, 2003 (MJD 52 938), the INTEGRAL observatory detected an increase in its 18–60 keV flux to ~10 mCrab compared to the upper limit of ~2 mCrab during previous observations. On October 28, 2003, (MJD 52 940), the flux reached ~40 mCrab in the same energy range. The subsequent observations of the source were interrupted due to solar flaring activity. Because of the short IBIS exposure for the pulsar, we constructed an average spectrum from all observations for this period during the outburst. The JEM-X monitor did not detect the source.

It follows from previous studies that the pulsar's spectrum is one of the hardest and may extend to ~200 keV (Maisack *et al.* 1997). The INTEGRAL observatory detected the source at a statistically significant level up to 50 keV, which can be explained by its short exposure. The spectrum obtained was fitted by a power law with an index of 2.81 ± 0.38, with the reduced $\chi^2 = 0.6(5)$. Kendziorra *et al.* (1994) fitted the source's spectrum in the energy range 3–200 keV

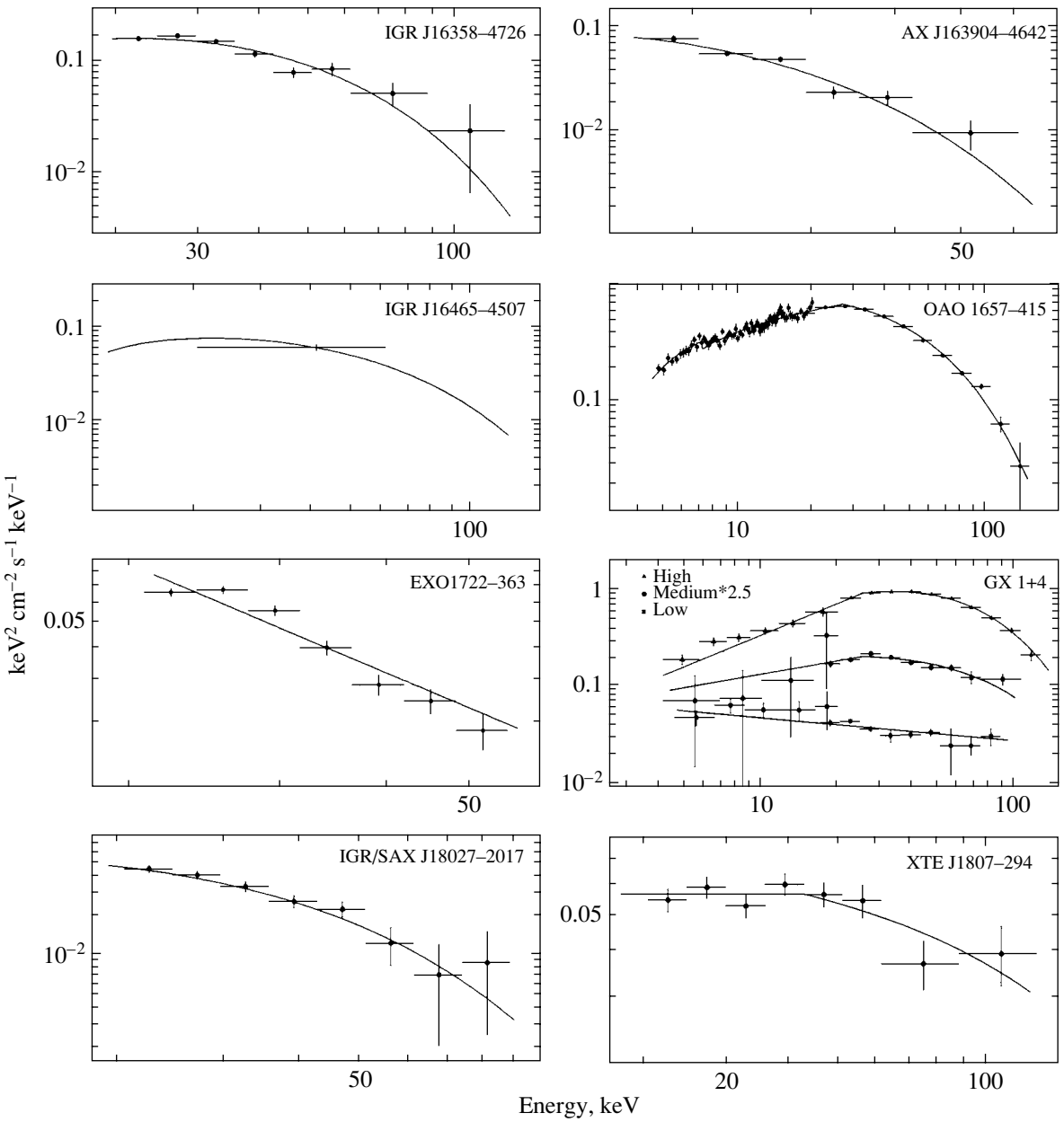

Fig. 2. (Contd.)

by model (1) with the following parameters: $\Gamma \sim 1.2$, $E_{\rm cut} \sim 24$ keV, and $E_{\rm fold} \sim 20$ keV. We also fitted the spectrum by model (1) by fixing the photon index and the cutoff energy; the derived e-folding energy was found to be a factor of 1.5 lower than the value given in the above paper. For this model, the reduced $\chi^2 = 0.07(5)$.

Vela X-1 (4U 0900–403). The pulsar Vela X-1 was regularly within the field of view of the instruments during the Galactic plane survey and during the observations of the region near the source as part of the "General Program." Preliminary results of the source's study using INTEGRAL data were presented by Kretschmar *et al.* (2004). The observations from January through July 2003 (MJD 52 644–52 832) were used in this paper. The flux from the pulsar is highly variable and subjected to orbital modulations. A flux of ~7 mCrab was detected from the pulsar at a statistically significant level during X-ray eclipse (much as was observed by the GRANAT observatory; see Lutovinov *et al.* 2000), and it reached 700 mCrab in the energy range 18–60 keV at the maximum. We constructed the pulsar's spectra for the eclipse phase and for various fluxes. Since the source was not detected by the JEM-X instrument during eclipses, we were able to construct its spec-

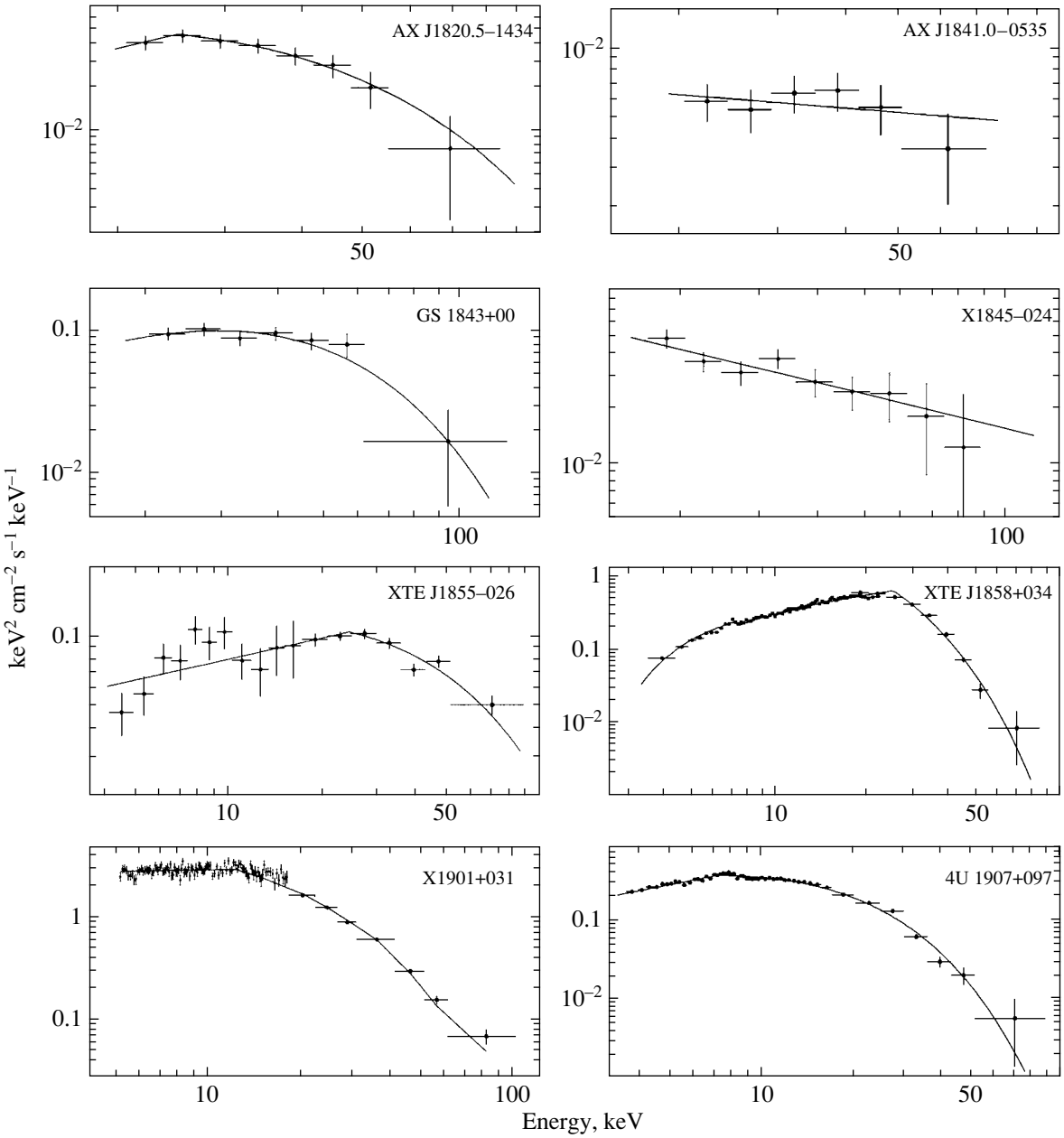

Fig. 2. (Contd.)

trum at these times only in the hard X-ray energy range. We fitted it by a simple power law with an index of 3.1 ± 0.3.

Since our analysis of the spectra outside eclipse revealed no marked differences in their shape, we give the pulsar's average spectrum. A cyclotron line at ~24 keV and its harmonic at ~50 keV were detected in the source (Table 3), in agreement with previous results (see, e.g., Coburn *et al.* 2002). A prominent feature that can be described by a model iron emission line is also observed near an energy of 6–7 keV. However, given the peculiarities of the JEM-X response matrix (see above), we treat this interpretation with great caution.

Cen X-3 (3U 1118–60). We used the pointings from January through July 2003 (MJD 52 668–52 832) obtained both during the Galactic plane scanning and as part of the "General Program" to analyze the pulsar's spectrum. Using the known orbital parameters of the binary (Burderi *et al.* 2000), we determined the orbital phases for our observations and analyzed the emission from the source during and outside X-ray eclipse. The source was not detected during eclipse; the upper 1σ limit on its 18–60 keV flux was 2.5 mCrab. Outside eclipse, the mean

flux from the pulsar was ~17 mCrab in the same energy range. Several outbursts during which the flux reached ~90 mCrab were detected against this background.

We constructed the pulsar's radiation spectrum averaged over all outbursts and an average persistent spectrum for the source outside eclipse. Our study showed that the spectrum becomes softer during outbursts: the photon index increases from 0.87 to 1.16 (both spectra are shown in Fig. 2). In fitting the spectra, we attempted to introduce a component that describes the iron emission line in the model. Since we failed to do this properly due to the difficulties in reconstructing the spectra from JEM-X data mentioned above, we described the source's spectrum in the standard X-ray energy range by a simple power law. Otherwise, our best-fit parameters for the spectrum (Table 2) are in good agreement with the values obtained by Burderi *et al.* (2000) and La Barbera *et al.* (2004).

4U 1145–619, 1E 1145.1–614. When analyzing the emission from 4U 1145–619, White *et al.* (1978) found pulsations from this pulsar at two close frequencies. This puzzle was solved using data from the Einstein observatory, whose instruments detected the second source, 1E 1145.1–614, at less than 20′ from the first source (Lamb *et al.* 1980).

The pulsar 4U 1145–619 is a transient from which regular outbursts with a duration of ~10 days at intervals of ~186.5 days are observed; this is assumed to be the orbital period in the binary. At the end of May 2003 (MJD 52 788), the INTEGRAL observatory detected an outburst from it during which the mean 18–60 keV flux was ~26 mCrab. We used the available data in this time interval to construct the pulsar's average spectrum. In the remaining time, the upper (1σ) limit on the flux from the pulsar was 4 mCrab in the same energy range.

The study of 1E 1145.1–614 is severely complicated by the proximity of its twin, which becomes much brighter during outbursts, and the standard collimator X-ray instruments do not allow these sources to be observed separately. The pulsar could be studied in more detail after its discovery only several years later using ART-P (Grebenev *et al.* 1992) and RXTE data, when its twin was in quiescence (Ray and Chakrabarty 2002). In our paper, we used the observations from March 2003 through September 2004 (MJD 52 710–53 276) to analyze 1E 1145.1–614. In this period, its flux was constant and had a mean value of ~20 mCrab, except the following times: 52 795 MJD, when the flux from the pulsar increased to ~100 mCrab; 53 196 MJD, when the source flared up again (Bodaghee *et al.* 2004); and the outburst time of the pulsar 4U 1145–619,

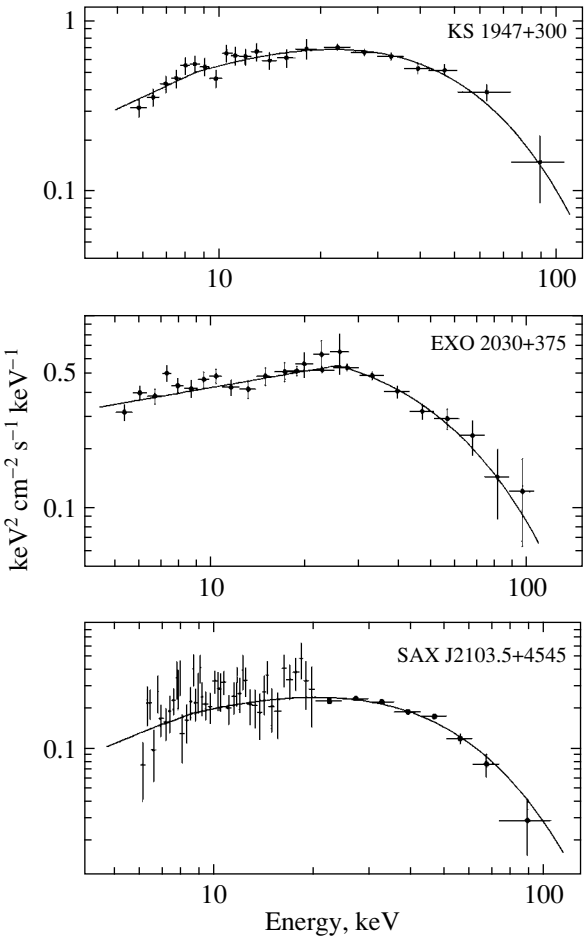

Fig. 2. (Contd.)

when the mean flux from 1E 1145.1–614 rose to 40 mCrab. However, we found no clear correlations of the flux rises between the two sources; therefore, we concluded that these events were independent. We constructed the source's spectra during and outside these outbursts. The source was not within the JEM-X field of view during the outbursts and was not detected by the instrument outside these, except the outburst period of 4U 1145–619. Since no clear differences were found in the spectral shape of 1E 1145.1–614, we give here only an average spectrum for all observations. The derived best-fit parameters for the average spectrum of 1E 1145.1–614 are in good agreement with the values from Ray and Chakrabarty (2002), who analyzed the source's spectrum using RXTE data, except the photon index, which proved to be slightly smaller. The parameter $N_{\rm H}$ was fixed at the value given in the paper mentioned above.

During the outbursts in 1984 and 1985, the mean photon index for the pulsar 4U 1145–619 was equal to one, the low-energy absorption changed from 26×10^{22} to 3.1×10^{22} cm^{-2}, the cutoff energy

Table 3. Other best-fit parameters for the spectra of the pulsars

Binary	Fe line center, keV	Fe line width, keV	Fe line intensity, photons cm^{-2} s^{-1}	E_{cycl}, keV	τ_{cycl}	σ_{cycl}, keV
V0332+53[a]	–	–	–	$24.25^{+0.07}_{-0.14}$	$1.98^{+0.02}_{-0.04}$	7.10±0.10
4U 0352+309	–	–	–	28.8 ± 2.5	0.33 ± 0.12	9[b]
Vela X-1[c]	6.64 ± 0.10	0.31 ± 0.16	$(4.7 \pm 0.8) \times 10^{-3}$	24.0 ± 0.3	0.38 ± 0.01	5.3 ± 0.5
GX 301−2 (high)	–	–	–	$49.2^{+4.2}_{-2.1}$	$0.60^{+0.13}_{-0.09}$	18[b]
GX 301−2 (low)	$6.54^{+0.17}_{-0.11}$	$0.52^{+0.22}_{-0.14}$	$(2.54 \pm 1.02) \times 10^{-3}$	$47.4^{+2.2}_{-1.1}$	0.87±0.17	18[b]

[a] Two more features were found in the pulsar spectrum, the second and third harmonics of the cyclotron line: $E_{cycl2} = 46.8^{+0.2}_{-0.1}$, $\tau_{cycl2} = 1.94^{+0.06}_{-0.07}$, $\sigma_{cycl2} = 8.9 \pm 0.4$; $E_{cycl3} = 67.9^{+3.2}_{-4.3}$, $\tau_{cycl3} = 2.60^{+0.25}_{-0.35}$, $\sigma_{cycl3} = 26.9 \pm 5.4$.
[b] The parameter is fixed.
[c] The second harmonic of the cyclotron line with $E_{cycl2} = 50.2 \pm 0.5$ keV, $\tau_{cycl2} = 0.95 \pm 0.03$, $\sigma_{cycl2} = 12.2 \pm 0.5$ keV was detected in the pulsar.

remained constant ∼6 keV, and the e-folding energy rose from ∼12 keV during the 1984 outburst to ∼17 keV during the 1985 outburst (Cook and Warwick 1987). Our analysis showed that the pulsar's spectrum became softer, $\Gamma = 1.5 \pm 0.1$, while the e-folding energy increased to 30 ± 4 keV. The sensitivity of the JEM-X detector is too low to determine the low-energy absorption, while its spread does not allow it to be fixed at a particular value; therefore, we did not introduce this component in the standard model when fitting the spectrum.

GX 301−2 (3A 1223−624). To analyze the source, we used the publicly accessible INTEGRAL observational data obtained from January through July 2003. Over this period, the IBIS telescope made about 250 pointings at the object under study, which included two times close to the periastron passage by the neutron star. Therefore, all of the data obtained were arbitrarily divided into low and high (periastron passage) states. For the high state, we had some 10 IBIS pointings at our disposal (we took into consideration the pointings for which the orbital phase was within the range from 0.87 to 0.92), while for the low state we were able to reconstruct the broadband spectrum using also 23 JEM-X pointings. A preliminary analysis based on the first several IBIS pointings was performed by Kreykenbohm *et al.* (2004).

Tsygankov *et al.* (2004) showed that the shape of the source's radiation spectrum and its hardness were subjected to random variations on a time scale of the order of several thousand seconds. In this paper, we failed to analyze these variations due to the lack of JEM-X data in the high state and insufficient statistics in the low state. In our spectral analysis of the low state for the pulsar GX 301−2, we corrected significantly model fit (1): low-energy absorption (many authors pointed out a significant hydrogen column density that strongly depends on the object's orbital phase and that reaches $\sim 2 \times 10^{24}$ atoms cm^{-2}; Endo *et al.* 2002), an iron line, and a resonance cyclotron absorption line were added to the power law with a high-energy cutoff. The latter feature whose existence was mentioned by various authors (see, e.g., Orlandini *et al.* 2000; Coburn *et al.* 2002) has a confidence level higher than 3σ and improves significantly the quality of the fit. In our case, for the low state (the mean 3−100 keV flux from the source was 1.9×10^{-9} erg cm^{-2} s^{-1}), we obtained the energy $E_{cyc} = 47.4 \pm 1.9$ keV for the cyclotron absorption line that is closest to the value given by Orlandini *et al.* (2000) (the line width was fixed at the value taken from this paper). Within the error limits, our results are also in good agreement with the results of other authors.

As was mentioned above, we had only the IBIS data at our disposal for the high state. Nevertheless, the quality of the spectrum allowed us to detect a statistically significant change in the photon index, which slightly increased compared to the low state (Table 2), but was slightly lower than that in Borkus *et al.* (1998), while the remaining model parameters were in good agreement. When this parameter is fixed at 0.3 obtained in the low state, the quality of the fit deteriorates sharply. In this case, we also added the resonance cyclotron absorption line at energy ∼49 keV whose confidence level was about 2σ (Table 3) to the standard model (1).

2RXP 130159.6−635806. Hard X-ray emission from the region of the sky containing this object was detected by the INTEGRAL observatory during its outburst in late January−early February 2004 (Chernyakova *et al.* 2004), when the 20−60 keV flux from the source reached ∼15 mCrab. Subsequently, XMM-Newton data revealed X-ray pulsations from it with a period of ∼700 s. The spectral and temporal

properties of the new pulsar were analyzed in detail by Chernyakova *et al.* (2005) using both current XMM-Newton and INTEGRAL data and archival ASCA and BeppoSAX data. The source's spectrum and its best-fit parameters over a wide energy range (1–70 keV) presented in Fig. 2 and Table 2, respectively, were taken from the same paper.

4U 1538–522. The pulsar 4U 1538–522 is a persistent source. Over the period of our observations from February 2003 through September 2004 (MJD 52 671–53 260), its mean 18–60 keV flux was ~15 mCrab. We constructed the pulsar's average spectrum from all of the available data in the energy range 4–80 keV. The derived best-fit parameters for the spectrum are in good agreement with the values from Robba *et al.* (2001) ($N_{\rm H}$ was taken from the same paper), who analyzed the pulsar's spectrum using BeppoSAX data.

4U 1626–67. To study the pulsar 4U 1626–67, we used the observations from March through October 2003 (MJD 52 699–52 915) performed as part of the Galactic plane scanning and the deep Galactic center survey. The light curve of the source exhibited no statistically significant variations in the flux, whose mean value was ~12 mCrab in the energy range 18–60 keV; therefore, we constructed an average spectrum of the pulsar. Since the source was far from the Galactic plane ($b = -13.1$), it was not within the JEM-X field of view, which did not allow us to reconstruct its spectrum in the soft X-ray energy range. Preliminary results of the pulsar's analysis based on INTEGRAL data were presented by Denis *et al.* (2004), who described the source's spectrum by a simple power law with an index of 3.4. In our paper, the exposure of the available observations is a factor of 10 longer; therefore, we were able to fit the spectrum by the standard model (1) by fixing the photon index at the value given in Orlandini *et al.* (1998), who analyzed the pulsar's spectrum over a wide energy range (0.1–100 keV). Our values of $E_{\rm cut}$ and $E_{\rm fold}$ are in good agreement with those given in the same paper.

IGR/AX J16320–4752, IGR J16358–4726, AX J163904–4642, IGR J16465–4507. These recently discovered long-period pulsars (with pulsation periods of several hundred seconds) belong to the class of strongly absorbed sources discovered by the INTEGRAL observatory. These are not detected by the JEM-X monitor because of significant absorption. Therefore, Lutovinov *et al.* (2005c) analyzed their spectra over a wide energy range using data from the RXTE, ASCA, and XMM-Newton observatories in the standard X-ray energy range and from the ISGRI detector at energies above 18 keV; We used model (2) to fit the spectra. The spectra of the sources (Fig. 2) and their best-fit parameters (Table 2) were taken from Lutovinov *et al.* (2005c).

OAO 1657–415. The intensity of the pulsar OAO 1657–415 is subjected to strong orbital modulations and varies between a few mCrab (during X-ray eclipse) and 100–150 mCrab in the energy range 18–60 keV. Since our study of the source's spectrum at various orbital phases (the orbital parameters of the binary were taken from Baykal (2000)) revealed no marked differences in its shape, we constructed an average spectrum from all of the available data from March 2003 until April 2004 (MJD 52 699–53 097). The pulsar's spectrum is one of the hardest spectra for X-ray pulsars in binaries, extending to 100 keV (see Table 2 and Fig. 2), and strong absorption with $N_{\rm H} \sim 10^{23}$ cm^{-2} is observed at low energies. The pulsar will be analyzed in detail using INTEGRAL and RXTE data in a special paper.

EXO 1722–363. The flux from the pulsar EXO 1722–363 is subjected to orbital modulations (Markwardt and Swank 2003; Lutovinov *et al.* 2004b) and changed from a few to 50 mCrab in the energy range 18–60 keV over the period of our observations from March 2003 through April 2004 (MJD 52 698–53 097). Based on INTEGRAL data, Lutovinov *et al.* (2004b, 2004c) improved the localization accuracy of the object and showed that the shape of the hard part of the pulsar's spectrum remains constant, although the flux is highly variable, while the shape of its soft part analyzed using RXTE data strongly depends on the orbital phase of the binary, and the photoabsorption can reach $N_{\rm H} \simeq 10^{24}$ cm^{-2}.

We failed to reconstruct the source's spectrum from JEM-X data, since it was within the field of view of this instrument only during states with low fluxes. Our analysis showed that the pulsar is detected at a statistically significant level up to ~60 keV, and its hard X-ray spectrum can be described either by a power law with an index of 3.5 or by model (2), from which it follows that the e-folding energy is ~15 keV. However, both models describe the source's spectrum poorly, and further studies over a wide energy range are required to improve its parameters.

GX 1+4 (4U 1728–247). To analyze the radiation spectrum of the X-ray pulsar GX 1+4, we used the currently publicly accessible data that cover the interval from late February through late September 2003. The total exposure for the IBIS telescope was ~2400 ks; the source was within the JEM-X field of view much more rarely.

Our analysis showed that the spectral parameters of the pulsar's radiation depend on its flux. When constructing average spectra for the object under

study, we took into account the pulsar's intensity in the time interval where the averaging was performed. Therefore, we identified three segments (MJD 52 698–52 700, MJD 52 710–52 753, and MJD 52 874–52 910) in the light curve with mean 18–60 keV fluxes from the source of ∼130, ∼11, and ∼6 mCrab, respectively. In the latter case (low state), the source's spectrum was best fitted by a simple power law. Despite significant errors, we see from Table 2 that as the intensity of the radiation from the object under study decreases, its spectrum becomes slightly softer, as confirmed by the studies of other authors (Paul *et al.* 1995).

IGR/SAX J1802.7–2017. The INTEGRAL spectrum of the new X-ray pulsar IGR/SAX J1802.7–2017 was analyzed by Lutovinov *et al.* (2005a), from which we took its best-fit parameters.

XTE J1807–294. Formally, this source is not an accretion-powered X-ray pulsar and belongs to the class of millisecond pulsars. Campana *et al.* (2003) showed that the source's XMM-Newton radiation spectrum at low energies is best fitted by the combination of an absorbed blackbody and Comptonization models or a power law without absorption or emission lines.

Because of its transient nature, the pulsar under study was detected by the IBIS telescope at a statistically significant level only in the period between February 20 and May 1, 2003 (MJD 52 690–52 760) (Falanda *et al.* 2005), without being detected by the JEM-X monitor. It should be noted that this source is the only millisecond pulsar in our sample, which is why we pay special attention to choosing the model fit. To analyze the spectral properties of the pulsar's radiation, we used models (1) and (2) and a simple power law; for the composite models, the power-law index was fixed at the value taken from Campana *et al.* (2003). Based on $\Delta\chi^2$ statistics, we established that model (1) with the parameters from Table 2 is in best agreement with the experimental data. Such high values of $E_{\rm cut} \sim 48$ keV and $E_{\rm fold} \sim 76$ keV are not a rarity for flaring millisecond pulsars (see, e.g., Heindl and Smith 1998).

AX J1820.5–1434. The pulsar AX J1820.5–1434 was discovered in 1997 during the Galactic plane scanning by the ASCA observatory (Kinugasa *et al.* 1998); these authors also analyzed the source's spectrum in the soft X-ray energy range. The INTEGRAL observatory first detected the source in the hard X-ray energy range (Lutovinov *et al.* 2003b). The available observations can be arbitrarily divided into two groups: from March through April 2003 (MJD 52 699–52 759), during which the flux from the source did not change appreciably and was ∼8 mCrab in the energy range 18–60 keV, and from September through October 2003 (MJD 52 909–52 929), when the source was not detected at a statistically significant level and the upper 1σ limit on its flux was 0.3 mCrab in the same energy range. We constructed an average spectrum from all of the data when the source was not detected and used model (1) to fit it; the photon index was fixed at 0.9 given in Kinugasa *et al.* (1998). We see from Fig. 2 that the pulsar was detected at a statistically significant level up to ∼70 keV.

AX J1841.0–0535. The pulsar AX J1841.0–0535, which was discovered by the ASCA observatory (Bamba *et al.* 2001), was detected during the observations of the region of the Sagittarius Arm by the INTEGRAL observatory in the spring of 2003. Since its position in a preliminary analysis slightly differed from that measured by the ASCA observatory, it was called a new source, IGR J18406–0539 (Molkov *et al.* 2004a). In October 2004, another outburst was detected from the same region of the sky. As previously, it was initially attributed to the new source IGR J18410–0535 (Rodriguez *et al.* 2004), but it was subsequently shown that the same source as that in 2003 was observed (Halpern *et al.* 2004).

A more detailed analysis has shown that the source was detected at a statistically significant level in the spring of 2003 only in two observations during which its 18–60 keV flux reached ∼ 40 mCrab. An increase in the flux from the source to ∼ 10 mCrab in the same energy range was also detected in October 2003. In the remaining time, the upper 1σ limit on the (18–60 keV) flux from the pulsar was 1 mCrab. We have obtained a hard X-ray spectrum of the source averaged over the entire period of its high state for the first time. Because of the poor statistics, we fitted the spectrum by a simple power law with an index of 2.2 ± 0.3.

GS 1843+009. An average spectrum for the transient pulsar GS 1843+009 in the hard X-ray energy range (20–100 кэВ) was constructed from the data obtained in early May 2003 (MJD 52 759–52 760), when an outburst was detected from the source (Cherepashchuk *et al.* 2003) and its 18–60 keV flux during the outburst was ∼7 mCrab. The JEM-X monitor did not detect the pulsar.

Because of the lack of data in the softer part of the spectrum, when describing it by model (1), we fixed the following parameters obtained from BeppoSAX data over a wide energy range during the outburst from the source in April 1997: $\Gamma = 0.34$ and $E_{\rm cut} = 5.95$ keV (Piraino *et al.* 2000). The derived e-folding energy $E_{\rm fold} = 17.4 \pm 1.4$ keV is in good agreement with the value given in Piraino *et al.* (2000). This may suggest that the shape of the source's radiation spectrum is constant irrespective of its luminosity.

A1845–024. Soffitta *et al.* (1998) identified the pulsar A1845–024 with the sources GS 1843–02 and GRO J1849–03. To analyze its spectrum, we used the publicly accessible observations from March through October 2003 (MJD 52 699–52 930). Over this period, one outburst was detected from the pulsar during which the 18–60 keV flux reached ~7 mCrab; the outburst began approximately on MJD 52 728 and lasted for ~40 days. We constructed the pulsar's average spectrum for this period from ISGRI data; the JEM-X instrument did not detect the source. In the remaining time, the upper 1σ limit on the flux from the source was 0.4 mCrab in the same energy range. The pulsar's 18–90 keV spectrum was fitted by a simple power law with a photon index of $\Gamma = 2.62 \pm 0.19$, in agreement with that obtained by Zhang *et al.* (1996), whose used ComptonGRO data.

XTE J1855–026. For the pulsar XTE J1855–026, we were able to construct a broadband spectrum in the energy range 4–100 keV using the 9-ks-averaged JEM-X data obtained on October 18, 2003, and the IBIS data averaged over all of the available observations (March 2003–April 2004).

We used model (1) to fit the INTEGRAL data; because of the low flux from the source (2.68×10^{-10} erg cm^{-2} s^{-1} in the energy range 3–100 keV), the quality of the soft (<20 keV) X-ray spectrum did not allow us to detect an iron line and low-energy absorption. It should be noted that there is a discrepancy between our best-fit parameters and those given in Corbet *et al.* (1999): according to the INTEGRAL data, the spectrum is slightly softer, while the *e*-folding energies at high energies are larger by about 10 keV.

XTE J1858+034 (inserted into the proof). The pulsar XTE J1858+034 is a transient source that was discovered during its outburst in 1998 by the RXTE observatory (Remillard *et al.* 1998). During the observations of the Sagittarius Arm by the INTEGRAL observatory (MJD 53 116–53 128), a new outburst was detected from the source, during which its localization accuracy was improved (Molkov *et al.* 2004b). In the period MJD 53 116–53 119, the mean 18–60 keV flux from the source was ~ 6 mCrab; subsequently, it rose and reached ~ 83 mCrab in the same energy range by MJD 53 128. Since there were no INTEGRAL data, the subsequent behavior of the source was analyzed using the light curve constructed from ASM/RXTE data in the energy range 1–12 keV, which are accessible at http://xte.mid.edu. It follows from this light curve that the flux from the pulsar no longer increased, but remained at this level for ~4 more days, following which it began to decrease.

To find the possible dependence of the pulsar's spectral shape on its intensity, we constructed the source's mean spectra for the above time intervals. Our analysis showed that the spectral shape of the pulsar is virtually independent of the outburst phase; therefore, we give the mean spectrum for the entire period of observations. We used model (1) modified by low-energy absorption to fit it and obtained the following parameters: $N_{\rm H} = (14.3 \pm 0.7) \times 10^{22}$ cm^{-2}, $\Gamma = 1.38 \pm 0.02$, $E_{\rm cut} = 25.16 \pm 0.33$ keV, and $E_{fold} = 7.92 \pm 0.22$ keV. Paul and Rao (1998) analyzed the pulsar's spectrum in the energy range 2–50 keV using RXTE data, but they failed to obtain reasonably bounded best-fit parameters for the spectrum. Thus, our measurements are the first reliable determination of the parameters for the source's spectrum in a wide energy range. The behavior of the source during its 2004 outburst will be analyzed in more detail in a special paper.

X1901+03. The X-ray pulsar X1901+03 was observed by the INTEGRAL observatory during its outburst in the spring of 2003 (Galloway *et al.* 2003). The spectrum and its best-fit parameters based on model (1) were taken from Molkov *et al.* (2003), who performed spectral and temporal analyses of the pulsar's behavior.

4U 1907+097. To construct the spectrum for the pulsar 4U 1907+097, we used the publicly accessible observational data from March through May 2003 (MJD 52 705–52 762). The mean 18–60 keV flux from the source in this period was ~20 mCrab; however, we observed episodes with a duration of ~1 day when the flux dropped by a factor of 2 and detected one outburst during which the flux doubled compared to its mean value.

Roberts *et al.* (2001) analyzed the source's soft X-ray spectrum in detail using ASCA data, which were fitted by a simple power law with low-energy absorption, and RXTE data in the range 2.5–20 keV, which were fitted by model (2). This analysis showed that the best-fit parameters for the pulsar's spectrum change only slightly with flux, except the absorption, which changes from $\sim 2 \times 10^{22}$ to $\sim 8 \times 10^{22}$ cm^{-2} throughout the orbital cycle.

We constructed the source's average spectrum from all of the available observations and fitted it by model (1). Our photon index agrees with the values given in Roberts *et al.* (2001) and Cusumano *et al.* (1998) (in this paper, the source's spectrum was analyzed over a wide energy range using BeppoSAX data and was fitted by model (1)). At the same time, the *e*-folding energy proved to be a factor of 1.7 lower than the values given in these papers.

Cusumano *et al.* (1998) detected a cyclotron line at 19 keV and its harmonic in the pulsar's spectrum. Our analysis did not reveal these features in the source's spectrum.

KS 1947+300. The transient X-ray pulsar KS 1947+300 was within the IBIS/INTEGRAL field of view from December 2002 until April 2004 ~700 times, with the total exposure being ~1.5 million s. Because of its flaring activity, several states differing in intensity for which independent spectral analyses were performed using INTEGRAL and RXTE data (Tsygankov and Lutovinov 2005b) can be identified in the source's light curve.

Here, we provide the INTEGRAL spectrum of the source obtained on April 7, 2004, when it was detected at a statistically significant level by both the IBIS telescope and the JEM-X monitor. The pulsar's spectrum (Fig. 2) and its best-fit parameters (Table 2) were taken from Tsygankov and Lutovinov (2005b).

EXO 2030+375. The INTEGRAL observations of the transient pulsar EXO 2030+375 prior to MJD 52 650 were analyzed in several papers (see, e.g., Kuznetsov *et al.* 2004; Camero Arranz *et al.* 2004; and references therein). Over the period from MJD 52 650 to MJD 52 838, three outbursts (MJD 52 717, MJD 52 761, MJD 52 805) were detected from the source, during which the 18–60 keV flux reached ~80 mCrab. In the remaining time, the upper 1σ limit on its flux was 2 mCrab in the same energy range. Because of the scarcity of data, we failed to analyze the spectra for each outburst separately; therefore, we constructed an average spectrum for all outbursts. Our best-fit parameters based on model (1) agree with those given in Kuznetsov *et al.* (2004) and Reynolds *et al.* (1993a) for the hard and soft X-ray energy ranges, respectively.

SAX J2103.5+4545. The source SAX J2103.5+4545 was within the field of view of the INTEGRAL instruments during the calibration observations of the Cyg X-1 region in December 2002 (MJD 52 629–52 632 and MJD 52 636–52 637); a detailed analysis of these observations can be found in our previous paper (Filippova *et al.* 2004). The data obtained later during the Galactic plane scanning were analyzed by Sidoli *et al.* (2004). The pulsar's spectrum shown in Fig. 2 and its best-fit parameters (Table 2) were taken from Filippova *et al.* (2004).

CONCLUSIONS

We have presented a catalog of spectra for 34 accretion-powered X-ray pulsars and one millisecond pulsar that were observed by the INTEGRAL observatory and that were detected by its instruments at a statistically significant level in the period from MJD 52 629 to MJD 53 276. For 18 of the 35 sources, we were able to reconstruct their broadband spectra. The sources under study include one millisecond pulsar, XTE J1807–294, and seven recently discovered X-ray pulsars: 2RXP J130159.6–635806, IGR/AX J16320–4751, IGR J16358–4726, AX J163904–4642, IGR J16465–4507, SAX/IGR J18027–2017, and AX J1841.0–0535. Hard X-ray spectra have been obtained for the pulsars RX J0146.9+6121, AX J1820.5–1434, and AX J1841.0–0535 for the first time.

For variable sources, we analyzed the flux dependence of the spectral shape. For example, the spectrum of the pulsar GX 1+4 becomes harder with increasing intensity of the source. We also compared our best-fit parameters with the results of previous studies and discussed their evolution.

A hard X-ray spectrum has been obtained for the pulsar Vela X-1 for the first time during an eclipse of the source by its optical companion. We were able to reconstruct it only in the hard X-ray energy range, since the JEM-X instrument did not detect the pulsar at this time. The spectrum was described by a simple power law with an index of 3.1.

Cyclotron lines and their harmonics were detected in the spectra of several pulsars: one harmonic in 4U 0352+309, one harmonic in both low and high states in GX 301–2, two harmonics in Vela X-1, and three harmonics in V 0332+53.

ACKNOWLEDGMENTS

We thank E.M. Churazov, who developed the algorithms for IBIS data analysis and provided the software. We also thank M.R. Gilfanov and P.E. Shtykovskiy for a discussion of the results obtained. This work was supported by the Russian Foundation for Basic Research (project no. 04-02-17276). We are grateful to the European INTEGRAL Science Data Center (Versoix, Switzerland) and the Russian INTEGRAL Science Data Center (Moscow, Russia) for the data. The work was performed in part during visits to the European INTEGRAL Science Data Center (Versoix, Switzerland); A.A. Lutovinov and S.S. Tsygankov thank its staff for hospitality and computer resources. A.A. Lutovinov thanks the ESA, and S.S. Tsygankov thanks the Russian Academy of Sciences (the "Nonstationary Phenomena in Astronomy" program) for support of these visits. We are also grateful to the INTEGRAL maintenance service and the software developers for the JEM-X instrument, namely, C.A. Oxborrow and P. Kretschmar, for help in interpreting the results obtained from the data of this instrument. The results of this work are based on observations of the INTEGRAL observatory, an ESA project with the participation of Denmark, France, Germany, Italy, Switzerland, Spain, the Czech Republic, Poland, Russia, and the United States.

REFERENCES

1. G. Augello, R. Iaria, N. Robba, *et al.*, Astrophys. J. **596**, 63 (2003).
2. A. Bamba, J. Yokogama, M. Ueno, *et al.*, Publ. Astron. Soc. Jpn. **53**, 1179 (2001).
3. A. Baykal, Mon. Not. R. Astron. Soc. **313**, 637 (2000).
4. A. Baykal, M. Stark, and J. Swank, Astrophys. J. Lett. **544**, L129 (2000).
5. L. Bildsten, D. Chakrabarty, J. Chiu, *et al.*, Astrophys. J., Suppl. Ser. **113**, 367 (1997).
6. A. Bodaghee, N. Mowlavi, and J. Ballet, Astron. Telegram **290**, 1 (2004).
7. E. Bonning and M. Falanga, Astron. Astrophys. **436**, 31L (2005).
8. V. V. Borkus, A. S. Kaniovsky, R. A. Sunyaev, *et al.*, Pis'ma Astron. Zh. **24**, 83 (1998) [Astron. Lett. **24**, 60 (1998)].
9. K. Borozdin, M. R. Gilfanov, R. A. Sunyaev, *et al.*, Pis'ma Astron. Zh. **16**, 804 (1990) [Sov. Astron. Lett. **16**, 345 (1990)].
10. L. Burderi, T. Di Salvo, N. Robba, *et al.*, Astrophys. J. **530**, 429 (2000).
11. A. Camero Arranz, P. Reig, P. Connell, *et al.*, in *Proceedings of the 5th INTEGRAL Workshop on "The INTEGRAL Univers"*, Ed. by V. Schönfelder *et al.* (ESA Publ. Division, Noordwijk, 2004), SP-552, p. 279.
12. S. Campana, M. Ravasio, G. L. Israel, *et al.*, Astrophys. J. Lett. **594**, L39 (2003).
13. D. Chakrabarty, J. Grunsfeld, A. Thomas, *et al.*, Astrophys. J. **403**, 33 (1993).
14. D. Chakrabarty, L. Homer, P. Charles, *et al.*, Astrophys. J. **562**, 985 (2001).
15. D. Chakrabarty, Z. Wang, A. Juett, *et al.*, Astrophys. J. **573**, 789 (2002).
16. A. Cherepashchuk, S. Molkov, L. Foschini, *et al.*, Astron. Telegram **159**, 1 (2003).
17. M. Chernyakova, P. Shtykovskiy, A. Lutovinov, *et al.*, Astron. Telegram **251**, 1 (2004).
18. M. Chernyakova, A. Lutovinov, J. Rodriguez, and M. Revnivtsev, MNRS (accepted), astro-ph/0508515 (2005).
19. G. Clark, Astrophys. J. **542**, 131 (2000).
20. W. Coburn, W. Heindl, R. Rothschild, *et al.*, Astrophys. J. **580**, 394 (2002).
21. W. Coburn, P. Kretschman, I. Kreykenbohm, *et al.*, Astron. Telegram **381**, 1 (2005).
22. M. Coe, B. Payne, A. Longmore, *et al.*, Mon. Not. R. Astron. Soc. **232**, 865 (1988).
23. M. Cook and R. Warwick, Mon. Not. R. Astron. Soc. **227**, 661 (1987).
24. R. Corbet, F. Marshall, A. Peele, *et al.*, Astrophys. J. **517**, 956 (1999).
25. R. Corbet and K. Mukai, Astrophys. J. **577**, 923 (2002).
26. D. Crampton, J. Hutchings, and A. Cowley, Astrophys. J. **299**, 839 (1985).
27. G. Cusumano, T. di Salvo, L. Burderi, *et al.*, Astron. Astrophys. **338**, L79 (1998).
28. M. Denis, J. Grygorczuk, T. Bulik, *et al.*, in *Proceedings of the 5th INTEGRAL Workshop on "The INTEGRAL Univers,"* Ed. by V. Schönfelder *et al.* (ESA Publ. Division, Noordwijk, 2004), SP-552, p. 295.
29. N. Eismont, A. Ditrikh, G. Janin, *et al.*, Astron. Astrophys. **411**, L37 (2003).
30. T. Endo, M. Ishida, K. Masai, *et al.*, Astrophys. J. **574**, 879 (2002).
31. M. Falanga, J. Bonnet-Bidand, J. Poutanen, *et al.*, Astron. Astrophys. **436**, 647 (2005).
32. E. V. Filippova, A. A. Lutovinov, P. E. Shtykovskiy, *et al.*, Pis'ma Astron. Zh. **30**, 905 (2004) [Astron. Lett. **30**, 824 (2004)].
33. M. Finger, L. Bildsten, D. Chakrabarty, *et al.*, Astrophys. J. **517**, 449 (1999).
34. J. Finley, T. Belloni, and Cassinelli, Astron. Astrophys. **262**, L25 (1992).
35. W. Forman, H. Tananbaum, and C. Jones, Astrophys. J. **206**, 29 (1976).
36. D. Galloway, R. Remillard, E. Morgan, *et al.*, IAU Circ. **8070**, 2 (2003).
37. D. Galloway, E. Morgan, and A. Levine, Astrophys. J. **613**, 1164 (2004).
38. R. Giacconi, H. Gursky, E. Kellogg, *et al.*, Astrophys. J. Lett. **167**, L67 (1971).
39. A. Giangrande, F. Giovannelli, C. Bartolini, *et al.*, Astron. Astrophys., Suppl. Ser. **40**, 289 (1980).
40. M. R. Gilfanov, R. A. Sunyaev, E. M. Churazov, *et al.*, Pis'ma Astron. Zh. **15**, 675 (1989) [Sov. Astron. Lett. **15**, 291 (1989)].
41. Yu. Gnedin and P. Sunyaev, Astron. Astrophys. **36**, 379 (1974).
42. S. A. Grebenev, M. N. Pavlinsky, and R. A. Sunyaev, Pis'ma Astron. Zh. **18**, 570 (1992) [Sov. Astron. Lett. **18**, 228 (1992)].
43. J. Halpern, E. Gotthelf, D. Helfand, *et al.*, Astron. Telegram **289**, 1 (2004).
44. W. Heindl and D. Smith, Astrophys. J. Lett. **506**, L35 (1998).
45. W. Hiltner, J. Werner, and P. Osmer, Astrophys. J. **175**, 19 (1972).
46. M. Iye, Publ. Astron. Soc. Jpn. **38**, 463 (1986).
47. S. Ilovaisky, C. Chevalier, and C. Motch, Astron. Astrophys. **114**, 7 (1982).
48. G. Israel, I. Negueruela, S. Campaha, *et al.*, Astron. Astrophys. **371**, 1018 (2001).
49. R. Kelley, J. Jernigan, A. Levine, *et al.*, Astrophys. J. **264**, 568 (1983a).
50. R. Kelley, S. Rappaport, G. Clark, *et al.*, Astrophys. J. **268**, 790 (1983b).
51. E. Kendziorra, P. Kretschmar, H. Pan, *et al.*, Astron. Astrophys. **291**, L31 (1994).
52. K. Kinugasa, K. Torii, Y. Hashimoto, *et al.*, Astrophys. J. **495**, 435 (1998).
53. M. Kirsch, K. Mukerjee, M. Breitfellner, *et al.*, Astron. Astrophys. **423**, 9 (2004).
54. K. Koyama, I. Asaoka, N. Ushimaru, *et al.*, Astrophys. J. **362**, 215 (1990a).
55. K. Koyama, H. Kunieda, Y. Takeuchi, *et al.*, Publ. Astron. Soc. Jpn. **42**, 59 (1990b).

56. P. Kretschmar, R. Staubert, I. Kreykenbohm, *et al.*, in *Proceedings of the 5th INTEGRAL Workshop on "The INTEGRAL Univers,"* Ed. by V. Schönfelder *et al.* (ESA Publ. Division, Noordwijk, 2004), SP-552, p. 267.
57. I. Kreykenbohm, K. Pottschmidt, P. Kretschmar, *et al.*, in *Proceedings of the 5th INTEGRAL Workshop on "The INTEGRAL Univers,"* Ed. by V. Schönfelder *et al.* (ESA Publ. Division, Noordwijk, 2004), SP-552, p. 333.
58. I. Kreykenbohm, N. Mowlavi, N. Produit, *et al.*, Astron. Astrophys. **433**, L45 (2005).
59. W. Krzeminski, Astrophys. J. **192**, 135 (1974).
60. S. Kuznetsov, M. Falanga, A. Goldwurm, *et al.*, in *Proceedings of the 5th INTEGRAL Workshop on "The INTEGRAL Univers,"* Ed. by V. Schönfelder *et al.* (ESA Publ. Division, Noordwijk, 2004), SP-552, p. 285.
61. A. La Barbera, L. Burderi, T. Di Salvo, *et al.*, Astrophys. J. **553**, 375 (2001).
62. A. La Barbera, C. Ferrigno, S. Piraino, *et al.*, in *Proceedings of the 5th INTEGRAL Workshop on "The INTEGRAL Univers,"* Ed. by V. Schönfelder *et al.* (ESA Publ. Division, Noordwijk, 2004), SP-552, p. 337.
63. F. Lamb, C. Petchik, and D. Pines, Astrophys. J. **184**, 271 (1973).
64. R. Lamb, T. Markert, R. Hartman, *et al.*, Astrophys. J. **239**, 651 (1980).
65. F. Lebrun, J. P. Leray, P. Lavocat, *et al.*, Astron. Astrophys. **411**, L141 (2003).
66. A. Levine, S. Rappoport, J. Deeter, *et al.*, Astrophys. J. **410**, 328 (1993).
67. W. Lewin, G. Ricker, and J. McClintock, Astrophys. J. Lett. **169**, L17 (1971).
68. F. Li, S. Rappaport, and A. Epstein, Nature **271**, 37 (1978).
69. N. Lund, S. Brandt, C. Budtz-Joergesen, *et al.*, Astron. Astrophys. **411**, L231 (2003).
70. A. A. Lutovinov, S. A. Grebenev, R. A. Sunyaev, and M. N. Pavlinsky, Pis'ma Astron. Zh. **20**, 631 (1994) [Astron. Lett. **20**, 538 (1994)].
71. A. A. Lutovinov, S. A. Grebenev, M. N. Pavlinsky, and R. A. Sunyaev, Pis'ma Astron. Zh. **26**, 892 (2000) [Astron. Lett. **26**, 765 (2000)].
72. A. A. Lutovinov, S. V. Molkov, and M. G. Revnivtsev, Pis'ma Astron. Zh. **29**, 803 (2003a) [Astron. Lett. **29**, 713 (2003a)].
73. A. Lutovinov, R. Walter, G. Belanger, *et al.*, Astron. Telegram **155**, 1 (2003b).
74. A. Lutovinov, C. Budtz-Jorgensen, M. Turler, *et al.*, Astron. Telegram **326**, 1 (2004a).
75. A. Lutovinov, S. Tsygankov, M. Revnivtsev, *et al.*, in *Proceedings of the 5th INTEGRAL Workshop on "The INTEGRAL Univers,"* Ed. by V. Schönfelder *et al.* (ESA Publ. Division, Noordwijk, 2004b), SP-552, p. 253.
76. A. Lutovinov, M. Revnivtsev, and S. Molkov, Astron. Telegram **178**, 1 (2004c).
77. A. Lutovinov, M. Revnivtsev, S. Molkov, and R. Sunyaev, Astron. Astrophys. **430**, 997 (2005a).
78. A. Lutovinov, J. Rodriguez, M. Revnivtsev, and P. Shtykovskiy, Astron. Astrophys. **433**, L41 (2005b).
79. A. Lutovinov, M. Revnivtsev, M. Gilfanov, *et al.*, Astron. Astrophys. (2005c) (in press); astro-ph/0411550.
80. M. Maisack, J. Grove, E. Kendziorra, *et al.*, Astron. Astrophys. **325**, 212 (1997).
81. K. Makishima, T. Mihara, M. Ishida, *et al.*, Astrophys. J. **365**, L59 (1990).
82. C. Markwardt and J. Swank, Astron. Telegram **179**, 1 (2003).
83. C. Markwardt, M. Juda, and J. Swank, IAU Circ. **8095**, 2 (2003).
84. N. Marshall and M. Ricketts, Mon. Not. R. Astron. Soc. **193**, 7 (1980).
85. N. Masetti, M. Orlandini, D. Dalfiume, *et al.*, Astron. Astrophys. (in press); astro-ph/0508451 (2005).
86. J. McClintok, H. Bradt, R. Doxsey, *et al.*, Nature **270**, 320 (1977).
87. S. Mereghetti, A. Tiengo, G. L. Israel, *et al.*, Astron. Astrophys. **354**, 567 (2000).
88. S. Molkov, A. Lutovinov, and S. Grebenev, Astron. Astrophys. **411**, 357 (2003).
89. S. Molkov, A. Cherepashchuk, A. Lutovinov, *et al.*, Astron. Astrophys. Lett. **30**, 534 (2004a).
90. S. Molkov, A. Cherepashchuk, M. Revnivtsev, *et al.*, Astron. Telegram **274**, 1 (2004b).
91. R. Morrison and D. McCammon, Astrophys. J. **270**, 119 (1983).
92. D.-S. Moon, S. Eikenberry, and I. Wasserman, Astrophys. J. Lett. **582**, L91 (2003).
93. F. Nagase, Publ. Astron. Soc. Jpn. **41**, 1 (1989).
94. I. Negueruela, P. Roche, J. Fabregat, *et al.*, Mon. Not. R. Astron. Soc. **307**, 695 (1999).
95. I. Negueruela, G. Israel, A. Marco, *et al.*, Astron. Astrophys. **397**, 739 (2003).
96. M. Orlandini and D. Dal Fiume, in *X-Ray Astronomy: Stellar Endpoints, AGN, and the Diffuse X-ray Background,* Ed. by N. E. White, G. Malaguti, and G. G. C. Palumbo (Am. Inst. Phys., New York, 2001); AIP Conf. Proc. **599**, 283 (2001).
97. M. Orlandini, D. Dal Fiume, F. Frontera, *et al.*, Astrophys. J. **500**, 163 (1998).
98. M. Orlandini, D. Dal Fiume, F. Frontera, *et al.*, Adv. Space Res. **25**, 417 (2000).
99. G. Parkes, P. Murdin, and K. Mason, Mon. Not. R. Astron. Soc. **184**, 73 (1978).
100. G. Parkes, K. Mason, P. Murdin, *et al.*, Mon. Not. R. Astron. Soc. **191**, 547 (1980).
101. S. Patel, C. Kouveliotou, A. Tennant, *et al.*, Am. Astron. Soc. Meet. **203**, 3103 (2003).
102. B. Paul and A. Rao, Astron. Astrophys. **337**, 815 (1998).
103. B. Paul, P. C. Agrawal, V. R. Chitnis, *et al.*, Bull. Astron. Soc. India **23**, 478 (1995).
104. M. Pereira, J. Braga, and F. Jablonski, Astrophys. J. **526**, 105 (1999).

105. S. Piraino, A. Santangelo, A. Segreto, *et al.*, Astron. Astrophys. **357**, 501 (2000).
106. R. Price, D. Groves, R. Rodrigues, *et al.*, Astrophys. J. **168**, 7 (1971).
107. Priedhorsky and Terrell, Nature **303**, 681 (1983).
108. J. Pringle and M. Rees, Astron. Astrophys. **21**, 1 (1972).
109. P. Ray and D. Chakrabarty, Astrophys. J. **581**, 1293 (2002).
110. P. Reig, D. Chakrabarty, M. Coe, *et al.*, Astron. Astrophys. **311**, 879 (1996).
111. M. G. Revnivtsev, R. A. Sunyaev, D. A. Varshalovich, *et al.*, Pis'ma Astron. Zh. **30**, 430 (2004) [Astron. Lett. **30**, 382 (2004)].
112. A. Reynolds, A. Parmar, and W. White, Astrophys. J. **414**, 302 (1993a).
113. A. Reynolds, R. Hilditch, W. Bell, and G. Hill, Mon. Not. R. Astron. Soc. **261**, 337 (1993b).
114. R. Remillard, A. Levine, T. Takeshima, *et al.*, IAU Circ. **6826**, 2 (1998).
115. N. Robba, L. Burderi, T. Di Salvo, *et al.*, Astrophys. J. **562**, 950 (2001).
116. M. Roberts, F. Michelson, D. Leahy, *et al.*, Astrophys. J. **555**, 967 (2001).
117. J. Rodiriguez, J. Tomsick, L. Foschini, *et al.*, Astron. Astrophys. **407**, 41 (2003).
118. J. Rodriguez, A. Garau, and S. Grebenev, Astron. Telegram **340**, 1 (2004).
119. F. Rosenberg, C. Eyles, G. Skinner, *et al.*, Nature **226**, 628 (1975).
120. N. Sanduleak and A. Philip, IAU Circ. **3023**, 1 (1976).
121. N. Sato, F. Nagase, N. Kawai, *et al.*, Astrophys. J. **304**, 241 (1986).
122. D. Sharma, R. Sood, G. Strigfellow, *et al.*, Adv. Space Res. **13**, 375 (1993).
123. L. Sidoli, S. Mereghetti, S. Larsson, *et al.*, in *Proceedings of the 5th INTEGRAL Workshop on "The INTEGRAL Univers,"* Ed. by V. Schönfelder *et al.* (ESA Publ. Division, Noordwijk, 2004), SP-552, p. 475.
124. A. Slettebak, Astrophys. J., Suppl. Ser. **59**, 769 (1985).
125. P. Soffitta, J. Tomsick, B. Harmon, *et al.*, Astrophys. J. **494**, 203 (1998).
126. L. Stella, N. White, J. Davelaar, *et al.*, Astrophys. J. Lett. **288**, L45 (1985).
127. J. Stevens, P. Reig, M. Coe, *et al.*, Mon. Not. R. Astron. Soc. **288**, 988 (1997).
128. M. Stollberg, M. Finger, R. Wilson, *et al.*, Astrophys. J. **512**, 313 (1999).
129. J. Swank, R. Remillard, and E. Smith, Astron. Telegram **349**, 1 (2004).
130. T Takeshima, R. Corbet, F. Marshal, *et al.*, IAUC **6826**, 1 (1998).
131. J. Truemper, W. Pietsch, C. Reppin, *et al.*, Astrophys. J. Lett. **219**, L105 (1978).
132. S. S. Tsygankov and A. A. Lutovinov, Pis'ma Astron. Zh. **31**, 427 (2005a) [Astron. Lett. **31**, 380 (2005a)].
133. S. S. Tsygankov and A. A. Lutovinov, Pis'ma Astron. Zh. **31**, 99 (2005b) [Astron. Lett. **31**, 88 (2005b)].
134. S. S. Tsygankov, A. A. Lutovinov, S. A. Grebenev, *et al.*, Pis'ma Astron. Zh. **30**, 596 (2004) [Astron. Lett. **30**, 540 (2004)].
135. P. Ubertini, F. Lebrun, G. Di Cocco, *et al.*, Astrophys. J. **411**, 131 (2003).
136. M. van Kerkwijk, J. van Oijen, and E. van den Heuvel, Astron. Astrophys. **209**, 173 (1989).
137. M. van Kerkwijk, J. van Paradijs, E. Zuiderwijk, *et al.*, Astron. Astrophys. **303**, 483 (1995).
138. Walter & INTEGRAL Survey Team, AAS/High Energy Astrophysics Division, 8 (2004).
139. R. S. Warwick, M. G. Watson, and R. Willingale, Space Sci. Rev. **40**, 429 (1985).
140. C. Winkler, T. J.-L. Courvoisier, G. Di Cocco, *et al.*, Astron. Astrophys. **411**, L1 (2003).
141. N. White, K. Mason, P. Sanford, *et al.*, Mon. Not. R. Astron. Soc. **176**, 91 (1976).
142. N. White, G. Parkes, P. Sanford, *et al.*, Nature **274**, 664 (1978).
143. N. White, J. Swank, and S. Holt, Astrophys. J. **270**, 771 (1983).
144. S. Zhang, B. Harmon, W. Paciesas, *et al.*, Astron. Astrophys., Suppl. Ser. **120**, 227 (1996).

Translated by V. Astakhov

Astronomy Letters, Vol. 31, No. 11, 2005, pp. 748–754. Translated from Pis'ma v Astronomicheskiĭ Zhurnal, Vol. 31, No. 11, 2005, pp. 839–846.

Generation of Magnetic Fluctuations Near a Shock Front in a Partially Ionized Medium

A. M. Bykov[1]* and I. N. Toptygin[2]**

[1] *Ioffe Physicotechnical Institute, Russian Academy of Sciences, ul. Politekhnicheskaya 26, St. Petersburg, 194021 Russia*

[2] *St. Petersburg State Polytechnical University, ul. Politekhnicheskaya 29, St. Petersburg, 195251 Russia*

Received April 25, 2005

Abstract—We investigate the generation mechanism of long-wavelength Alfvénic disturbances near the front of a collisionless shock that propagates in a partially ionized plasma. The wave generation and dissipation rates are calculated in the linear approximation. The instability is attributable to a current of energetic particles upstream of the shock front. The generation of long-wavelength magnetic fluctuations is most pronounced for strong shocks, but the effect is retained for shocks with a moderate particle acceleration efficiency without any noticeable modification of the shock structure by the pressure of accelerated particles. The mode generation time for supernova remnants in a partially ionized interstellar medium is shown to be shorter than their age. Long-wavelength magnetic disturbances determine the limiting energies of the particles accelerated at a shock by the Fermi mechanism. We discuss the application of the mechanism under consideration to explaining the observed properties of the SN 1006 remnant.

Key words: *supernovae and supernova remnants, MHD instability, accelerated particles, magnetic field.*

INTRODUCTION

The acceleration of particles near collisionless shock fronts is an efficient conversion mechanism of the free energy of supersonic magnetized plasma flows into the energy of nonthermal particles. Popular models for the origin of cosmic rays (CRs) consider young supernova remnants as the main sources of high-energy CRs (Berezinskiĭ *et al.* 1990; Ptuskin and Zirakashvili 2003, 2005; Hillas 2005) and shock acceleration as the main generation mechanism of relativistic particles. In models for the collective CR acceleration by multiple interactions with supernova remnants and strong winds from massive early-type stars, ensembles of shocks with various intensities also play a crucial role (Bykov and Toptygin 2001).

The X-ray observations of supernova remnants performed by the Chandra telescope with an angular resolution of ~1 arcsec (see, e.g., Vink 2004) point to an efficient generation mechanism of magnetic fields in the preshock region of the Cas A remnant.

Anisotropic CR distributions can lead to the generation of MHD waves (for a review, see Berezinskiĭ *et al.* 1990). The resonant generation of Alfvén waves by relativistic particles was considered as a possible mechanism of turbulence formation in the Galaxy; it provides the diffusion of CRs with energies up 100 GeV and the multiple scattering of accelerated particles near shock fronts (for a review, see Blandford and Eichler 1987). The nonresonant generation mechanisms of MHD waves can also be efficient near shock fronts. The instability of magnetosonic disturbances propagating in the upstream region of a strong shock modified by a CR pressure gradient is a possible nonresonant generation mechanism of a random magnetic field. The various cases of this instability were considered by Drury (1984), Zank and McKenzie (1987), Berezhko (1986), Chalov (1988), and Zank *et al.* (1990). Recently, Bell (2004) pointed out the possibility of an efficient generation of small-scale Alfvén modes (with scales smaller than the gyroradii of nonthermal particles) in a strong shock propagating in a completely ionized plasma.

In many cases, shocks propagate in a partially ionized medium. For supernova remnants interacting with molecular clouds (e.g., IC 443), the presence of a neutral component upstream of the shock front can lead to peculiar features in the regime of high-energy particle acceleration (see, e.g., Drury *et al.* 1996) and affects significantly the radiation spectra of such remnants (Bykov *et al.* 2000). A certain fraction of neutral hydrogen, helium, and metal atoms reach the

*E-mail: byk@astro.ioffe.ru
**E-mail: cosmos@it10242.spb.edu

shock front even in the case of a supernova remnant in a tenuous medium. These are observed in the optical and ultraviolet spectra of the shock front as a superposition of broad and narrow lines (in particular, for the $H\alpha$ line) in the remnants of SN 1006, Kepler, Tycho, RCW 86, the Cygnus Loop, etc. and are an efficient tool for estimating the shock velocity (Chevalier and Raymond 1978; Raymond 2001).

Below, we calculate the linear growth rate of long-wavelength Alfvénic oscillations excited by accelerated particles with allowance made for the dissipation of MHD oscillations in a medium containing not only a plasma, but also a neutral gas. The latter prevents fast background plasma neutralization of the electric current produced by relativistic particles and leads to a renormalization of the magnetic viscosity, which makes the growth of MHD oscillations possible.

INSTABILITY OF THE PRESHOCK REGION IN A PARTIALLY IONIZED MEDIUM

Let us consider a shock propagating in a partially ionized medium with a magnetic field. The matter upstream of a fairly strong shock front is assumed to be cold, and the gas pressure and viscosity may be disregarded. However, we take into account the Joule dissipation and the pressure of nonthermal particles.

Basic Equations

Let us write the magnetohydrodynamic equations in the preshock region in the rest frame of the shock front:

$$\nabla\times\mathbf{B}=\frac{4\pi}{c}(\mathbf{j}+\mathbf{j}^{\rm cr}),\qquad \nabla\times\mathbf{E}=-\frac{1}{c}\frac{\partial\mathbf{B}}{\partial t},\quad (1)$$

$$\rho\left(\frac{\partial\mathbf{u}}{\partial t}+(\mathbf{u}\cdot\nabla)\mathbf{u}\right)\quad (2)$$
$$=-\nabla P_{\rm cr}-\frac{1}{4\pi}\mathbf{B}\times(\nabla\times\mathbf{B}),$$

where ρ and $\mathbf{u}$ are, respectively, the mass density and the total macroscopic velocity of the medium (including the nonthermal plasma component); $P_{\rm cr}$ is the pressure of the nonthermal component; $\mathbf{E}$ and $\mathbf{B}$ are the total electric and magnetic field strengths; $\mathbf{j}$ is the current excited by these fields in the background plasma; and $\mathbf{j}^{\rm cr}$ is the macroscopic current produced by the accelerated particles. The latter was averaged over small-scale fluctuations and should be considered as the current produced by an extraneous (to the background medium) source. Equation (2) is applicable to describing the motions of the medium with scale lengths exceeding the mean free paths of the nonthermal energetic particles that determine $P_{\rm cr}$ and $\mathbf{j}^{\rm cr}$. The presence of an extraneous current of accelerated particles contributing to the total magnetic field is a major factor of the long-wavelength instability considered below. This distinguishes our case from the previously considered long-wavelength instabilities associated with the CR pressure gradient. An important factor is also the presence of a neutral component in the preshock region (even at a fairly high degree of ionization of the medium). In our analyzed one-dimensional case where all quantities depend on one z coordinate, both currents are transverse relative to the normal to the front plane.

The relation between the current $\mathbf{j}$ and the field vectors should be added to the above equations. In a medium with a fraction of neutral matter, this relation largely determines the form of Ohm's generalized law and the dissipative effect (i.e., the magnetic viscosity). This question has been explored in detail in the past decades (see Pikel'ner 1964; Ruzmaĭkin *et al.* 1988). We use Ohm's generalized law in the form given in the monograph by Pikel'ner (1966):

$$\mathbf{E}+\frac{1}{c}\mathbf{u}\times\mathbf{B}=\frac{1}{\sigma}\mathbf{j}+\frac{1}{n_iec}\mathbf{j}\times\mathbf{B}\quad (3)$$
$$+\frac{F^2\tau_i}{n_im_ic^2}\mathbf{B}\times(\mathbf{j}\times\mathbf{B}),$$

where $\mathbf{j}$ is the current of background particles of a partially ionized plasma, $\mathbf{E}$ and $\mathbf{B}$ are the vectors of the total field produced by the current $\mathbf{j}$ and other (external) sources, $n_i\approx n_e$ are the number densities of the charged components, and τ_i and τ_e are the mean times between collisions of ions and electrons, respectively, with other particles (in our case, mainly with neutral atoms and molecules). Finally, $\sigma=n_ee^2\tau_e/m_e$ is the collisional electric conductivity and F is the mass fraction of the neutral particles. In a warm medium and neutral clouds far from the shock front, the fraction $F\approx1$, but the ionizing radiation of the gas heated by a strong shock decreases appreciably in the preshock region, where neutral helium atoms can play an important role.

For a magnetized plasma with an admixture of neutrals with $\omega_B\tau\gg1$ (here, $\omega_B=eB_0/(mc)$), the three terms on the right-hand side of Eq. (3) differ by many orders of magnitude. The ratio of the third and second terms yields $\tau_ieB_0/(m_ic)=\omega_{Bi}\tau_i\gg1$. The ratio of the third and first terms is of the order of $\tau_iB_0^2\sigma/(n_im_ic^2)=(\omega_{Bi}\tau_i)(\omega_{Be}\tau_e)\gg1$. These estimates become invalid only if the transverse (relative to $\mathbf{B}$) current component is anomalously small. However, the current is transverse in the case under consideration. Let us retain only the last term on the right-hand side of Eq. (3) and substitute $\mathbf{B}=\mathbf{B}_0+\mathbf{b}$, $\mathbf{j}=(c/4\pi)\nabla\times\mathbf{b}-\mathbf{j}^{\rm cr}$ into it. This yields the following after linearization: $\mathbf{B}\times(\mathbf{j}\times\mathbf{B})=(cB_0^2/(4\pi))\nabla\times\mathbf{B}-B_0^2\mathbf{j}^{\rm cr}$. Eliminating the electric

field $\mathbf{E}$ from (3) and (1), we obtain a linearized equation for the magnetic field in the standard form,

$$\frac{\partial \mathbf{b}}{\partial t} + (\mathbf{u}\cdot\nabla)\mathbf{b} = (\mathbf{B}_0\cdot\nabla)\mathbf{u}_\perp + \nu_\mathrm{m}\triangle\mathbf{b} + \frac{4\pi\nu_\mathrm{m}}{c}\nabla\times\mathbf{j}^\mathrm{cr}, \quad (4)$$

but with an essentially renormalized magnetic viscosity, which we express in terms of the effective electric conductivity σ_ef:

$$\nu_\mathrm{m} = \frac{c^2}{4\pi\sigma_\mathrm{ef}} = \frac{F^2\tau_i B_0^2}{4\pi n_i m_i}.$$

The linearized equation of motion for the medium (2) takes the form

$$\rho\left(\frac{\partial \mathbf{u}_\perp}{\partial t} + (\mathbf{u}\cdot\nabla)\mathbf{u}_\perp\right) = -\frac{1}{4\pi}\mathbf{B}_0\times(\nabla\times\mathbf{b}). \quad (5)$$

The pressure gradient of nonthermal particles does not appear in the equation for the transverse velocity. Now the constant velocity component of the preshock medium perpendicular to the shock front is denoted in Eqs. (4) and (5) by $\mathbf{u}$ without any subscript. The small velocity component parallel to the shock front has the subscript $\perp$. In what follows, we will consider a purely hydrogen medium with $m_i = m_p$ and $\omega_{Bi} = \omega_{Bp}$.

Calculating the Current of Accelerated Particles

Let us calculate the electric current that is generated by nonthermal particles under the electric and magnetic fields of an MHD oscillation. Denote these fields by $\mathbf{b}$ and $\mathbf{E}$ and consider the case with the simplest geometry where the external field $\mathbf{B}_0$ is uniform and directed along the normal to a plane boundless front, while the MHD oscillation field is perpendicular to the external field ($\mathbf{b}\perp\mathbf{B}_0$) and is a plane wave propagating along $\mathbf{B}_0$: $\mathbf{b} = \mathbf{b}_0 e^{i(\mathbf{k}\cdot\mathbf{r}-\omega t)}$, $\mathbf{k} = k\mathbf{e}_{||}$. The electric field of the wave is related to the magnetic field by the electromagnetic induction equation

$$\mathbf{k}\times\mathbf{E} = \frac{\omega}{c}\mathbf{b}, \qquad \mathbf{E} = -\frac{\omega}{ck}\mathbf{e}_{||}\times\mathbf{b}.$$

We perform our analysis in the rest frame of the shock front.

The distribution function $f(\mathbf{r}, p_\perp, p_{||}, \phi, t)$ of relativistic particles in the geometry of the problem under consideration satisfies the equation

$$\frac{\partial f}{\partial t} + \mathbf{v}\cdot\frac{\partial f}{\partial \mathbf{r}} + e\mathbf{E}\cdot\frac{\partial f}{\partial \mathbf{p}} - \frac{ec}{\varepsilon}(\mathbf{B}_0+\mathbf{b})\cdot\mathcal{O}f = I[f], \quad (6)$$

where

$$\mathcal{O} = \mathbf{p}\times\frac{\partial}{\partial \mathbf{p}}$$

is the momentum rotation operator, ε is the particle energy, and $I[f]$ is the collision integral averaged over the turbulent spectrum that includes the interaction of relativistic particles with MHD turbulence. Specific expressions for this quantity in the lowest-order approximation in turbulence amplitude can be found in a monograph by Toptygin (1985), while nonlinear corrections are given in our previous review (Bykov and Toptygin 1993).

Let us linearize kinetic equation (6) by assuming the external field to be weak and by separating out the small part δf attributable to this field from the distribution function $f = f_0 + \delta f$:

$$\frac{\partial \delta f}{\partial t} + \mathbf{v}\cdot\frac{\partial \delta f}{\partial \mathbf{r}} - \frac{ec}{\varepsilon}\mathbf{B}_0\cdot\mathcal{O}\delta f = -e\mathbf{E}\cdot\frac{\partial f_0}{\partial \mathbf{p}} + \frac{ec}{\varepsilon}\mathbf{b}\cdot\mathcal{O}f_0 \equiv Q(\mathbf{p}, z, t). \quad (7)$$

Here, f_0 is the stationary (in the rest frame of the shock front) distribution function of the accelerated particles in the absence of the MHD wave under consideration. The accelerated particles undergo strong scattering and have a weakly anisotropic distribution function that can be written as (Toptygin 1985)

$$f_0(z,\mathbf{p}) = \frac{1}{4\pi}\left[N(p,z) + \frac{3}{pv}\mathbf{p}\cdot\mathbf{J}(p,z)\right], \quad (8)$$
$$J \ll vN,$$

where

$$J_\alpha = -\kappa_{\alpha\beta}\frac{\partial N}{\partial x_\beta} - \frac{p}{3}\frac{\partial N}{\partial p}u_\alpha \quad (9)$$

is the differential flux density of the accelerated particles, $\kappa_{\alpha\beta}$ is their diffusion tensor, and $\mathbf{u}$ is the velocity of the medium. The applicability of relations (8) and (9) is limited by the condition $u \ll v$.

The isotropic part $N(p,z)$ of the distribution function in the preshock region can be easily calculated in the stationary case:

$$N(p,z) = (\alpha-3)N_0\frac{p_0^{\alpha-3}}{p^\alpha} \times \exp\left[\int_0^z \frac{u\,dz'}{\kappa_{||}(p,z')}\right], \quad (10)$$
$$z \le 0, \quad p_0 \le p \le p_m.$$

Here, N_0 is the number density of relativistic particles with all energies, $\alpha = 3u/\Delta u$ is the spectral index, and $\Delta u > 0$ is the jump in velocity at the shock front. Solution (10) corresponds to the acceleration of

test particles where a small part of the shock energy flux is transferred to them. In this case, the shock front modification by the accelerated particles may be disregarded and the velocity of the medium in the preshock region may be assumed to be approximately constant, $u \approx \text{const}$. The spectral index is $\alpha > 4$ for a moderately strong shock front and $\alpha \le 4$ for a strong shock (see, e.g., Toptygin 1997). The specific value of α depends not only on the Mach number of the wave, but also on the rate of particle injection into the acceleration process. At $\alpha < 4$, the bulk of the energy belongs to the most energetic particles with $\varepsilon \lesssim \varepsilon_{\rm m} = cp_{\rm m}$, and several tens of percent of the total flow energy is spent on particle acceleration. In this calculation, we restrict ourselves to spectral indices $\alpha \ge 4$, suggesting a moderate acceleration rate at which the total kinetic energy of the accelerated particles generally does not exceed 10% of the system's total energy, although the maximum particle momentum $p_{\rm m}$ can be much larger than the injection momentum: $p_{\rm m} \gg p_0$. At such spectral indices, the total energy of the accelerated particles at the shock front ($z = 0$) depends on p_m very weakly not more strongly than the logarithmic law:

$$w_{\rm cr} \approx \int_{p_0}^{p_m} cpN(p,0)p^2dp = \frac{\alpha-3}{\alpha-4}N_0m_pc^2, \quad (11)$$

$$\alpha > 4; \quad \frac{\alpha-3}{\alpha-4} \to \ln\frac{p_m}{p_0} \quad \text{at} \quad \alpha \to 4.$$

At an arbitrary spectral index $\alpha \ge 4$, the particle distribution function and the current take the form

$$f_0(z,\mathbf{p}) = \frac{(\alpha-3)N_0p_0^{\alpha-3}}{4\pi p^\alpha} \times \left[1 + \frac{u}{v}(\alpha-3)\cos\theta\right] e^{uz/\kappa_\parallel},$$

$$Q(\phi) = (\mathbf{b}\cdot\mathbf{e}_\phi)\frac{(\alpha-3)eN_0p_0^{\alpha-3}}{4\pi\Omega p^{\alpha+1}} \times \left[(\alpha-3)\frac{u}{c} - \frac{\omega}{ck}\left(\alpha + \frac{u}{v}(\alpha+1)(\alpha-3)\cos\theta\right)\right] \times e^{uz/\kappa_\parallel}\sin\theta,$$

$$\delta f = \int_{\pm\infty}^{\phi} Q(\phi')e^{a(\phi-\phi')}d\phi' = (\mathbf{b}\cdot\mathbf{e}_\phi)\frac{(\alpha-3)eN_0p_0^{\alpha-3}}{4\pi\Omega p^{\alpha+1}} \times \left[(\alpha-3)\frac{u}{c} - \frac{\omega}{ck}\left(\alpha + \frac{u}{v}(\alpha+1)(\alpha-3)\cos\theta\right)\right] \times \frac{\mathbf{b}\cdot\mathbf{e}_\perp - a\mathbf{b}\cdot\mathbf{e}_\phi}{1+a^2}e^{uz/\kappa_\parallel}\sin\theta,$$

where

$$a = \frac{1}{\Omega}[v_\parallel u/\kappa_\parallel - i(\omega - kv_\parallel)].$$

The expression for the current of relativistic particles can be reduced to

$$\mathbf{j}^{\rm cr} = \int e\mathbf{v}\delta f(p,\theta,\phi)p^2dp\sin\theta d\theta d\phi = \int p^2dp\sin^3\theta d\theta\frac{(\alpha-3)ve^2N_0p_0^{\alpha-3}}{4\Omega p^{\alpha+1}} \times \left[(\alpha-3)\frac{u}{c} - \frac{\omega}{ck}\left(\alpha + \frac{u}{v}(\alpha+1)(\alpha-3)\cos\theta\right)\right] \times \frac{\mathbf{b} + a\mathbf{e}_\parallel\times\mathbf{b}}{1+a^2}e^{uz/\kappa_\parallel}.$$

In the previous formulas, except formula (11), there was no substitution $v \to c$; these are also valid for nonrelativistic energies, but at $v \gg u$. Below, we consider the relativistic case, $v \approx c$, $p_0 = m_pc$.

At present, there is no consistent theory to calculate the turbulence spectrum in the vicinity of a shock. The turbulence-determined diffusion coefficient of energetic particles has to be specified from model considerations. The Bohm diffusion model is most popular (see, e.g., the reviews by Jones and Ellison 1991 and Malkov and Drury 2001). This model assumes strong turbulence at which the local transport mean free path $\Lambda(p)$ of a particle is of the order of its gyroradius:

$$\Lambda(p) \approx \eta r_{\rm g}(p) = \frac{cp}{eB},$$

$$\tilde\kappa_\parallel = \frac{c\Lambda}{3}, \quad p_0 \le p \le p_{\rm m},$$

where the parameter $\eta \gtrsim 1$ and p_0 and $p_{\rm m}$ bound the range of momenta under consideration; the case of $p_{\rm m} \gg p_0$ is of considerable interest. The turbulent and regular fields are assumed to be of the same order of magnitude: $B \approx B_0$. The latter condition is consistent with the assumption of a minor fraction of the energy being transferred to the accelerated particles, since the mechanical energy density in a strong shock under typical astrophysical conditions is several orders of magnitude higher than the energy density of the primary magnetic field. The pattern of particle transport depends on the relationship between the local diffusion coefficient $\tilde\kappa_\parallel$ and the parameters of the turbulent plasma motions with scale lengths exceeding Λ. If the fluctuation amplitude of the macroscopic velocity of the medium $\delta u(l)$ with a scale length $l \gg \Lambda$ is so large that $\delta u l \gtrsim \tilde\kappa_\parallel$, then the turbulent particle transport will play a major role on these scales. In this model, the diffusion coefficient does not depend on the particle energy over a wide energy range (Bykov and Toptygin 1993).

The solution of kinetic equation (7) for a constant diffusion coefficient has the simplest form that we consider below, although there are no fundamental difficulties in considering systems with $\kappa_\parallel(p)$ dependent on the momentum p. For the CR current after calculating the integrals, we obtain

$$\mathbf{j}^{\rm cr} = -(\sigma'_{\rm cr} + i\sigma''_{\rm cr})\mathbf{e}_\parallel \times \mathbf{b} + (g' + ig'')\mathbf{b}, \qquad (12)$$

where the following notation is used:

$$\sigma'_{\rm cr} = \frac{(\alpha-3)^2\omega_0^2\omega u}{8(\alpha-1)\omega_{Bp}^2 c}\left(\frac{ck}{\omega_{Bp}}\right)^{\alpha-4},$$

$$\sigma''_{\rm cr} = \frac{(\alpha+1)(\alpha-3)^2\omega_0^2\omega u}{60\pi(\alpha-4)\omega_{Bp}^2 c},$$

$$g' = -\frac{\omega_0^2}{12\pi\omega_{Bp}}\left(\frac{3u}{c} + \alpha\frac{\omega-uk}{ck}\right),$$

$$g'' = \frac{(\alpha-3)\omega_0^2}{8\alpha(\alpha-2)\omega_{Bp}}\left(\frac{ck}{\omega_{Bp}}\right)^{\alpha-3}\left(\frac{3u}{c} + \alpha\frac{\omega-uk}{ck}\right),$$

$$\omega_0^2 = \frac{4\pi e^2 N_0}{m_p}, \qquad \xi_0 = \frac{\omega_{Bp}}{ck}.$$

When passing to $\alpha \to 4$, we should make the substitution $(\alpha-4)^{-1} \to \ln\xi_0 + 8/15$.

The current can also be represented in a conventional form similar to Ohm's law in a gyrotropic medium, $\mathbf{j}^{\rm cr} = \sigma_{\rm ef}\mathbf{E} + \sigma_{\rm H}\mathbf{e}_\parallel \times \mathbf{E}$, but representation (12) in the MHD approximation is more convenient.

The Growth Rate of MHD Waves

Equations (4) and (6) together with the extraneous current of relativistic particles (12) allow us to derive a dispersion relation for the waves that can be excited in a weakly ionized medium with an admixture of nonthermal energetic particles. We seek a solution of these equations for $|z| \ll \kappa_\parallel/u$ in the form $\mathbf{b}$, $\mathbf{u}_\perp \propto e^{i(kz-\omega t)}$. Equation (5) allows the transverse velocity to be expressed in terms of the magnetic field:

$$\mathbf{u}_\perp = \frac{kB_0}{4\pi\rho\omega'}\mathbf{b},$$

where $\omega' = \omega - uk$ is the oscillation frequency in the frame of reference comoving with the medium. Using this relation, we derive a system of equations for the magnetic field components from Eqs. (4) and (12):

$$\left\{\omega'^2 - (u_{\rm A}k)^2 + \frac{4\pi}{c}\nu_{\rm m}\sigma'_{\rm cr}k\omega' + i\nu_{\rm m}k^2\omega' \times \left[1 + \frac{4\pi}{ck}\sigma''_{\rm cr}\right]\right\}b_x - \frac{4\pi}{c}\nu_{\rm m}(g' + ig'')k\omega' b_y = 0,$$

$$\frac{4\pi}{c}\nu_{\rm m}(g' + ig'')k\omega' b_x + \left\{\omega'^2 - (u_{\rm A}k)^2 + \frac{4\pi}{c}\nu_{\rm m}\sigma'_{\rm cr}k\omega' + i\nu_{\rm m}k^2\omega'\left[1 + \frac{4\pi}{ck}\sigma''_{\rm cr}\right]\right\}b_y = 0,$$

where $u_{\rm A}$ is the Alfvén velocity. Equating the determinant of this system to zero yields a dispersion relation that defines several oscillation branches:

$$\omega'^2 - (u_{\rm A}k)^2 + \frac{4\pi}{c}\nu_{\rm m}(\sigma'_{\rm cr} \mp g')k\omega' + i\nu_{\rm m}k^2\omega'\left[1 + \frac{4\pi}{ck}(\sigma''_{\rm cr} \pm g')\right] = 0. \qquad (13)$$

In the absence of energetic nonthermal particles ($\sigma_{\rm cr} = g = 0$), we obtain a dispersion relation that describes damped Alfén waves:

$$\omega' = \pm u_{\rm A}k - i\gamma, \qquad \gamma = \frac{1}{2}\nu_{\rm m}k^2$$

(in the approximation of $\gamma \ll u_{\rm A}k$). In the presence of energetic nonthermal particles, the term in square brackets is added to the imaginary part in Eq. (13); this term can have different signs, since $\sigma''_{\rm cr}/g' \approx u\ln\xi_0/c \ll 1$. The oscillation branch that corresponds to the plus in front of g' at fairly low values of

$$k < k_{\rm c} = \frac{4\pi}{c}|g'|$$

will grow, $\mathbf{b} \propto e^{\gamma t}$, at a rate

$$\gamma \approx \frac{1}{2}\nu_{\rm m}k^2\left(\frac{4\pi|g'|}{ck} - 1\right). \qquad (14)$$

Significantly, the nonresonant generation mechanism of long-wavelength magnetic fluctuations in a partially ionized medium requires no pressure gradient (or other inhomogeneity) in the preshock region. This distinguishes it from the previously mentioned instabilities of an inhomogeneous preshock region modified by the CR pressure. However, one might expect growth rate (14) to remain valid an order of magnitude up to $k \gtrsim 2\pi/l_{\rm m} \approx 2\pi u/\kappa_\parallel$ in the presence of an inhomogeneous preshock region as well. The front inhomogeneity can be consistently taken into account in the geometrical optics approximation in a way similar to that used by Chalov (1988). A certain renormalization of the real part of the frequency also takes place. The presence of a neutral component (even with a relatively low mass fraction F) in the case of a magnetized medium with $\omega_{Bi}\tau \gg 1$ changes radically Ohm's law and gives rise to long-wavelength instability. For a shock with an Alfvén Mach number $M_{\rm A} > 4$, the estimate of growth rate (14) is

$$\gamma \sim \frac{F^2}{6}(\omega_{Bi}\tau_i)\frac{N_0}{n_i}ku. \qquad (15)$$

THE GENERATION OF MAGNETIC FIELD FLUCTUATIONS IN THE SHOCKS OF SUPERNOVA REMNANTS

Let us consider the possible applications of the Alfvén wave generation mechanism in the shock of the SN 1006 remnant considered above. This is one of the young supernova remnants known from ancient historical chronicles (Lozinskaya 1986), and it probably belongs to type-Ia supernovae. The X-ray emission from the SN 1006 remnant is characterized by bright thin segments located in the northeast (NE) and southwest (SW) parts of a roughly spherical shell $\sim 30'$ in diameter. The bright NE part has recently been studied in detail in the Chandra X-ray observatory by Long *et al.* (2003) and Bamba *et al.* (2003). The X-ray spectrum of the thin bright NE segment is dominated by a nonthermal continuum that is commonly interpreted as the synchrotron radiation of electrons with energies of $\sim 10-100$ TeV in the vicinity of a shock. The high angular resolution ($\sim 1''$) of the ACIS CCD detector in the Chandra observatory allowed Long *et al.* (2003) to detect a sharp jump in radiation intensity. They established that the intensity of the radiation at energies above 1.2 keV immediately upstream of the shock front does not exceed 1.5% of the maximum brightness immediately downstream of the shock front. The bright NE segment of the X-ray synchrotron radiation is $\approx 10''$ in width ($1'' = 3.3 \times 10^{16}$ cm at an estimated distance to SN 1006 of 2.2 kpc). The presence of a weak radio halo in remnant supernovae and estimates of the diffusion coefficients for relativistic electrons were previously discussed by Achterberg *et al.* (1994), but the upper limit on the brightness of the synchrotron halo set by Long *et al.* (2003) is most stringent (see Ballet 2005).

The optical and ultraviolet spectra of SN 1006 obtained by Korreck *et al.* (2004) agree with the estimates of the neutral mass fraction $F \sim 0.1$ in the upstream region of a shock propagating with a velocity $v_{\rm sh} \sim 2300$ km s^{-1}. The gas density upstream of the front of the NE sector of the shock in SN 1006 was estimated to be $n_i \sim 0.1$ cm^{-3}. Using the hydrogen charge exchange reaction rate at a temperature of $\sim 10^4$ K from Kulsrud and Cesarsky (1971), we obtain the mean free path of a hydrogen atom relative to charge exchange equal to the minimum instability wavelength $\lambda_0 = 2\pi k_0^{-1} \sim 2 \times 10^{16}$ cm (since $k_0 \ll k_{\rm c}$) and an estimate of the magnetization factor, $\omega_{Bi}\tau_i \gtrsim 10^7 B n_{-1}$, where B is measured in μG. Thus, using relation (15), we obtain a characteristic mode growth time scale of $\sim 6 \times 10^2 (N_0/n_i)^{-1}$ (s), which allows magnetic fields with scale lengths of the order of λ_0 to be amplified over the lifetime of SN 1006 if the rate of proton injection into the acceleration process at the shock admits of $N_0/n_i \gtrsim 10^{-7}$. Using relation (11), we can make sure that the energy density of the accelerated particles accounts for a few fractions of a percent of the onflow kinetic energy density. If we restrict our analysis to injection rates that admit of CR energy densities $w_{\rm cr}$ on the order of several percent of the flow kinetic energy density ($\sim m_p n_i v_{\rm sh}^2$), then we will get the possibility of the generation of magnetic field fluctuations upstream of the shock front with amplitudes of $\delta B \sim 30$ μG. A compression of the transverse field component at the discontinuity in a strong shock with $R \approx 4$ (here, we consider a single-fluid wave without an extended preshock region, since we investigate the case of low proton injection rates) can yield magnetic fields of ~ 100 μG in the postshock region. Magnetic fields in the postshock region of SN 1006 of ~ 100 μG allow the observed intensity distribution of the X-ray continuum emission in the NE segment of the shock (Long *et al.* 2003; Berezhko *et al.* 2003; Ballet 2005) to be explained in terms of the rapid synchrotron cooling of relativistic electrons downstream of the shock front. In the case of magnetic field generation in a partially ionized medium, no significant pressure of the CR nucleon component ($\sim m_p n_i v_{\rm sh}^2$), assumed in the model by Berezhko *et al.* (2003) in the preshock region, is required. The upper limit for the ratio of the synchrotron luminosity upstream of the shock front to the maximum luminosity in the transverse segment of the shock is $R^{-\Gamma}$, where Γ is the photon spectral index of the synchrotron radiation at energies above ~ 1.5 keV. In our case of compression in a strong single-fluid shock with $R \approx 4$ and a synchrotron index $\Gamma \sim 3$, we obtain a ratio of the specific luminosities close to 1.5%, in agreement with the limit set by Long *et al.* (2003).

Another interesting application of the physical mechanism of magnetic field generation by a shock in a plasma medium with a neutral component may be radio filaments near the Galactic center (Morris and Serabyn 1996). The observations by Yusef-Zadeh *et al.* (2005) point to the possible association of some of the filaments with supernova remnants.

CONCLUSIONS

We investigated a new type of instability of a partially ionized plasma with relativistic particles accelerated at a strong shock front. Alfvénic MHD waves are excited by a nonresonant mechanism upstream of the shock front. Applying this mechanism to the remnant of SN 1006 allows us to explain the main features of the emission from this remnant and the possible magnetic field amplification downstream of the shock front (~ 100 μG) without assuming a significant nonlinear modification of the profile of the preshock region by the accelerated particles.

ACKNOWLEDGMENTS

This work was supported in part by the Russian Foundation for Basic Research (project nos. 03-02-17433 and 04-02-16595) and the "Development of the Scientific Potential of Higher Schools" program, the "Basic Research" subprogram 1 (project no. UR.02.01.289).

REFERENCES

1. A. Achterberg, R. Blandford, and S. Reynolds, Astron. Astrophys. **281**, 220 (1994).
2. J. Ballet, astro-ph/0503309 (2005).
3. A. Bamba, R. Yamazaki, M. Ueno, and K. Koyama, Astrophys. J. **589**, 827 (2003).
4. A. R. Bell, Mon. Not. R. Astron. Soc. **353**, 550 (2004).
5. E. G. Berezhko, Pis'ma Astron. Zh. **12**, 842 (1986) [Sov. Astron. Lett. **12**, 352 (1986)].
6. E. G. Berezhko, L. T. Ksenofontov, and H. J. Volk, Astron. Astrophys. **412**, L11 (2003).
7. V. S. Berezinskiĭ, S. V. Bulanov, V. L. Ginzburg, *et al.*, *Cosmic-Ray Astrophysics,* Ed. by V. L. Ginzburg (Nauka, Moscow, 1990).
8. R. D. Blandford and D. Eichler, Phys. Rep. **154**, 1 (1987).
9. A. M. Bykov, R. A. Chevalier, D. C. Ellison, and Yu. A. Uvarov, Astrophys. J. **538**, 203 (2000).
10. A. M. Bykov and I. N. Toptygin, Usp. Fiz. Nauk **163** (11), 19 (1993) [Phys. Usp. **36**, 1020 (1993)].
11. A. M. Bykov and I. N. Toptygin, Pis'ma Astron. Zh. **27**, 735 (2001) [Astron. Lett. **27**, 625 (2001)].
12. S. V. Chalov, Pis'ma Astron. Zh. **14**, 272 (1988) [Sov. Astron. Lett. **14**, 114 (1988)].
13. R. A. Chevalier and J. C. Raymond, Astrophys. J. Lett. **225**, L27 (1978).
14. L. O'C. Drury, Adv. Space Res. **4**, 185 (1984).
15. L. O'C. Drury, P. Duffy, and J. G. Kirk, Astron. Astrophys. **309**, 1002 (1996).
16. A. M. Hillas, J. Phys. G **31**, R95 (2005).
17. F. C. Jones and D. C. Ellison, Space Sci. Rev. **58**, 259 (1991).
18. K. E. Korreck, J. C. Raymond, T. H. Zurbuchen, and P. Ghavamian, Astrophys. J. **615**, 280 (2004).
19. R. M. Kulsrud and C. J. Cesarsky, Astrophys. Lett. **8**, 189 (1971).
20. K. S. Long, S. P. Reynolds, J. C. Raymond, *et al.*, Astrophys. J. **586**, 1162 (2003).
21. T. A. Lozinskaya, *Supernovae and Stellar Wind in the Interstellar Medium* (Nauka, Moscow, 1986; American Inst. of Physics, New York, 1992).
22. M. A. Malkov and L. O'C. Drury, Rep. Prog. Phys. **64**, 429 (2001).
23. M. Morris and E. Serabyn, Annu. Rev. Astron. Astrophys. **34**, 645 (1996).
24. S. P. Pikelner, *Fundamentals of Cosmic Electrodynamics* (NASA, Washington, D.C., 1964; Fizmatgiz, Moscow, 1966).
25. V. S. Ptuskin and V. N. Zirakashvili, Astron. Astrophys. **403**, 1 (2003).
26. V. S. Ptuskin and V. N. Zirakashvili, Astron. Astrophys. **429**, 755 (2005).
27. J. C. Raymond, Space Sci. Rev. **99**, 209 (2001).
28. A. A. Ruzmaĭkin, D. D. Sokolov, and A. M. Shukurov, *Magnetic Fields of Galaxies* (Nauka, Moscow, 1988).
29. I. N. Toptygin, *Cosmic Rays in Interplanetary Magnetic Fields* (Reidel, Dordrecht, 1985).
30. I. N. Toptygin, Zh. Éksp. Teor. Fiz. **112**, 1584 (1997) [JETP **85**, 862 (1997)].
31. J. Vink, Adv. Space Res. **33**, 356 (2004).
32. F. Yusef-Zadeh, M. Wardle, M. Muno, *et al.*, astro-ph/0502260 (2005).
33. G. P. Zank, W. I. Axford, and J. F. McKenzie, Astron. Astrophys. **233**, 275 (1990).
34. G. P. Zank and J. F. McKenzie, J. Plasma Phys. **37**, 347 (1987).

Translated by V. Astakhov

Astronomy Letters, Vol. 31, No. 11, 2005, pp. 755–759. Translated from Pis'ma v Astronomicheskiĭ Zhurnal, Vol. 31, No. 11, 2005, pp. 847–852.

Possible Origin of Clusters in Ultra-High-Energy Cosmic Rays

A. V. Uryson*

Lebedev Physical Institute, Russian Academy of Sciences, Leninskiĭ pr. 53, Moscow, 117924 Russia

Received March 10, 2005

Abstract—We estimate the detection rate of ultra-high-energy cosmic rays on ground-based arrays by assuming that the cosmic-ray sources are active galactic nuclei. We analyze the cases of detection of clusters, several particles that arrived, within the error limits, from the same area of the sky. The adopted model is shown to explain the detection rate of clusters on the AGASA array. © *2005 Pleiades Publishing, Inc.*

Key words: *cosmic rays, nonthermal radiation processes.*

INTRODUCTION

The origin of ultra-high-energy cosmic rays (UHECRs), $E > 4 \times 10^{19}$ eV, has not yet been elucidated. In our opinion, the sources of UHECRs are active galactic nuclei (AGNs). This is an old hypothesis that was discussed in the late 1960s and with which the AGN space density estimates (Berezinskiĭ *et al.* 1990) were consistent. The identification of CR sources performed by Uryson (1996, 2001a, 2004a), Tinyakov and Tkachev (2001), and Gorbunov *et al.* (2002) has shown that Seyfert nuclei with redshifts $z < 0.01$ and BL Lac objects are possible sources of UHECRs.

On their way from the source to the Earth, UHECRs are deflected by magnetic fields in intergalactic space and in the Galaxy. When identifying the sources, we assumed that CRs are deflected by the intergalactic magnetic fields through no more than 9°. The intergalactic magnetic fields are $B < 10^{-9}$ G (Kronberg 1994), and this condition is satisfied for the particles arrived from distances of ~50 Mpc, i.e., emitted by Seyfert nuclei with $z < 0.01$ (Uryson 2001b). BL Lac objects are hundreds of megaparsecs away, but even for such distant sources, the deflections may not exceed a few degrees if the filamentary structure of the intergalactic magnetic fields is taken into account (Dolag *et al.* 2004). The field in the Galaxy has regular and irregular components; the field strength is $B \sim 10^{-6}$ G. In the disk, the field is regular in the spiral arms and directed along them; in the halo, the regular component is perpendicular to the disk (Kronberg 1994). The deflections of particles in the regular field depend on the particle arrival direction and can be negligible. In the irregular field, the deflections do not exceed 1°. Therefore, our identification is valid for CRs arriving from fairly high Galactic latitudes (in all our identification works, we selected UHECRs depending on the Galactic latitude of their arrival).

Our identification of sources was based on a statistical analysis. The major CR sources can be revealed in this way, but it is difficult to exclude other hypotheses. For instance, there are UHECR particles that have arrived from areas of the sky where there are neither Seyfert nuclei with $z < 0.01$ nor BL Lac objects. This may be because the catalogs of objects are incomplete; they do not contain all objects of a given type, and, as a result, some particles arrive from "empty" areas of the sky. (For this reason, the sources can be identified only statistically.) However, a different explanation is possible: statistical analysis has revealed the major CR sources, but there are also other, less efficient or rarer sources. CRs in the arrival direction of which no object of the "major" type is observed originate from these "minor" sources. To reliably establish the CR sources, we must find out whether conditions for UHECR acceleration exist in the identified objects and compare the model predictions with experimental data.

Particle acceleration in the identified objects was considered by Kardashev (1995), Shatskiĭ and Kardashev (2002), and Uryson (2001b, 2004b). They showed that conditions for particle acceleration to energies of 10^{21} eV exist in the identified objects. The CR spectra near the Earth obtained in the model under consideration agree, within the error limits, with the measured spectra (Uryson 2004c).

Here, we analyze the clusters detected in UHECRs, groups of particles with coincident (within the error limits) arrival directions, and consider how the existence of clusters can be explained in our model.

*E-mail: uryson@sci.lebedev.ru

1063-7737/05/3111-0755$26.00

THE UHECR DETECTION RATE FROM A SINGLE SOURCE

Let us estimate the detection rate of UHECRs emitted by a single source on ground-based arrays with an area $S \approx 10$ km^2 (the Yakutsk, Haverah Park, Akeno, and Volcano Ranch arrays have approximately the same area) and $S \approx 100$ or 3000 km^2 (the areas of the AGASA and Pierre Auger arrays).

Let us first consider Seyfert nuclei. To provide the observed intensity of CRs with energies $E > 5 \times 10^{19}$ eV, $I(E) \approx 10^{-39}$–10^{40} (cm^2 s sr eV)$^{-1}$ (Nagano and Watson 2000), a Seyfert nucleus spends an estimated power of $L_S \approx 10^{39}$–10^{40} erg s^{-1} on the emission of UHECRs (Uryson 2001b, 2004a).

This estimate was obtained by assuming that the particles are emitted by the source isotropically. However, in our acceleration model (Uryson 2001b, 2004b), the particles are accelerated in a jet and are emitted in a directed beam with an opening half-angle of $\theta \leq 6.5 \times 10^{-4}$. Taking into account the possible charge conversion of the accelerated particles (Derishev *et al.* 2003), we find that UHECRs are emitted in a cone with an angle of 20°. It thus follows that the sources of the detected CRs are Seyfert nuclei oriented in such a way that the angle i between the line of sight and the normal to the plane does not exceed 10°. In the catalog by Véron-Cetty and Véron (2003), the fraction of such nuclei (among those with redshifts $z < 0.01$) is ~0.15. However, the Seyfert nuclei identified as possible CR sources are oriented differently; the mean angle $i \approx 52°$. If these objects are actually CR sources, then they emit uncollimated beams of particles. UHECR particles can be emitted in an uncollimated way from an accretion disk in the model by Haswell *et al.* (1992). We adopt this model by assuming that CRs emerging from the source in a cone with an angle $\theta \approx 50°$ are detected on Earth.

At a given CR intensity near the Earth, the power of a source with emission in a solid angle Ω_S is a factor of $\Omega_S/(4\pi)$ lower than that of an isotropic source. For an angle $\theta \approx 50°$, the solid angle is $\Omega_S \approx 2$ and the UHECR beam power is $L_S^b \approx 2 \times 10^{39}$ erg s^{-1} if $I(E) \approx 10^{-39}$ (cm^2 s sr eV)$^{-1}$ and $L_S \approx 10^{40}$ erg s^{-1}. Assuming that the energy spectrum of the accelerated particles is a power law (Uryson 2004c) and, therefore, the overwhelming majority of particles have an energy $E_0 \approx 5 \times 10^{19}$ eV, we find that the source emits $N_S = L_S^b/E_0 \approx 2 \times 10^{31}$ particles s^{-1}. At distance R from the source, the beam particles cross the area $\pi R^2 \Omega_S$ and the particle flux in the solid angle Ω_S (the number of particles crossing a unit area perpendicular to the beam axis per unit time) is $N = L_S^b/(R^2 \Omega_S E_0)$ (this relationship is formally identical to the expression for the number of particles in a unit solid angle for isotropic emission $N = L_S/(4\pi R^2 E_0)$).

Let the source be at a distance of $R = 16$ Mpc. This is the distance at which the maximum in the spatial distribution of Seyfert nuclei with redshifts $z < 0.01$ from the catalog by Véron-Cetty and Véron (2001) is located for the Hubble constant $H = 75$ km Mpc^{-1} s^{-1}. On Earth, the particle flux from this source is $N \approx 4.3 \times 10^{-21}$ (cm^2 s)$^{-1}$ and arrays with areas $S \approx 10$, 100, and 3000 km^2 detect 0.012, 0.12, and ~4 particles per year, respectively. Hence, we find that no doublets of particles are detected from a single source on arrays with $S \sim 10$ km^2. On the AGASA array ($S \approx 100$ km^2), a doublet of particles from a single source can be detected in an observing time of $T > 10$ yr. On the Pierre Auger array ($S \sim 3000$ km^2), a cluster from a single source can be detected during a year of operation. In the section Discussion, we list the reasons why these estimates can be considerably lower.

Let us now determine the detection rate if the UHECR sources are BL Lac objects. In these objects, the jets are directed toward the observer (here, we do not touch on uniformity or nonuniformity of the CR intensity distribution in different regions of intergalactic space). Consider the possible values of the parameters that are necessary for our estimates by assuming that the particles are accelerated in the source in accordance with the model by Kardashev (1995).

In the model by Kardashev (1995), the power spent on UHECR emission is $L_{BL} = 1.5 \times 10^{12} L_\odot$, where $L_\odot$ is the solar luminosity. At $L_\odot \approx 3.86 \times 10^{45}$ erg s^{-1}, $L_{BL} \approx 6 \times 10^{45}$ erg s^{-1}. Since the particle in this model are accelerated by an electric field, we assume the original CR spectrum to be monoenergetic. The energy of the accelerated protons in the model reaches ~10^{20}–10^{21} eV (Kardashev 1995; Shatskiĭ and Kardashev 2002), in agreement with the maximum value of 10^{21} eV in the sources obtained by Aharonian *et al.* (2002) and Medvedev (2003) and with the estimate by Uryson (2004c). According to our estimates obtained by comparing the calculated and measured UHECR spectra (Uryson 2004c), the CR emission power is $L_{BL} \sim 10^{43}$–10^{44} erg s^{-1} (this quantity cannot be determined with a better accuracy because of the large measurement errors). The particles are emitted in a directed beam with an opening half-angle $\alpha \approx 7 \times 10^{-7}$ (Kardashev 1995).

The fraction of the particles that reached the array with energy $E \geq 4 \times 10^{19}$ eV depends on the distance of the source due to the CR energy losses in the interactions with background radiations in intergalactic space (Greisen 1966; Zatsepin and Kuz'min 1966).

In what follows, we assume that this fraction is 0.3, 0.5, 0.7, and 1 for distances $R \approx 800$, 700, 600 Mpc, and $R < 600$ Mpc, respectively. We will disregard the contribution from the sources at $R > 800$ Mpc (because of the low particle density, the contribution from these sources to the detected flux is an order of magnitude lower than the contribution from the sources at $R < 600$ Mpc even without including the CR energy losses in intergalactic space).

Assuming that the source has a redshift $z \approx 0.2$ (this is the redshift at which the maximum in the spatial distribution of BL Lac objects from the catalog by Veron-Cetty and Veron 2001 is located), i.e., is $R \approx 600$ Mpc away, we estimate the CR detection rate for the following sets of parameters.

(1) Assuming that $L_{\rm BL} \approx 6 \times 10^{45}$ erg s^{-1} is the power of the directed beam, we find for $E_0 = 10^{21}$ eV that an array with a relatively small area, $S \approx 10$ km^2, detects $\sim 10^8$ particles per year from a single source, in conflict with the measurements.

(2) For an isotropic CR emission power $L_{\rm BL} \approx 6 \times 10^{45}$ erg s^{-1} (the equivalent power of the directed beam is $L^b_{\rm BL} \approx 10^{33}$ erg s^{-1}) and a particle energy of $E_0 = 10^{21}$ eV, an array with an area $S \approx 100$ km^2 will detect 1.8 particles per year from a single source and a cluster of three or more particles in several years. On an array with $S \sim 10$ km^2, a doublet of particles can be detected in a time $T > 10$ yr.

(3) Finally, let us consider a set of parameters with an isotropic CR emission power of $L_{\rm BL} \sim 10^{44}$ erg/s (the equivalent power of the directed beam is $L^b_{\rm BL} \approx 1.6 \times 10^{31}$ erg s^{-1}) and a particle energy of $E_0 = 10^{21}$ eV. In this case, arrays with an area of 10, 100, and 3000 km^2 will detect 5×10^{-4}, 5×10^{-3}, and 0.15 particles per year, respectively, from a single source. In this model, at $L_{\rm BL} \leq 10^{44}$ erg s^{-1}, CR clusters from a single source can be detected only on an array with an area $S \sim 3000$ km^2 in a time $T > 10$ yr.

Below, we analyze the second and third sets of parameters and do not consider the first set, because it is in conflict with the experimental data. Let us turn to the AGASA data.

ANALYSIS OF THE CLUSTERS DETECTED ON THE AGASA ARRAY

UHECR particles whose arrival directions coincided within a single error, a total of five doublets and one triplet of 63 UHE particles, were detected on the AGASA array over 10 years (Hayashida *et al.* 2000). A particle detected on the Yakutsk array (Afanasiev *et al.* 1996) also falls into the triplet particle region. The detection rate of particles in clusters is $\sim$1–1.5 particles per year; in doublet C4 (according to the numbering of clusters from Hayashida *et al.* (2000)), the particles were detected with an interval of almost 10 years.

The UHECR particles most likely arrive from areas of the sky with an enhanced AGN density (Uryson 2001a). (The sources in the model with the second set of parameters, as shown above, constitute an exception.) If this is the case, then the particles that form a cluster also arrive from such areas. The size of these areas in equatorial coordinates is ($\Delta\alpha \lesssim 9^\circ$, $\Delta\delta \lesssim 9^\circ$). If we assume that the errors in the right ascension and declination are approximately 3°, then this is the region of a triple error in the determination of the particle arrival direction.

Let us test this assumption. Let us consider the AGNs near the arrival direction of the particles in each cluster and estimate the CR detection rate. The size of the neighborhood in which we will analyze the AGNs is ($\Delta\alpha \lesssim 9^\circ$, $\Delta\delta \lesssim 9^\circ$).

Seyfert nuclei with $z < 0.01$ fall into the search region of four clusters: C2, C3, C5, and C6. The search region of triplet C2 contains five nuclei from the catalog by Veron-Cetty and Veron (2001), eight objects from Veron-Cetty and Veron (2003), and ten nuclei from the catalog by Lipovetskiĭ *et al.* (1987). One object from the catalog by Lipovetskiĭ *et al.* (1987) and one object (Veron-Cetty and Veron 2001, 2003; Lipovetskiĭ *et al.* 1987) fall into the regions of doublet C3 and cluster C5, respectively. There are three, five, and four nuclei from the catalogs by Veron-Cetty and Veron (2001, 2003) and Lipovetskiĭ *et al.* (1987), respectively, in the region of doublet C6.

The UHECR flux from the Seyfert nuclei in the region of triplet C2 detected by an array with an area $S \approx 100$ km^2 is $\sim$0.6 particles per year, the flux in the region of doublets C3 and C5 is $\sim$0.03 particles per year, and the flux from the nuclei in the region of cluster C6 is $\sim$2 particles per year, as estimated from the data of the catalogs by Veron-Cetty and Veron (2003) or Lipovetskiĭ *et al.* (1987).

The fluxes of $\sim$0.03 particles per year are too low to explain the doublets of particles; the fluxes of $\sim$1 particles per year are enough for clusters to be detected on the AGASA array. Thus, the model with Seyfert nuclei explains the origin of two clusters.

BL Lac objects fall into the search regions of all the clusters, except doublet C4. Nearby Seyfert nuclei do not fall into the C4 search region either. This may be attributable to the low Galactic latitude of the particle arrival, $b \approx -10^\circ$, since this latitude corresponds to the "zone of avoidance" of galaxies in which relatively few objects are observed. The numbers of objects from the catalogs by Veron-Cetty and Veron (2001, 2003) that fall into the search regions are, respectively, 3 and

4 for doublet C1, 2 and 9 for triplet C2, 4 and 8 for cluster C3, 6 and 12 for doublet C5, and 8 and 13 for cluster C6.

Let us determine the UHECR flux from the BL Lac objects in the cluster region initially for the third set of parameters. (In our estimates, we disregarded the BL Lac objects with unknown redshifts.) An array with an area $S \approx 100$ km^2 will detect the following fluxes: $\sim$0.3, $\sim$0.4, $\sim$0.1, $\sim$0.6, and $\sim$0.45 particles per year in the regions of clusters C1, C2, C3, C5, and C6, respectively. The fluxes $\sim$0.3–0.6 particles per year are enough to explain the detected clusters of particles.

The fluxes calculated with the second set of parameters will be a factor of $\sim$50 higher. In this model, the clusters of particles are emitted by single sources.

DISCUSSION

The above fluxes may have been overestimated. The reasons are the following.

First, the fluxes were obtained by assuming that the array detects the emission from the sources during the entire period of its operation. In fact, the source position in the sky can depend on the time of the day and on the season. As a result, the actual time during which the source emission is detected by the array can be considerably shorter. For instance, if the sky area from which the cluster particles arrive falls into the array survey region $\sim$1/2 day during $\sim$1/2 year, then the detected CR flux from the sources will be a factor of 4 lower than the estimates obtained.

Second, the arrays usually select showers with polar angles of the arrival direction $\Theta < 30°$–$45°$; therefore, no more than half of the emission from a given source is detected. As a result, the estimated CR detection rate may be a factor of $\sim$2–10 higher than the measured values. For these reasons, although the second set of parameters in the BL Lac model yields a high CR flux, it is probably suitable for explaining the detected clusters.

In addition, the activity of BL Lac objects can be not constant, but quasi-periodic, with a period of from 4 to $\sim$25 yr with a relatively short duration of the active state (Pyatunina *et al.* 2005). If this is the case, then the clusters can be formed through the emission and the subsequent "turn-off" of a single source in the model with the second set of parameters. Further evidence for this picture is that BL Lac objects with intense emission are the most likely sources of UHECRs (Gorbunov *et al.* 2002). The relatively short flares of the CR sources are also consistent with the formation of clusters of particles by several sources in the model with the third set of parameters.

In addition, the CR emission may be affected by the content of protons (nuclei) in the jet plasma or in the region of the accretion disk where the particles are accelerated. According to Zheleznyakov and Koryagin (2002) and Koryagin (2004), the fraction of the protons in a jet can be $\sim$0.01–0.1. A change in the proton fraction in the particle acceleration region by several factors will lead to a change in the CR intensity also by several factors, and this will appear as the turn-on and turn-off of the UHECR source.

The turn-on and turn-off of the sources may be the reason why the AGASA array has detected only doublets, one triplet, and no clusters with a larger number of particles over 10 years of operation.

Let us now list the predictions of the model in which the particles are emitted by BL Lac objects with a maximum energy of 10^{27} eV (Kardashev 1995). For $L_{\rm BL} \approx 6 \times 10^{45}$ erg s^{-1}, the CR fluxes in it are too low: arrays with areas $S \sim 100$ and 1000 km^2 will detect no more than 10^{-7} and 10^{-6} particles per year, respectively, from the cluster region. If $L_{\rm BL} \approx 6 \times 10^{45}$ erg s^{-1} is the power of the directed beam, then the predicted fluxes are too high. Thus, for example, an array with $S \sim 10$ km^2 will detect $\sim 10^6$ particles per year from a single source, in conflict with the measurements. The model with such parameters does not describe the UHECR spectra measured on different arrays (Uryson 2004c) either.

It follows from this comparison that CR data can be a test for some of the theoretical estimates pertaining to AGNs.

CONCLUSIONS

The model in which the sources of UHECRs are AGNs can explain the origin of the particle clusters detected by AGASA. The clusters of particles arrive from areas of the sky with an enhanced density of these objects (the sizes of such sky areas in equatorial coordinates are $\Delta\alpha < 9°$, $\Delta\delta < 9°$), but can also be detected from individual sources. No clusters can be detected on arrays with an area $S \sim 10$ km^2.

If the UHECR sources are Seyfert nuclei, then a doublet of particles from a single Seyfert nucleus can be detected on an array with an area $S \approx 100$ km^2 in an observing time of $T > 10$ yr. On an array with $S \sim 3000$ km^2, a cluster can be detected in a year of its operation.

If UHECRs are emitted by BL Lac objects, then a cluster of particles can be produced by a single source with an emission power in the CR beam of $\sim 10^{33}$ erg s^{-1}. Doublets and triplets of particles from such single sources can be detected by an array with an area $S \approx 100$ km^2 in $\sim$2–4 yr. If the CR emission power is $\sim 2 \times 10^{31}$ erg s^{-1}, then the clusters of particles are emitted by a group of sources. Doublets and

triplets of particles will be detected by an array with an area $S \approx 100$ km^2 also in ~2–4 yr of its operation.

The CR emission and the cluster formation can be affected by the following factors. First, CRs are accelerated in the source quasi-periodically, with a period of from 4 to ~25 yr with a relatively short duration of the active state, which is possible, as suggested by the results of Pyatunina *et al.* (2005). Second, the UHECR particle emission may be affected by the changing (from ~0.01 to 0.1) fraction of the protons (nuclei) in the jet plasma or in the particle acceleration region. (Such a change in the proton fraction is consistent with the results of Zheleznyakov and Koryagin 2002.)

The variable activity of the sources and the decrease and increase in the proton fraction in a jet appear as the turn-on and turn-off of the source. This may be the reason why the AGASA array detected only doublets, one triplet, no clusters with a larger number of particles over 10 yr of its operation.

The estimates of the CR detection rate from which these conclusions were drawn have been obtained without allowance for the actual time during which the array detected the emission from the sources. In addition, we disregarded the selection of showers by the polar angle of their arrival, with the result that no more than half of the emission from the source may be detected. Therefore, a further study of clusters requires taking into account the actual time of shower detection and their selection by the polar angle of their arrival.

A comparison of the CR data with theoretical estimates can serve as a test for the models of AGNs, the UHECR sources.

ACKNOWLEDGMENTS

I am grateful to A.V. Zasov and V.V. Lidskiĭ for discussions and to the referees for remarks.

REFERENCES

1. B. N. Afanasiev, M. N. Dyakonov, V. P. Egorova, *et al.*, in *Proceedings of International Symposium "Extremely High Energy Cosmic Rays: Astrophysics and Future Observatories,"* Ed. by M. Nagano (Inst. Cosmic-Ray Res., Tokyo, 1996), p. 32.
2. F. A. Aharonian, A. A. Belyanin, E. V. Derishev, *et al.*, Phys. Rev. D **66**, 023 005 (2002).
3. V. S. Berezinskiĭ, S. V. Bulanov, V. L. Ginzburg, *et al.*, *Astrophysics of Cosmic Rays,* Ed. by V. L. Ginzburg (Nauka, Moscow, 1990) [in Russian].
4. E. V. Derishev, F. A. Aharonian, V. V. Kocharovsky, and Vl. V. Kocharovsky, Phys. Rev. D **68**, 043 003 (2003).
5. K. Dolag, D. Grasso, V. Springel, *et al.*, Pis'ma Zh. Éksp. Teor. Fiz. **79**, 719 (2004) [JETP Lett. **79**, 583 (2004)].
6. D. S. Gorbunov, P. G. Tinyakov, I. I. Tkachev, and S. V. Troitsky, Astrophys. J. Lett. **577**, L93 (2002).
7. K. Greisen, Phys. Rev. Lett. **16**, 748 (1966).
8. C. A. Haswell, T. Tajima, and J.-I. Sakai, Astrophys. J. **401**, 495 (1992).
9. N. Hayashida, K. Honda, N. Inoue, *et al.*, astro-ph/0008102 (2000).
10. N. S. Kardashev, Mon. Not. R. Astron. Soc. **276**, 515 (1995).
11. S. A. Koryagin, private communication (2004).
12. P. P. Kronberg, Rep. Prog. Phys. **57**, 325 (1994).
13. V. A. Lipovetskiĭ, S. N. Neizvestnyĭ, and O. M. Neizvestnaya, Soobshch. Spets. Astrofiz. Obs. **55** (1987).
14. M. V. Medvedev, Phys. Rev. E **67**, 045 401(R) (2003).
15. M. Nagano and A. Watson, Rev. Mod. Phys. **72**, 689 (2000).
16. T. B. Pyatunina, D. C. Gabuzda, S. G. Jorstad, *et al.*, astro-ph/0502173 (2005).
17. A. A. Shatskiĭ and N. S. Kardashev, Astron. Zh. **79**, 708 (2002) [Astron. Rep. **46**, 639 (2002)].
18. P. G. Tinyakov and I. I. Tkachev, Pis'ma Zh. Éksp. Teor. Fiz. **74**, 499 (2001) [JETP Lett. **74**, 445 (2001)].
19. A. V. Uryson, Pis'ma Zh. Éksp. Teor. Fiz. **64**, 71 (1996) [JETP Lett. **64**, 77 (1996)].
20. A. V. Uryson, Astron. Zh. **78**, 686 (2001a) [Astron. Rep. **45**, 591 (2001a)].
21. A. V. Uryson, Pis'ma Astron. Zh. **27**, 901 (2001b) [Astron. Lett. **27**, 775 (2001b)].
22. A. V. Uryson, Astron. Astrophys. Trans. **23**, 43 (2004a).
23. A. V. Uryson, Astron. Zh. **81**, 99 (2004b) [Astron. Rep. **48**, 81 (2004b)].
24. A. V. Uryson, Pis'ma Astron. Zh. **30**, 897 (2004c) [Astron. Lett. **30**, 816 (2004c)].
25. M.-P. Veron-Cetty and P. Veron, Astron. Astrophys. **374**, 92 (2001).
26. M.-P. Veron-Cetty and P. Veron, http://www.obs-hp.fr (2003).
27. G. T. Zatsepin and V. A. Kuz'min, Pis'ma Zh. Éksp. Teor. Fiz. **4**, 114 (1966) [JETP Lett. **4**, 78 (1966)].
28. V. V. Zheleznyakov and S. A. Koryagin, Pis'ma Astron. Zh. **28**, 809 (2002) [Astron. Lett. **28**, 727 (2002)].

Translated by G. Rudnitskiĭ

Astronomy Letters, Vol. 31, No. 11, 2005, pp. 760–766. Translated from Pis'ma v Astronomicheskiĭ Zhurnal, Vol. 31, No. 11, 2005, pp. 853–859.

Long-Term Monitoring of the Long-Period Variable Y Cassiopeiae in the 1.35-cm Water-Vapor Line

G. M. Rudnitskiĭ* **and M. I. Pashchenko**

Sternberg Astronomical Institute, Universitetskiĭ pr. 13, Moscow, 119992 Russia

Received May 5, 2005

Abstract—Observations of the circumstellar maser emission from the long-period variable star Y Cas in the 1.35-cm water-vapor line are presented. The observations were performed with the RT-22 radio telescope at the Pushchino Radio Astronomy Observatory (Astrospace Center, Lebedev Physical Institute, Russian Academy of Sciences) in the period 1982–2005. The variations in the integrated flux $F_{\rm int}$ in the H_2O line correlate with the visual light curve of the star. The phase delay $\Delta\varphi$ between the $F_{\rm int}$ variations and the light curve is $0.2–0.4P$ (P is the period of the star). The H_2O maser Y Cas belongs to transient sources: peaks of high maser activity alternate with intervals of a low emission level when the H_2O-line flux does not exceed $(0.1–0.5) \times 10^{-20}$ W m^{-2}. A "superperiod" of ~5.7 yr was found in the occurrence of activity peaks. A particularly strong maximum of maser radio emission took place at the end of 1997, when the flux $F_{\rm int}$ reached 15.6×10^{-20} W m^{-2}. A model for the H_2O maser variability in Y Cas is discussed. The variability is caused by a periodic action of shock waves driven by stellar pulsations. The H_2O maser flares may be associated with short-lived episodes of enhanced mass loss by the star or with the propagation of a particularly strong shock wave when a planet orbiting the star passes through its periastron. © *2005 Pleiades Publishing, Inc.*

Key words: *late-type stars, long-period variable stars, circumstellar envelopes, maser radio sources.*

INTRODUCTION

More than 500 late-type variable giant and supergiant stars, which are sources of maser radio emission in the $6_{16}–5_{23}$ rotational line of the ortho-H_2O molecule ($\nu = 22.235$ GHz), are known to date (Benson *et al.* 1990; Palagi *et al.* 1993). All these stars belong to long-period Mira Ceti variables or semiregular Sra and SRb variables. The H_2O radio emission from the stars is highly variable. Occasionally, the flux density in the 1.35-cm line changes by several orders of magnitude. Comparing the H_2O line and optical variations in the stars is of considerable interest from the viewpoint of long-term observations. A correlation between the H_2O line and optical variability curves, as well as a study of the accompanying variations in the structure of the H_2O line profile, characterize the processes that take place in the inner layers of the circumstellar envelopes around AGB stars, to which the variables under consideration belong.

This paper continues a series of publications (Berulis *et al.* 1983; Rudnitskiĭ *et al.* 1999; Rudnitskij *et al.*, 2000; Pashchenko and Rudnitskiĭ 2004; and references therein) on the study of H_2O maser variability in long-period variable stars. We present the results of our observations of the star Y Cas performed from 1982 until 2005.

In the fourth edition of the *General Catalog of Variable Stars* (GCVS) (Kholopov *et al.* 1985), Y Cas is classified as a Mira Ceti long-period variable. Its light elements in the GCVS are

$$\text{Max JD} = 2444506 + 413^{\rm d}.48E. \qquad (1)$$

The visual magnitude range is $8.7–15^{m}.3$, the spectral type changes from M6e to M8.5e, and the distance to the star is variously estimated to be in the range from 506 (Spencer *et al.* 1981) to 780 pc (González-Alfonso *et al.* 1998). The star Y Cas is a well-known source of maser emission in the molecular lines of OH (Kolena and Pataki 1977), H_2O (Dickinson 1976), and SiO (Dickinson *et al.* 1978) as well as of thermal radio emission of the CO molecule (González-Alfonso *et al.* 1998). The radial velocity of the star was found from the thermal molecular radio emission to be $V_* = -16.9$ km s^{-1}. The star's mass loss rate is $\dot{M} \sim (3–10) \times 10^{-7} M_\odot$ yr^{-1} (Bowers and Johnston 1994; González-Alfonso *et al.* 1998).

OBSERVATIONS

The long-term monitoring of Y Cas in the H_2O line was performed with the RT-22 radio telescope at

*E-mail: gmr@sai.msu.ru

Published data on the observations of the H_2O maser emission in Y Cas

Date	F_{peak}, Jy	V_{LSR}, km s^{-1}	FWHM, km s^{-1}	F_{int}, 10^{-20} W m^{-2}	Reference
August 5, 1974	4	−17*	2.4	0.81	Dickinson (1976)
September 7–10, 1976	<9	–	–	–	Spencer *et al.* (1979)
November 28, 1976	3	-17.3	2.8	0.64	Olnon *et al.* (1980)
September 8, 1988	19.9	-18.9	2.4	2.47	Palagi *et al.* (1993)
December 12–13, 1988	33	-18.32	1.3	3.60	Bowers and Johnston (1994)**
May 10–11, 1991	4.6	-18.4	2.8	1.08	Takaba *et al.* (1994)
March 26, 1995	–	–	–	1.23	Szymczak and Le Squeren (1999)

* Table 1 in Dickinson (1976) gives an erroneous radial velocity of +2.4 km s^{-1} instead of −17 km s^{-1}.

** The VLA inteferometric map of the H_2O maser Y Cas.

the Radio Astronomy Observatory (Astrospace Center, Lebedev Physical Institute, Russian Academy of Sciences) in Pushchino (Moscow oblast). The receiving equipment included a liquid-helium-cooled 22-GHz band maser amplifier (with a system noise temperature of $T_N = 200$–300 K). In the 1993–2005 observations, we used a cooled 22-GHz band FET amplifier (with a system noise temperature of $T_N = 80$–120 K). For the spectral analysis, we used a 128-channel filter-bank spectrometer designed and produced at the Sternberg Astronomical Institute with a frequency resolution of 7.5 kHz (0.101 km s^{-1} in radial velocity at the H_2O line frequency). The absorption in the Earth's atmosphere was taken into account using a technique described by Rudnitskiĭ *et al.* (1999). The flux density sensitivity in different observing sessions ranged from 5 to 20 Jy. A total of 112 observing sessions were carried out for Y Cas over 23 years (from February 11, 1982, through March 15, 2005).

Figure 1 presents the results of our observations in the form of spectral H_2O line profiles. The scale on the vertical axis is in units of flux density F_ν (janskys). The radial velocity with respect to the Local Standard of Rest (V_{LSR}, km s^{-1}) is along the horizontal axis. This figure shows mainly the spectra that exhibit detectable emission and some of the profiles where the emission level is below the noise level.

In Fig. 2b, the integrated flux F_{int} of the H_2O maser emission in the H_2O line profile is plotted against time. The errors of $F_{int}(H_2O)$ in Fig. 2b were estimated from the noise dispersion σ in the spectral channels; these are small, and their limits are smaller than the symbol size on the plot in most cases. As upper limits for F_{int}, we took the fluxes of a Gaussian feature with a 3σ amplitude and a full width at half maximum (FWHM) of 2.5 km s^{-1} (a typical width of the spectral feature in the cases where the emission was detected). The typical upper limits on F_{int} are $(0.1$–$0.5) \times 10^{-20}$ W m^{-2}.

For comparison, Fig. 2a shows the visual light curve of Y Cas. We used the data of long-term visual observations of Y Cas from the French Association of Variable Star Observers (AFOEV)[1] and the American Association of Variable Star Observers (AAVSO)[2] retrieved via the Internet. Our FFT analysis of the entire light curve in Fig. 2a revealed a period of $P_0 = 413^d.9 \pm 0^d.5$ (Fig. 3), in agreement with the GCVS value. The diamonds in the upper part of Fig. 2a denote the epochs of maxima calculated with light elements (1), and the vertical straight lines indicate the epochs of actual maxima. We see from the figure that elements (1) are, on average, conserved throughout the interval 1980–2005. However, the actual maxima preceded the calculated ones in 1989–1994 and lagged behind these in 2003–2004.

DISCUSSION

The H_2O maser Y Cas is among the poorly studied masers. Prior to our work, no dedicated monitoring of the 22.235-GHz H_2O maser variability in Y Cas had been carried out. The H_2O line emission in Y Cas was first observed by Dickinson (1976) on August 5, 1974. Subsequently, Y Cas was observed in the H_2O line occasionally. The table lists the observational data of other authors. Its columns contain the following:

[1] ftp://cdsarc.u-strasbg.fr/pub/afoev/.

[2] http://www.aavso.org/.

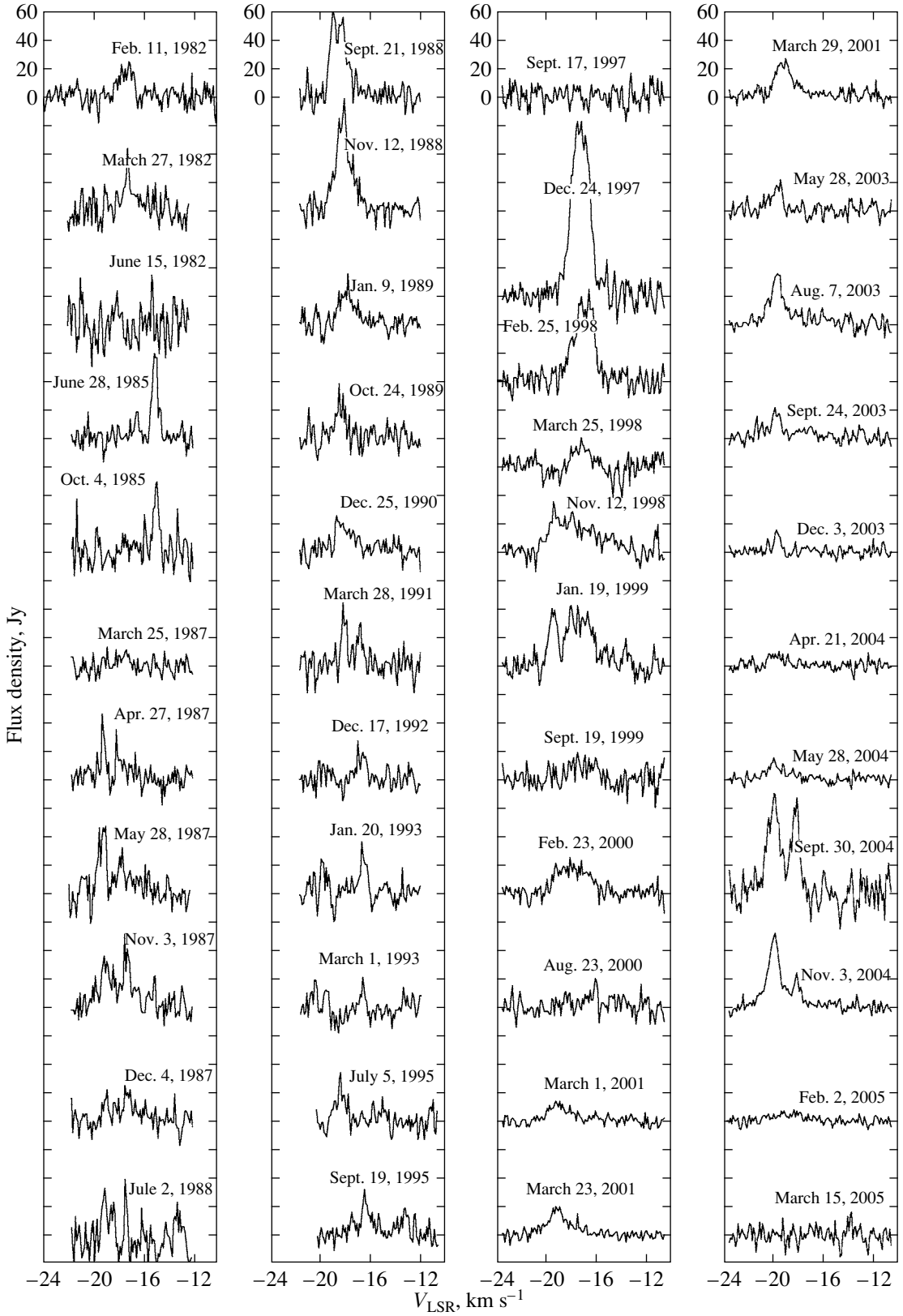

Fig. 1. Profiles of the H_2O maser emission line in the star Y Cas.

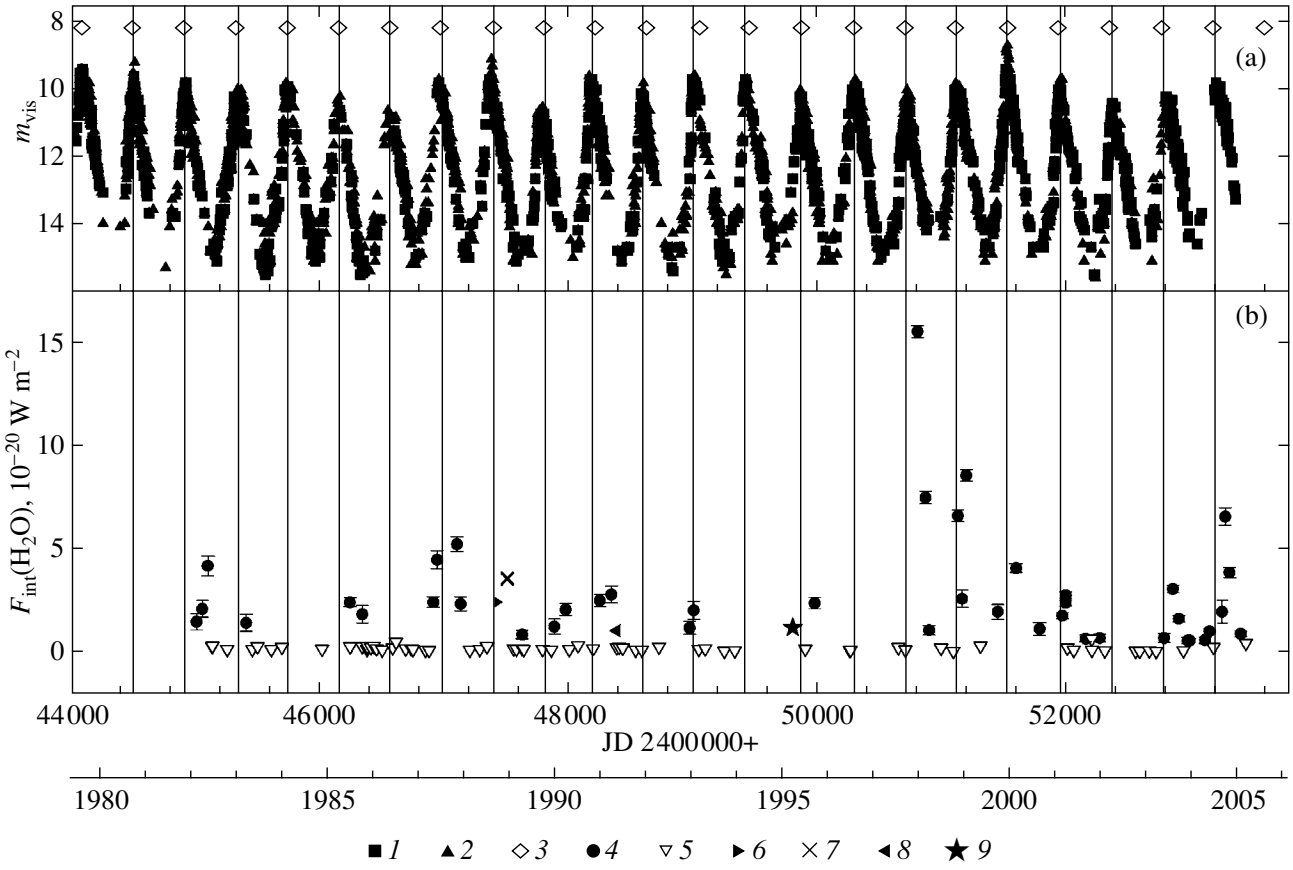

Fig. 2. (a) Visual light curve of Y Cas: *1*, AFOEV data; *2*, AAVSO data; *3*, epochs of visual maxima calculated with GCVS light elements (1). The vertical straight lines mark the epochs of the actual light maxima. (b) Integrated H_2O line flux: *4*, our data for the radial-velocity range $-21 \ldots -14$ km s^{-1}; *5*, upper limits on the line flux; the data of other authors are also shown: *6*, Palagi *et al.* (1993); *7*, Bowers and Johnston (1994); *8*, Takaba *et al.* (1995); *9*, Szymczak and Le Squeren (1999).

dates of observations, peak flux densities, peak radial velocities, line full widths at half maximum, integrated line fluxes, and references. These results are indicated by different symbols in Fig. 2b. For the measurements at epochs close to our observations, the fluxes obtained in other papers agree with our data.

The work by Bowers and Johnston (1994), the only one in which the H_2O maser Y Cas was observed interferometrically, should be noted. The H_2O maser Y Cas was mapped on VLA on December 12–13, 1988. The map exhibits features with radial velocities in the range $V_{LSR} = -20.9 \ldots -15.4$ km s^{-1}. The distribution of the spectral features is elongated in the east–west direction. Most of the features at radial velocities lower than the stellar velocity ($V_* = -16.9$ km s^{-1}) are located in the eastern part of the map. A possible explanation is that the maser is localized in a bipolar outflow from the star. The total extent of the masering region in the map is $\sim$50 ms. At a distance of $d = 500$–780 pc (see the Introduction), this corresponds to a linear size of the maser $\sim (3.7$–$6.0) \times 10^{14}$ cm. The group of features at $V_{LSR} = -18.6 \ldots -17.0$ km s^{-1}, which mainly contribute to the H_2O line profile, is located within 10 ms east of the stellar position in the map, i.e., at a projected distance of $\sim(0.7$–$1.2) \times 10^{14}$ cm. The features have negative velocities with respect to the stellar center-of-mass velocity $V_* = -16.9$ km s^{-1}. These features are probably localized in the approaching jet of the bipolar outflow.

In addition to the 6_{16}–5_{23} line at 22.235 GHz, another water-vapor maser line was observed in Y Cas. González-Alfonso *et al.* (1998) detected maser emission from Y Cas in the 3_{13}–2_{20} line of para-H_2O at 183.31 GHz. The radial velocity of the peak in the 183-GHz line, like that of the 22-GHz line, is blueshifted with respect to V_*, i.e., the region of the main emission from the 183-GHz maser is also located in the approaching jet.

Our regular 23-year-long observations revealed that the H_2O maser Y Cas is a typical transient with

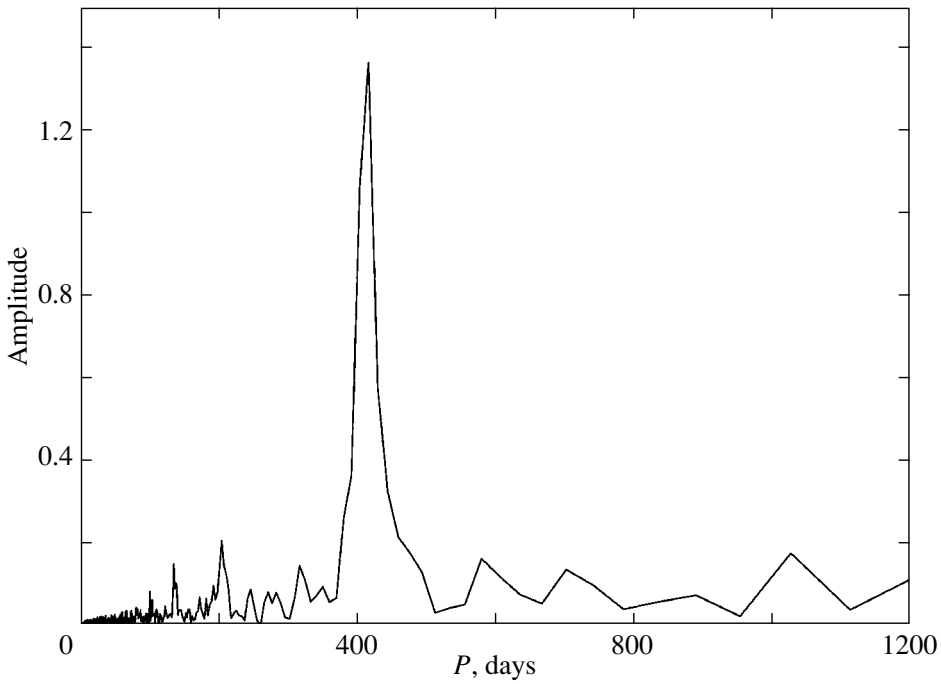

Fig. 3. FFT periodogram of the light curve (Fig. 2a). The peak corresponds to the period $P_0 = 413\overset{d}{.}9 \pm 0\overset{d}{.}5$. The harmonics at $P = P_0/2$, $P_0/3$, and $P_0/4$ are seen.

jumps in the H_2O line flux reaching two orders of magnitude. In this respect, the star Y Cas is similar to R Cas, which was discussed previously (Pashchenko and Rudnitskiĭ 2004). In both stars, intervals of high maser activity alternate with intervals of a low emission level, when the H_2O maser is inaccessible to observation on RT-22.

In the history of our H_2O line observations of Y Cas, we can distinguish four periods of enhanced maser activity when $F_{\rm int}$ reached $(4–5) \times 10^{-20}$ W m^{-2} or more: 1982–early 1983, 1987–1991, late 1997–early 2001, and 2003–2005. In these intervals, when the maser emission was detectable in our observations, $F_{\rm int}(H_2O)$ correlated with the visual light curve of Y Cas: the maximum of $F_{\rm int}(H_2O)$ occurs shortly after the visual maximum of the star with a phase delay of $\Delta\varphi \sim 0.2P$ or occasionally more, up to $0.4P$, as at the maximum of 1982.

A periodicity of the epochs of enhanced H_2O line flux is evident. The sharp maximum of $F_{\rm int}$ at the end of 1997, when the peak flux density at $V_{\rm LSR} = -17.4$ km s^{-1} reached 122 Jy and $F_{\rm int}$ was 15.6×10^{-20} W m^{-2}, is particularly prominent. Higher than average maxima of $F_{\rm int}$ were in 1982, 1987, and 2004. If enhanced maser activity took place in 1994–1995, the maser activity superperiod can be estimated as ~5.7 yr. However, in the interval JD = 2449337–2449904, our data are lacking. There is only a single observation by Szymczak and Le Squeren (1999) denoted in Fig. 2b by an asterisk; in this case, the flux is low ($F_{\rm int} = 1.23 \times 10^{-20}$ W m^{-2}). Low fluxes were recorded in 1976 (see the table), i.e., six years before the beginning of our observations, when a maximum of maser activity could also occur.

Such a violation of the presumed "superperiodicity" in the behavior of the maser may be due to the missing of individual "supermaxima." We noted a similar behavior in our monitoring of the H_2O maser W Hya (Rudnitskiĭ *et al.* 1999). The causes of the correlation between the H_2O maser emission and the visual light curve and the missing of individual maxima are discussed in detail in our previous papers (Rudnitskiĭ and Chuprikov 1990; Rudnitskij 1997; Rudnitskij *et al.* 2000). The main hypothesis adopted in these papers is that the H_2O masering region is located at a distance of $\sim 10^{14}$ cm from the stellar center, in a quasi-stationary layer (QSL) of the material lost by the star. The H_2O maser pumping is maintained by pulsation-driven shock waves. Circumstellar dust plays an important role in the pumping mechanism. Periodic heating of dust grains by variable infrared radiation from the star results in a correlation between $F_{\rm int}(H_2O)$ and the infrared brightness of the star. The near-infrared light curves of Mira variables are known to have a delay $\Delta\varphi \sim 0.2–0.3P$ with respect to the visual light curves (Lockwood

and Wing 1971). Thus, the delay of $F_{\rm int}(H_2O)$ with respect to the visual light curve can be explained.

During our monitoring of the maser Y Cas, we recorded cases of particularly strong variability of the H_2O emission. The most dramatic example is an increase in $F_{\rm int}(H_2O)$ from a value $<0.14 \times 10^{-20}$ W m^{-2} on September 17, 1997, to an absolute maximum over the entire period of our observations, 15.6×10^{-20} W m^{-2} on December 24, 1997. During March 2001, the flux rose by a factor of 1.5; in two days (from March 27 through March 29), the flux increased by 15%.

The maser variability "superperiod" ($\sim$5.7 yr) may be caused by periodic QSL formation and destruction, because the mass loss by the star probably proceeds not at a constant rate $\dot{M}$, but in the form of isolated episodes, in the case under consideration, every six years. The relative irregularity of the mass loss process may be responsible for the missing of some episodes and, as a consequence, for the absence of expected high maxima of $F_{\rm int}(H_2O)$. The asymmetry of the interferometric map of the H_2O maser Y Cas (Bowers and Johnston 1994) suggests that the mass loss by the star is not spherically symmetric. This is also evidenced by the change in the H_2O line profile with time. In general, the main emission took place at velocities $V_{\rm LSR} = -18 \ldots -17$ km s^{-1} close to V_*. However, in several cases, emission features appeared at more negative velocities, $V_{\rm LSR} \sim -20 \ldots -18$ km s^{-1} (the 1987–1988 and 2001–2004 profiles, Fig. 1) and at more positive velocities, $V_{\rm LSR} \sim -15$ km s^{-1} (1985). In 1987, 1991, and 2004, the line profile exhibited a double structure. Occasionally, the emission occupied the entire range $V_{\rm LSR} = -20 \ldots -16$ km s^{-1} (1998–1999).

Another possible cause of the superperiodicity of the H_2O maser emission in Mira variables was discussed by Rudnitskij (2002). If the star has a planet in an orbit with an appreciable eccentricity and an appropriate revolution period (in the case under consideration, $\sim$5.7 yr), then a strong shock wave emerges near the orbital periastron, when the planet enters the denser layers of the circumstellar envelope. This causes the intensity of the maser emission to rise. During our monitoring, we also found superperiods in other Mira variables, in particular, U Ori, in which the superperiod (revealed by the variation in the phase delay $\Delta\varphi$) is $\sim$9 yr (Rudnitskij *et al.* 2000).

CONCLUSIONS

We have obtained the profiles of the 1.35-cm H_2O maser emission line of the Mira variable Y Cas for 1982–2005. The H_2O maser emission correlated with the visual light curve of the star; there was a phase delay $\Delta\varphi \sim 0.2$–$0.4P$ ($P = 414^{\rm d}$ is the period of the star) between the $F_{\rm int}(H_2O)$ variations and the optical light curve. We found a possible maser variation superperiod of $\sim$5.7 yr. We adopted a model for the H_2O maser excitation by shock waves driven by stellar pulsations (Rudnitskiĭ and Chuprikov 1990; Rudnitskij 1997). According to the model, the masering H_2O molecules concentrate in a quasi-stationary layer of material, a local density enhancement in the circumstellar envelope. The QSL can periodically appear in episodes of enhanced mass loss by the star and then disappear for some time. The weakening of the maser emission may be associated with the temporary absence of the QSL. An alternative explanation is a periodic action on the H_2O masering region from a planet revolving around Y Cas in an eccentric orbit with a period of $\sim$5.7 yr (Rudnitskij 2002).

ACKNOWLEDGMENTS

We are grateful to E.E. Lekht, V.A. Samodurov, I.A. Subaev, and A.M. Tolmachev for help with the observations. We used the visual observations of the American Association of Variable Star Observers (AAVSO) and the Association Française des Observateurs d'Étoiles Variables (AFOEV).

REFERENCES

1. P. J. Benson, I. R. Little-Marenin, T. C. Woods, *et al.*, Astrophys. J., Suppl. Ser. **74**, 911 (1990).
2. P. F. Bowers and K. J. Johnston, Astrophys. J., Suppl. Ser. **92**, 189 (1994).
3. I. I. Berulis, E. E. Lekht, M. I. Pashchenko, and G. M. Rudnitskiĭ, Astron. Zh. **60**, 310 (1983) [Sov. Astron. **27**, 179 (1983)].
4. D. F. Dickinson, Astrophys. J., Suppl. Ser. **30**, 259 (1976).
5. D. F. Dickinson, L. E. Snyder, L. W. Brown, and D. Buhl, Astron. J. **83**, 36 (1978).
6. E. González-Alfonso, J. Cernicharo, J. Alcolea, and M. A. Orlandi, Astron. Astrophys. **334**, 1016 (1998).
7. P. N. Kholopov, N. N. Samus', V. P. Goranskiĭ, *et al.*, *General Catalog of Variable Stars* (Nauka, Moscow, 1985), Vol. 1.
8. J. Kolena and L. Pataki, Astron. J. **82**, 150 (1977).
9. G. W. Lockwood and R. F. Wing, Astrophys. J. **169**, 63 (1971).
10. F. M. Olnon, A. Winnberg, H. E. Matthews, and G. V. Schultz, Astron. Astrophys., Suppl. Ser. **42**, 119 (1980).
11. F. Palagi, R. Cesaroni, G. Comoretto, *et al.*, Astron. Astrophys., Suppl. Ser. **101**, 153 (1993).
12. M. I. Pashchenko and G. M. Rudnitskiĭ, Astron. Zh. **81**, 418 (2004) [Astron. Rep. **48**, 380 (2004)].

13. G. M. Rudnitskij, Astrophys. Space Sci. **251**, 259 (1997).
14. G. M. Rudnitskij, Publ. Astron. Soc. Aust. **19**, 499 (2002).
15. G. M. Rudnitskiĭ and A. A. Chuprikov, Astron. Zh. **67**, 293 (1990) [Sov. Astron. **34**, 147 (1990)].
16. G. M. Rudnitskiĭ, E. E. Lekht, and I. I. Berulis, Pis'ma Astron. Zh. **25**, 467 (1999) [Astron. Lett. **25**, 398 (1999)].
17. G. M. Rudnitskij, E. E. Lekht, J. E. Mendoza-Torres, *et al.*, Astron. Astrophys., Suppl. Ser. **146**, 385 (2000).
18. J. H. Spencer, K. J. Johnston, J. M. Moran, *et al.*, Astrophys. J. **230**, 449 (1979).
19. J. H. Spencer, A. Winnberg, F. M. Olnon, *et al.*, Astron. J. **86**, 392 (1981).
20. M. Szymczak and A. M. Le Squeren, Mon. Not. R. Astron. Soc. **304**, 415 (1999).
21. H. Takaba, N. Ukita, T. Miyaji, and M. Miyoshi, Publ. Astron. Soc. Jpn. **46**, 629 (1994).

Translated by G. Rudnitskiĭ

Astronomy Letters, Vol. 31, No. 11, 2005, pp. 767–785. Translated from Pis'ma v Astronomicheskiĭ Zhurnal, Vol. 31, No. 11, 2005, pp. 860–820.

Resolved Images of an Unknown Sector on the Surface of Mercury

L. V. Ksanfomality*

Space Research Institute, Russian Academy of Sciences, Profsoyuznaya ul. 84/32, Moscow, 117810 Russia

Received May 11, 2005

Abstract—We took electronic photographs of Mercury on the side of the planet that was not photographed from the *Mariner-10* spacecraft in 1973–1975 by the millisecond-exposure method in ground-based observations. Based on these photographs, we synthesized resolved images of the surface of unknown regions of the planet. The capabilities of the method are limited by the small angular size of the planetary disk (only 7.3 arcsec at average quadrature), specific difficulties of Mercury's ground-based observations, their very limited duration, and the laboriousness of the subsequent computer-aided observational data processing. The millisecond-exposure method is complex, but a sufficient number of primary electronic photographs can be taken under good seeing conditions for the subsequent synthesis of Mercurian images with a resolution of no worse than the diffraction limit. A giant basin about 2000 km in diameter and other large structures are distinguished in the synthesized images of the planet. In the regions where radar data are available, these structures can be identified with previously found ones. In some measure, the synthesized images allow the relief of the longitude sector 210°–290° W to be reconstructed on Mercury. It can be asserted with caution that the large relief features are distributed asymmetrically over the surface of Mercury, much as observed on other terrestrial planets, the Moon, and many satellites of giant planets.

Key words: *Solar system, Mercury, speckles, short exposures.*

1. INTRODUCTION

The well-known short-exposure method in observations of close multiple astronomical objects allows one to obtain fragmented images (speckles) the processing of which increases significantly the resolution. A lesser known fact is that a resolution that has previously been deemed unattainable can also be achieved by this method in observations of planets. Here, we present the results of our observations of Mercury performed with very short exposures. Mercury's observations with millisecond exposures were begun in 1999 at the Abastumani Observatory, the Republic of Georgia. Our old studies of the frequency spectrum of scintillations and image jitter (Ksanfomality 1966; Ksanfomality and Shakhovskoĭ 1967) and a work by Fried (1978) underlie the idea of short exposures. These publications clearly pointed out that reducing the exposure could increase the resolution of the images of astronomical objects. A resolution close to the diffraction limit ($1.22\lambda/D$), which for an instrument, say, with a diameter of $D = 1.5$ m at a wavelength of $\lambda = 600$ nm is 0.12 arcsec, can be achieved in principle. At the same time, the typical resolution for a 1.5-m reflector is rarely better than 1–1.3 arcsec since it is limited by atmospheric turbulence (seeing). Thus, obtaining resolved images of the Mercurian surface, whose diameter at quadrature is, on average, only 7.3 arcsec, seems unfeasible at first glance and is limited to images of four to six lines. In addition, the actual sensitivity of photographic materials was too low to reduce the exposures to a few milliseconds. Only with the advent of CCD detectors with their high quantum yield (and, of course, with the selection of good photographs) were we able to return to this problem in 1999, when the very first test image synthesized from several electronic photographs of Mercury immediately indicated that the synthesis method is promising (Ksanfomality *et al.* 2001). At this time, J. Warell had been taking single CCD photographs of Mercury with moderately short exposures for several years (Warell and Limaye 2001). The observations of Mercury published by the teams of Dantowitz *et al.* (2000) and Baumgardner *et al.* (2000) were also performed with short exposures and the subsequent processing of large data sets. Previously, Fried (1978) published his analysis of the gain that a reduction in exposures could give. The short-exposure method differs fundamentally from the standard adaptive optics technique in that it uses the brief moments of calmness of the atmosphere. Reducing the exposure does not remove the distortions produced by atmospheric lens irregularities, but decreases significantly the image blurring. Having accumulated a consid-

*E-mail: ksanf@iki.rssi.ru

erable number of photographs, we can then choose photographs with small distortions from these suitable for further processing and for synthesizing images.

THE TOPICALITY OF MERCURIAN STUDIES

At the beginning of the 21st century, Mercury remains one of the least studied planets (Grard and Balogh 2001; Ksanfomality 2001; Strom and Sprague 2003). There are several reasons why studies of Mercury are topical. We will name some of these. There exists the cosmogonic paradox of the presence of the planet in a zone where the known accretion models cannot explain the formation of a planetary body, because the orbital velocities of the protoplanetary material are too high. Nevertheless, the models of the planet based on the observed FeO abundance suggest that Mercury was formed from planetesimals that emerged precisely near the current position of the planet (Robinson and Taylor 2001). Mercury is an unusual, iron planet with an Fe/Si ratio that is a factor of 5 larger than the Earth's one. Mercury has the highest mean density in the Solar system (5.43 g cm^{-3}), which is almost equal to the Earth's one (5.52 g cm^{-3}); the so-called "liberated" density of Mercury (5.30 g cm^{-3}) is considerably higher than the Earth's one (4.10 g cm^{-3}). The ratio of the core and surface radii (0.8) is the largest among the terrestrial planets, while the dimensionless moment of inertia (0.324) is the lowest. The regolith of Mercury, devoid of an atmosphere, is constantly exposed to cosmic factors and substantial thermal cycling (Ksanfomality 2001). The unique mechanism of direct interaction of the solar wind with the surface of an atmosphereless planet close to the Sun acts only on Mercury. While the sizes of Mercury and the Earth differ by a factor of 3, the magnetosphere of the latter is smaller than the Earth's by approximately a factor of 18. The interaction of the solar wind with the planet is determined precisely by the properties of its magnetosphere, which differs significantly from the Earth's. In the orbit of Mercury, both the interplanetary magnetic field and the solar-wind density are a factor of 4–9 higher than those in the Earth's orbit. There is virtually no ionosphere, which leads to an unusual interaction of the magnetosphere with the fluxes of photoelectrons emitted from the day side of the planet, with the Na, K, and even Ca atoms in the exosphere (Sarantos *et al.* 2001; Killen *et al.* 2005), and with the interplanetary plasma perturbed by the motion of Mercury (Burlaga 2001). The presence of a detectable magnetic field whose origin also causes ambiguous explanations (Connerney and Ness 1988; Ness 1978; Russel *et al.* 1988; Ksanfomality 1998) remains unique for a small body. The relief of the planet has features typical of Mercury alone (see, e.g., Trask and Guest 1975). At the beginning of the 21st century, the relief of more than half of the planetary surface remains unknown. *Mariner-10* still remains the only accomplished mission to Mercury (1973–1975). Since the *Mariner-10* spacecraft was above the same sunlit hemisphere of Mercury in all three flybys of the planet, the part of the planet, including the edge zones, that was photographed by Mariner 10 accounts for only 46% of its area (Grard and Balogh 2001). The photographed surface resembles in relief the lunar highland regions (Head III 1981); no lunar-type maria were found on this side of the planet.

The interest of researchers in the relief of the unknown part of Mercury is also associated with new missions to the planet. The NASA *Messenger mission* (the spacecraft was launched in 2004) and the *BepiColombo* project in preparation (ESA, the launch is scheduled for 2011) need much input data, including information about the surface of Mercury. Unfortunately, the angular distance of Mercury from the Sun in ground-based observations is always small; therefore, the administrators of observatories are reluctant to use large telescopes to observe Mercury, since there is a risk that the instrumentation of the telescope could be damaged by direct solar rays. Nevertheless, ground-based observations of Mercury by "classical" methods (without using short exposures) have been performed by many researchers. A detailed list of such works can be found, for example, in a paper by Warell and Limaye (2001). In comparison with the observations of other bodies in the Solar System, observations of Mercury at ground-based observatories are also subject to other restrictions. Since the greatest elongation of the planet does not exceed 28° (typically, no more than 22°), observations of it are performed in astronomical twilight or even against the daytime sky background. More or less productive observations of Mercury are possible only at low-latitude mountain observatories. The near-infrared range is commonly used to increase the signal-to-noise ratio, since the brightness of the clear sky decreases as λ^{-4}. The observing time in twilight rarely exceeds 20–30 min; the planet is low above the horizon when the large air mass ($\sec z$) complicates the problem still further. However, as we show below, resolved images of the planet can still be obtained by ground-based technical and analytical means at the limit of technical capabilities.

In this paper, we synthesize images of Mercury. Our series of observations was performed at various observatories, but always by the short-exposure method. At the Abastumani Astrophysical Observatory, the Republic of Georgia (42°50′ E, 41°45′ N),

the observations were carried out in December 1999 and November 2001 at morning elongation of the planet. The observations at the Skinakas Astrophysical Observatory of the Heraklion University (Crete, Greece, 35°13′ E, 24°54′ N) were performed in May and September 2002 at evening elongation. In December 2003, the observations were carried out at evening elongation at the Mount Bigelow Observatory (110°44′ W, 32°25′ N) of the Arizona University (United States). In August 2003 and July 2004, the observations were performed at the Terskol Peak Observatory (Kabardino-Balkaria, Russia, 42°30′ E, 43°16′ N) also at evening elongation. The results presented below are based on the processing of several series of observations of Mercury at the Skinakas and Abastumani Observatories.

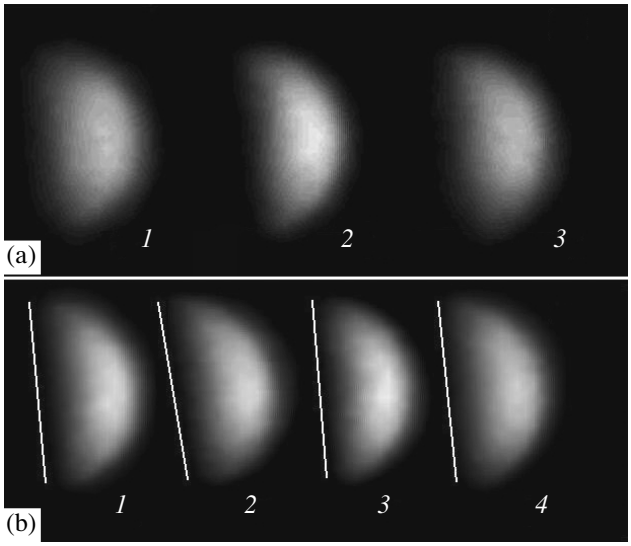

Fig. 1. (a) Rapid changes in image quality. Image *2* is sharp; images *1* and *3* are blurred. The intervals between images *1–2* and *2–3* are 99 ms each, and the exposures are 1 ms each. (b) Rotation of the sequential images in the plane of the sky. The exposures are 1 ms each.

ADVANTAGES OF THE SHORT-EXPOSURE METHOD IN OBSERVATIONS OF PLANETS

The resolution of astronomical images is limited mainly by atmospheric turbulence (seeing). The resolution depends on the place of observations, the time of the day, the aerosol density, and, of course, the zenith distance of the object (the air mass sec z). According to our observations (Ksanfomality 2003), the characteristic time in which the instantaneous optical properties of the atmosphere can change is rarely shorter than 30 ms. Therefore, for the instantaneous clearings of the atmosphere to be used, the exposures should not be considerably longer. CCD cameras and computer-aided primary data processing codes are used to take electronic photographs of Mercury with short exposures. Fried (1978) considered the advantages of the short-exposure method following Hufnagel (1966). Fried pointed out the following: "in short-exposure imaging through turbulence, there is some probability that the image will be nearly diffraction-limited because the instantaneous wave-front distortion over the aperture is negligible." Fried analyzed the distortions produced by atmospheric density inhomogeneities with scale sizes r and extent r_0 along the line of sight, which reduce the resolution of astronomical instruments. According to Fried, the turbulence-limited resolution is λ/r_0 and the possible gain in resolution can be 3.4 at short exposures.

The main conclusions reached by Fried (1978) are that the probability p of a "lucky short exposure" at fixed turbulence scale r_0 decreases sharply when the telescope diameter D increases. Fried also concluded that predawn observations when there is still no atmospheric turbulence are most favorable, while for daytime observations (with small zenith distances) fairly long exposures can be taken during weak daytime winds. There may be experimental confirmation for the latter conclusions. Of the two most successful series of our observations, one pertains to the early morning of November 3, 2001, when the rain clouds above the Abastumani Observatory suddenly dispersed during a calm, while the other pertains to the evenings of May 1 and 2, 2002, when the observations at the Skinakas observatory were performed under conditions of a strong wind. These results may be considered as experimental confirmation of the latter conclusions by Fried (1978).

The conclusions reached by Fried (1978) about the advantages of small telescopes repeated in Mendillo *et al.* (2001) are debatable, since these probably disregard the fact that the exposure with a 1.5-m telescope can be an order of magnitude shorter than that for a 0.5-m telescope at the same signal-to-noise ratio. Since the number of photons per CCD pixel is always limited and subject to significant fluctuations, a good result can be obtained only by simultaneously processing many thousands of electronic photographs. However, the available observing time for Mercury is always limited. Therefore, the required amount of data can be obtained only with a sufficiently large telescope. Previously (Ksanfomality 2003), we considered other practical limitations. Our photographs showed that the image quality often changes in only 99 ms (Fig. 1a). More stable decay or enhancement of atmospheric instabilities appears and disappears in several seconds (or tens of seconds). An effect that is not quite understandable, but familiar to observers, is occasionally observed in

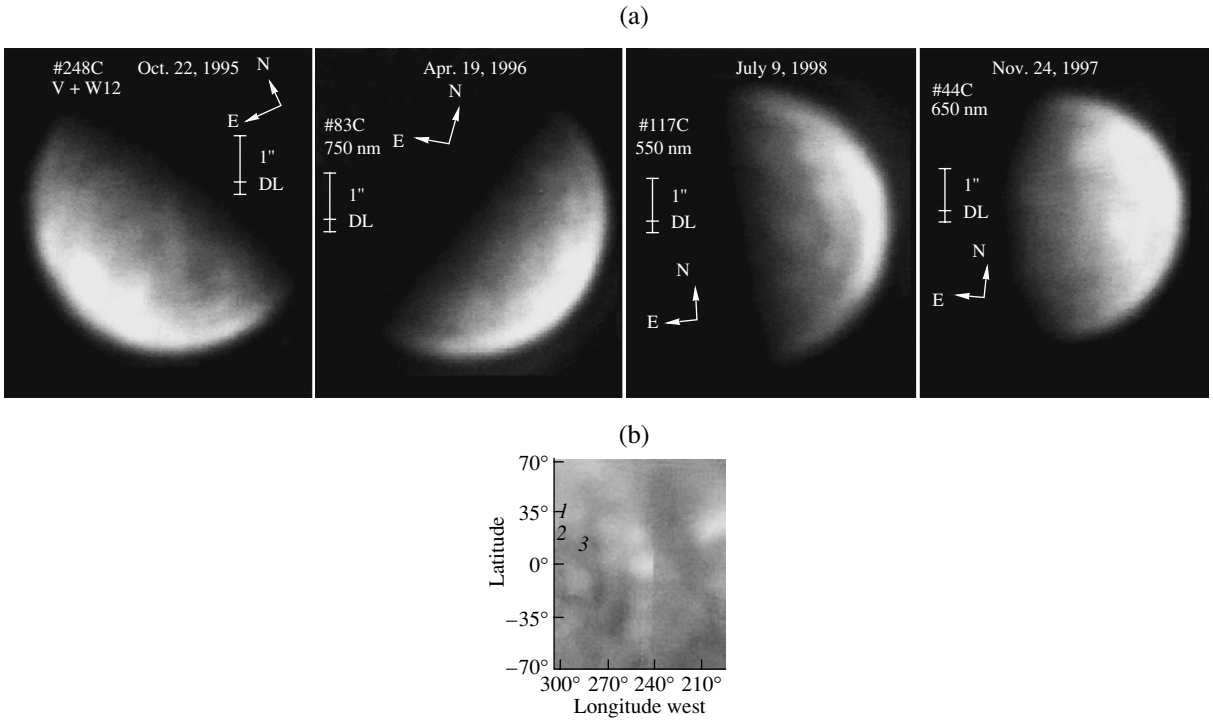

Fig. 2. (a) Examples of single electronic photographs of Mercury taken by J. Warell at the La Palma Observatory in the period 1995–1998. (b) A fragment of Mercury's photomap from Warell and Limaye (2001).

series with a large number of electronic photographs: the images occasionally prove to be rotated through several degrees (Fig. 1b), which makes it difficult to process them simultaneously.

Returning to the potentially attainable resolution that Fried likens to the diffraction limit of an instrument, his analysis should be complemented by the features that the image synthesis from a large number of primary photographs entails. As we show below, details that are formally even beyond the diffraction limit can be resolved by this method. The processing of our observations in May 2002 is such an example. The observations were performed in the near infrared (690–940 nm) using a 1.29-m telescope. The geocentric distance of Mercury was 0.87 AU. At a ratio of $1.22\lambda/D = 0.16$ arcsec, the limiting resolution of the planetary surface would be exactly 100 km. Therefore, one would think that surface features 40–60 km in diameter are outside the capabilities of the method. However, this is only an apparent paradox. The distribution of intensity y at distance x from the image center is known to be $y = [2J_1(x)/x]^2$, and the coefficient 1.22π corresponds to the position of the first minimum (dark ring). If we choose features at a level, for example, of 0.85, their size will naturally be smaller. However, this requires a large number of processed primary images, which holds in our image synthesis code. Specialists know this method well. For example, many published HST images of celestial objects are produced precisely by this processing.

1995–2002 WORKS ON MAPPING THE SURFACE OF MERCURY USING GROUND-BASED ASTRONOMICAL FACILITIES

The works by J. Warell (Upsala Astronomical Observatory, Sweden) stand out among the pioneering studies of Mercury with relatively short exposures. Warell began his observations in 1995. Various stages and results were described by Warell and his coworkers in publications (Warell and Limaye 2001; Mendillo *et al.* 2001; Warell 2002, 2003; Warell and Blewett 2004). Two 1.4- and 1.6-megapixel CCD cameras were mounted on the Swedish 0.5-m vacuum solar telescope at the La Palma Observatory with a focal length of 22.35 m. A set of filters from 450 to 940 nm was used. The exposures were chosen from 25 to 360 ms. In the above publications, Warell provided single (nonsynthesized) photographs chosen from a large number whose examples are shown in Fig. 2a. Although the exposures are comparatively long and the images are single ones, large features are distinguished in the photographs rather clearly. This even allowed the authors (Warell and Limaye 2001; Mendillo *et al.* 2001) to perform their preliminary global geological interpretation based

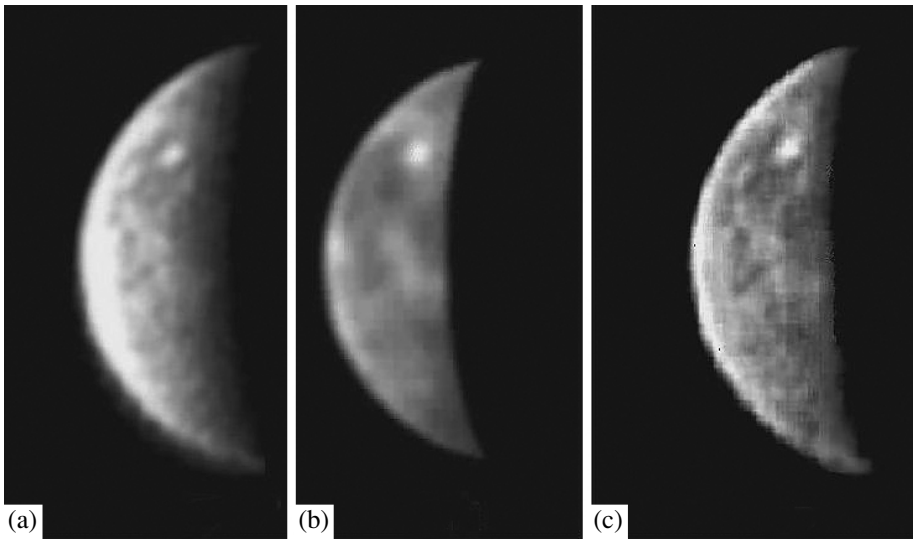

Fig. 3. Images of Mercury at phase 106° obtained by the teams of (a) Dantowitz *et al.* (2000) and (b) Baumgardner *et al.* (2000). (c) Mercury's image synthesized from images (a) and (b) by a method described previously (Ksanfomality 2003).

on the identified fuzzy features marked by numbers in Fig. 2b (see below). The authors believe that they managed to achieve a resolution of 200 km. Subsequently, to produce a more detailed image of the planet, Warell passed the primary photographs over to us to be processed by the software package used in our previous papers (Ksanfomality 2003, 2004). Unfortunately, because of the limited number of primary photographs, we failed to perform a satisfactory correlation matching of the planetary images.

On August 29, 1998, Dantowitz *et al.* (2000) and Baumgardner *et al.* (2000) photographed Mercury in the longitude range that was not photographed by Mariner 10 in 1974 using an ordinary (general-purpose) video camera mounted on the 1.5-m Mount Wilson Observatory telescope. The video camera operated in standard mode, with a frame rate of 30 s^{-1} and an exposure of 17 ms. A total of 219 000 frames were taken, of which 1000 photographs were chosen for further processing. Mercury was imaged at phase 106°, in the longitude range 265°–330° W, and with the coordinates of the subterral point 7.7° N, 254° W (Figs. 3a, 3b). This was probably the best results of the works published until 2001. In a joint paper of the authors from both groups by Warell and Baumgardner *et al.*, their results are compared (Mendillo *et al.* 2001). The authors estimated the achieved resolution on the surface of Mercury to be 250 km. Previously (Ksanfomality 2004), we additionally processed the results by Dantowitz *et al.* (2000) and Baumgardner *et al.* (2000) by a method presented in our earlier papers (Ksanfomality 2002, 2003), which improved appreciably the image of the planet (Fig. 3c). The synthesized image appears more detailed than the primary images.

In December 1999, Ksanfomality *et al.* (2001) took a series of primary electronic photographs at the Abastumani Astrophysical Observatory using a simple ST-6 CCD camera mounted at the Cassegrain focus ($F = 16$ m) of the AZT-11 telescope ($D = 1.25$ m). Subsequently, they synthesized a test image in which some features could be distinguished. The phase and longitudes in the image accidentally proved to be close to those in the mosaic of *Mariner-10* photographs, which allowed these to be compared (Figs. 4a, 4b).

On November 3, 2001, the next series of observations of Mercury was performed at the Abastumani Astrophysical Observatory at morning elonga-

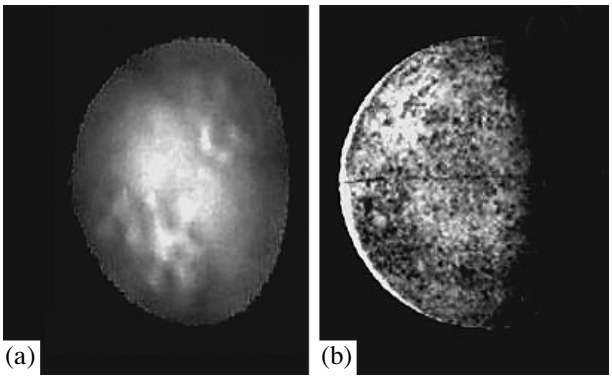

Fig. 4. (a) Test image of Mercury from the observations on December 3, 1999. (b) The position of the planet is approximately the same as that during the Mariner 10 imaging.

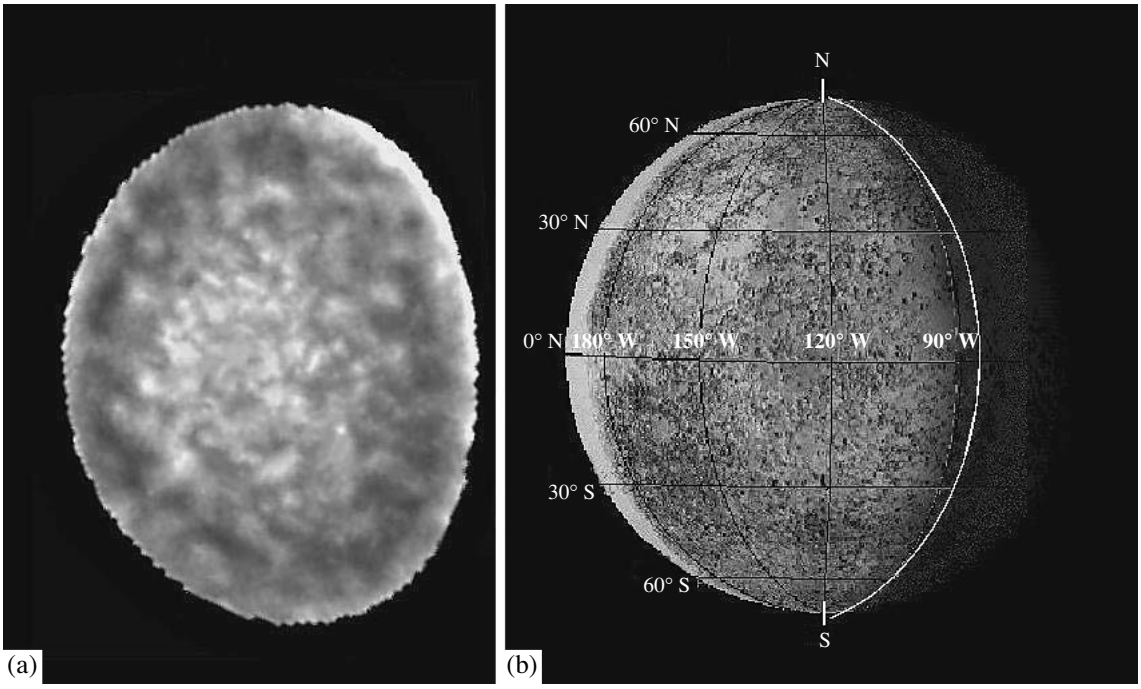

Fig. 5. (a) Image of Mercury synthesized from the observations on November 3, 2001 and (b) its comparison with Mercury's map constructed from the *Mariner-10* mosaic.

tion of the planet. In this experiment, we were able to achieve a very high resolution. The phase of the planet was 63°. We used the same AZT-11 telescope, but with a 700-nm filter that cut off the short wavelengths and with a SBIG STV CCD camera (square 7.4×7.4 μm pixels). The long-wavelength boundary lay near 1 μm and was determined by the spectral properties of the CCD array, which are given in Ksanfomality *et al.* (2002). Since the object is bright, the integration time of several thousand signal units in each pixel, even with a small-pixel CCD array, still did not exceed a few milliseconds. A long-focus instrument has advantages in Mercury's observations, because the nominal resolution, which is important for the subsequent data processing, increases. On November 3, 2001, the disk of the planet was seen at an angle of 6.1 arsec, which corresponded to a linear image size of 0.43 mm in the focal plane of the telescope. The observations were carried out under extremely favorable seeing conditions. Short exposures, 3–10 ms, were used. We took several series of primary photographs, including a series with the recording of the light polarization distribution over the planetary disk, were taken (Ksanfomality *et al.* 2002). Based on the subsequent selection from the electronic photographs taken, we synthesized an image for the longitudes from 90° to 190° using the first version of the data processing software (Fig. 5). The phase and longitudes in the image again proved to be close to those in the mosaic of *Mariner-10* photographs. Previously (Ksanfomality 2003), we showed that features in the central part of the image obtained with sizes of only 100–250 km are clearly identified with the *Mariner-10* data (Fig. 6). At that time, this result was unexpected (since the feature sizes were at the diffraction limit of the telescope), but it convincingly proved the actual capabilities of the new method. The relative rms error of the signal from a single CCD pixel in the specific case was 0.68%, while the triple error $3\sigma_R \approx 2\%$ was quite comparable to the contrast of individual pixels (4–10%). However, since the image is formed not by a single pixel, but by a large group of pixels (1200 pixels in Fig. 6), the probability of their erroneous combination is much lower. At the same time, shortcomings of the data processing code were revealed: the low spatial frequencies (large image features) were suppressed.

THE SURFACE OF MERCURY IN THE LONGITUDE RANGE 210°–285° W FROM THE OBSERVATIONS ON MAY 2, 2002

The images of Mercury given below are based on several series of successful observations carried out in early May 2002 at the Skinakas Observatory of the Heraklion University (35°13′ E, 24°54′ N, Crete, Greece). An SBIG STV CCD camera with a pixel size of 7.4×7.4 μm mounted on a Ritchey–Chrétien telescope ($D = 1.29$ m, $F = 9.857$ m) was used. To

significantly reduce the sky background, the observations were performed in the near infrared (690–940 nm) with cutting-off KC 17 and KC 19 filters (the short-wavelength boundaries are 670 and 700 nm, respectively). The disk of the planet on May 1 and 2, 2002, was seen, on average, at an angle of 7.75 arcsec with a linear size of 0.37 mm in the focal plane of the telescope and corresponded on the CCD array only to 50 lines in zoom mode or 25 lines in normal mode (the combination of four pixels). The phase of Mercury was 93°–97°. Short exposures, mainly 1 ms and up to 10 ms at large zenith distances, were used.

To take the largest possible number of primary electronic photographs of Mercury, the STV camera mounted on the telescope was switched to fast image collection mode. It took 4 s (at a 1-ms exposure with 99-ms intervals) to obtain one frame (Fig. 7) composed of 40 photographs. It took approximately the same time to write the frame to memory. After 15 frames were obtained, the entire set was transferred to a computer. Only a serial (com) port was used in the STV camera for data transfer, which causes additional losses of time and is a shortcoming of the STV camera. Nevertheless, the fast collection of primary images of each frame in some measure compensates for these loses. However, this requires stable seeing conditions, which were observed at the Skinakas observatory on May 1 and 2, 2002. Since the size of each image in Fig. 7 is only 7.75 arcsec, an image unsteadiness of only 1–2 arcsec would brought part of the image outside the CCD fragment used. On the ensuing days, until May 9, the seeing conditions were too poor to obtain anything like Fig. 7.

The observational data obtained with the STV camera in the chosen mode of the latter had an 11- or 11.5-bit compressed format. The routine primary data processing operations included the standard flat fielding and a precheck (the rejection of defective series). Subsequently, the best series of undistorted electronic photographs or single images were selected. The most important procedure was the correlation matching of a large number of images. Various versions of correlation matching codes were tested, but simpler codes invariably yielded better results. In the long run, two image processing codes were chosen: the very successful AstroStack-1 code (Stekelenburg 1999, 2000) and AIMAP-225 (Kakhiani 2003). In general, however, a package of 16 codes with AstroStack-1 and AIMAP-225 being the core codes were used for image processing. The codes were used in multilevel (hierarchical) mode: the groups of selected primary photographs were subjected to first-level correlation matching to produce images, one of which is shown in Fig. 8; subsequently, these, in turn, were subjected to the same operation. After the completion of the correlation matching, small features were identified

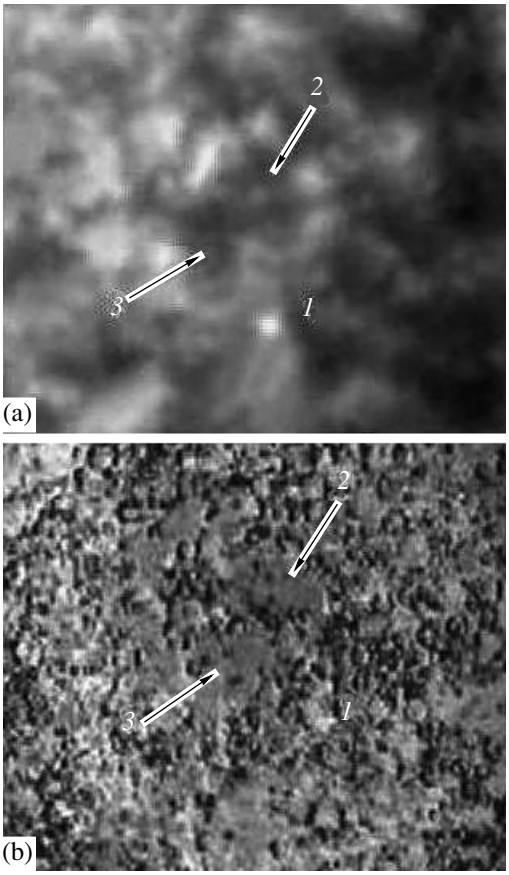

Fig. 6. Comparison of the fragments of (a) the synthesized image and (b) the *Mariner-10* photomap.

by choosing a moderate-depth unsharp mask. In addition, the image resolution could be improved using the Van Sitter or Lucy–Richardson deconvolution algorithms. Both deconvolution operations are built in the AstroStack-1 code. However, it may well be that the deconvolution makes the reproduction of the shades of gray nonlinear. The final operations included the limb- and terminator-darkening correction and plotting a longitude/latitide grid on the image in the computed geometry. The synthesis method was described in more detail by Ksanfomality *et al.* (2005).

Images of the surface in Mercury's longitude range 210°–285° W were synthesized in the course of a process that was continuously perfected and became complicated. The image resolution and the reliability of identifying the detected relief feature of the planet increased accordingly. The first version of the synthesized image (Fig. 9a, the 2003 processing) was based on the processing of the two most successful series of our observations (Ksanfomality 2003). A total of 560 primary photographs were in each series; about 35% of these remained after manual selection. This comparatively rough image immediately showed

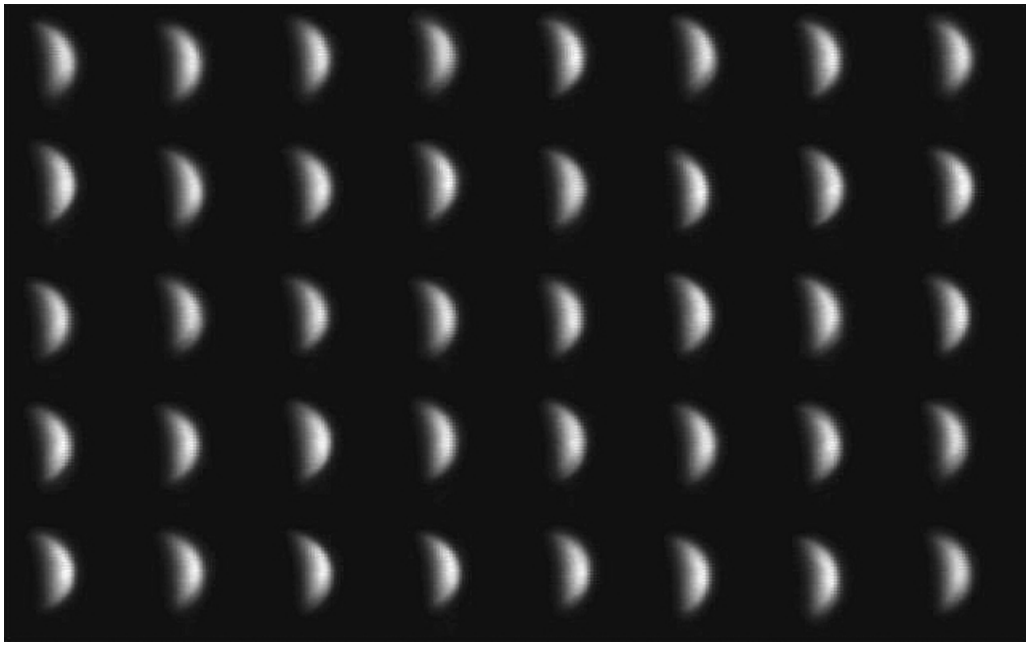

Fig. 7. Example of a frame from a group of primary electronic photographs of Mercury. The exposures are 1 ms each, and the intervals are 99 ms.

the largest structures in Mercurian's longitude range 210°–285° W.

Substantial progress in resolution was made in 2004, when we managed to complete the processing of the main data set collected in the observations on May 2, 2002 (performed in the near infrared, 690–940 nm). The second version of Mercury's synthesized image was based on a considerably larger number of primary photographs (the selection from 5240, except the photographs used to synthesize the first version of the image). Figure 9 shows three synthesized images of Mercury at phase 97°, which show how the images improved as increasingly more primary photographs were included in the synthesis and as the synthesis technique itself was perfected. The location of the coordinate grid is shown in Fig. 9d. The coordinate identification error does not exceed a few degrees, but it increases near the poles. The coordinate grid was constructed by taking into account the fact that the north pole at the time of observations was displaced from the limb toward the observer by ~1°.5 (on Mercury, 1° corresponds to 42.6 km). Although all of the large image features in Fig. 9a are present, the versions of Figs. 9b and 9c are appreciably sharper. Fairly small structures can b distinguished in Fig. 9c. The positions of large albedo or relief features are schematically shown in Fig. 10a, where arbitrary feature boundaries specified by shades of gray were plotted on the image field. Here, the locations of the boundaries are presented more clearly. The image contrast in Fig. 10 was reduced significantly, which allows us to discern those features that are near the terminator. In Fig. 10c, the coordinate grid was superimposed on the boundaries, while Fig. 10b shows the positions of the most prominent features considered below.

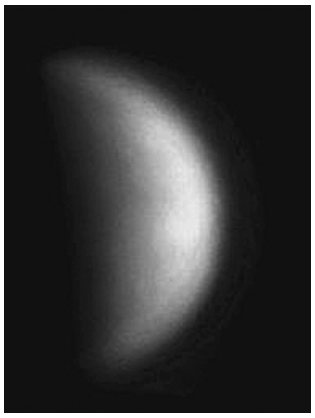

Fig. 8. First-level correlation matching of a group selected from 560 primary electronic photographs of Mercury.

Since the gradations of albedo (or relief) features are small, the possibilities for increasing the contrast are limited: for the same form of the gamma function, increasing the contrast of some features leads to the suppression of other features. Two very light regions near the limb centered at 32° N, 235° W and 6° S, 230° W and a large dark "basin" (according to the lunar terminology) near the terminator (*1* in Fig. 10)

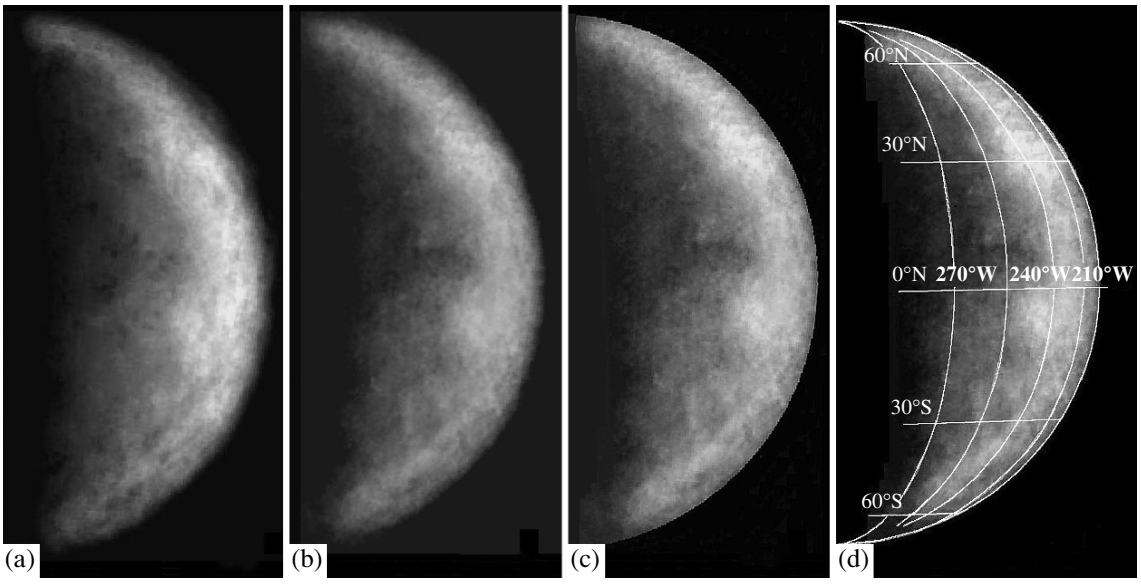

Fig. 9. Progress in the resolution of synthesized images for Mercury at phase 97° (the observations on May 2, 2002). The longitudes are 210°–290° W, and the central meridian is at 286° W. Images (a) and (b) were synthesized from independent primary data that number 1120 and 5240 primary electronic photographs, respectively. Image (c) is a combination of parts (a) and (b) with their weight coefficients. Image (d) shows the location of the coordinate grid. The image of Mercury synthesized from the observations on May 2, 2002. The near-infrared range, 690–940 nm.

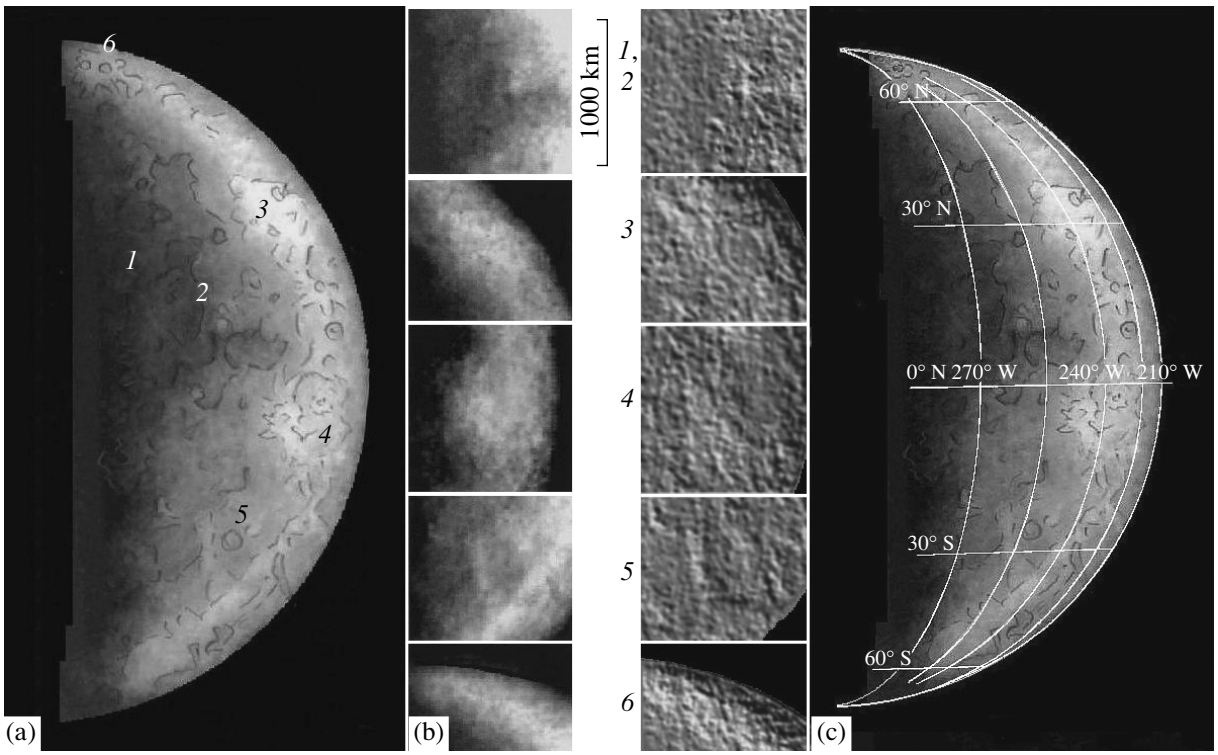

Fig. 10. (a) Arrangement of Mercurian features in the longitude range 210°–290° W. (b) The column of enhanced-contrast images on the left; the view of the same areas obtained using a special image processing code is on the right. (c) The location of the coordinate grid.

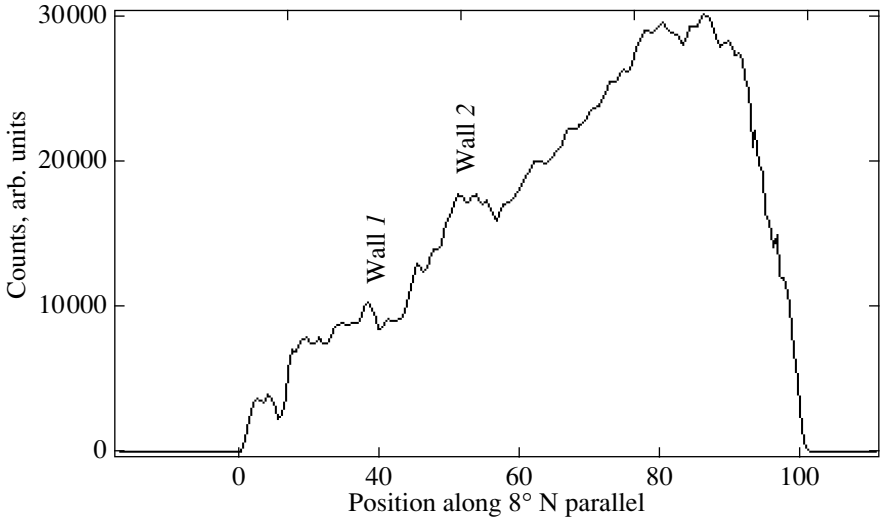

Fig. 11. Rims of the Skinakas Basin.

centered approximately at 8° N, 280° W are most prominent in Figs. 9a–9c. The basin, the largest formation in the longitude range 210°–290° W, has a structure that more or less resembles some of the large formations on the far side of the Moon with a diameter of the inner part ~25° (1060 km) and twice the diameter of the discernible outer rim (*2*, Fig. 10). The basin is probably a very old (possibly the oldest) formation on Mercury, with broken rims that are actually created by the boundaries of other, smaller basins. Nevertheless, signatures of the rims are clearly seen in Fig. 11, which shows a photometric profile through Mercury's image (Fig. 9a) along the 8° N parallel. This is the largest basin on Mercury. When processing the observations, we used the nickname "Skinakas Basin" (after the Observatory where the primary data were obtained) for this formation, without having any pretension to making this legally binding; the IAU is known to name all objects on the surface of Mercury after writers, composers, artists, etc. Nevertheless, the name "Skinakas Basin" (or "Skinakas Mare") mentioned at several conferences has already gotten into the literature.

It is interesting to compare the Skinakas Basin with the lunar relief. The inner part of the basin slightly exceeds in size the largest lunar Mare Imbrium, while its outer part has the scales of the lunar Oceanus Procellarum. (Therefore, the commonly encountered (in the literature) assertion that Mercury has mainly a highland relief (according to the lunar terminology) should be ascribed to only the part known from *Mariner-10* photographs.) The structure of the Skinakas Basin was examined in detail previously (Ksanfomality 2004). The inner rim of the Skinakas Basin is more or less regular in shape. The diameter of the outer rim is ~2300 km, which is 0.48 the diameter of the entire planet and makes the Skinakas Basin one of the largest crater maria on the terrestrial planets. The irregular shape of the outer rim, which is comparatively regular on the eastern side, is distorted by an object centered at 30° N, 280° W in the north and by an extensive, lighter region located between 255° and 280° W reaching 30° S in the south. The Skinakas Basin is probably similar in structure to the surface of the region of Caloris Planitia known from *Mariner-10* photographs, which is assumed to have an impact origin. Previously (Ksanfomality 2004), we compared the sizes of the Skinakas Basin and Carolis Planitia, which also has a double rim. The diameter of the Skinakas Basin is a factor of 1.5 larger than that of Caloris Planitia. In contrast to the Skinakas Basin and Caloris Planitia, the surface of Mare Imbrium is a lava field the formation of which dates back to the ancient epoch of global lava flows on the Moon. However, it is not quite appropriate to compare the Skinakas Basin with lunar mare regions. In general, their albedo is a factor of 2–3 lower than that of the highland relief. Since the data processing when Mercury's images were synthesized included the unsharp mask operation, the albedo variations are difficult to estimate reliably. In general, the lunar-type lava covering is comparatively uniform in albedo; therefore, based on the spotty structure of the central part of the Skinakas Basin, we assumed in a previous paper (Ksanfomality 2004) on the recommendation of V.V. Shevchenko that the basin is similar in nature to the surface of the central part of another lunar formation, the South Pole–Aitken basin. The latter has a diameter of 2500–3000 km at the outer boundary, which is quite comparable to the Skinakas Basin. If the Skinakas Basin is assumed to be actually a

broken impact crater, its sizes point to a very large impact event that dates back to the early history of Mercury, when the large planetesimals in the Solar System had not yet been exhausted.

Several other, smaller formations that were examined previously (Ksanfomality 2003; Ksanfomality *et al.* 2005) are distinguished in the synthesized images. However, how can we be sure that these formations actually reflect the geography of the Mercurian surface? Since the surface of Mercury in this part of it was unknown, the first and main criterion for the features being real remained their presence in several synthesized images obtained independently and from different groups of primary electronic photographs (Ksanfomality 2002, 2003). Using this criterion proved to be the most reliable method for confirming that these features are real. However, in two cases, we also managed to find the detected features in independent publications. These are the formations near the north pole (*6* in Fig. 10) that are examined below and the Skinakas Basin itself.

Only the eastern part of the Skinakas Basin is seen in Figs. 9 and 10. Nevertheless, we managed to synthesize the full image of the Skinakas Basin. For this purpose, we took the eastern part of the basin from our data and its western part from the revision (Ksanfomality 2004) of the results by Dantowitz *et al.* (2000) and Baumgardner *et al.* (2000) mentioned above, Fig. 3c. On their basis, we constructed the full image of the Skinakas Basin. As was noted above, the authors of the above two publications took numerous electronic photographs of Mercury at phase 106°, in the longitude range 265°–330° W, and with the coordinates of the subterral point 7.7° N, 254° W on August 29, 1998, using the 60-inch Mount Wilson Observatory telescope. Each of the teams published their results (Fig. 3). In one case, analog data sets were processed, while in the other case, digital data sets were processed; the latter were subsequently used to synthesize the images of the planet. As far as we can judge, the reason why the primary images differ is that the terminator in the publication by Baumgardner *et al.* (2000) may have been aligned artificially. Both teams point out the brightest object in the upper part of the image (~35° N, ~300° W). In addition, Dantowitz *et al.* (2000) pointed out the following: the observed features include wide albedo variations, several small bright spots, and an interesting ring object at the terminator approximately at 10° S, 270° W. Baumgardner *et al.* (2000) called this object a large dark marelike region at (~15°–35° N, ~300–330° W). It is easy to see that in both cases, this position virtually coincides with the position of the center of the Skinakas Basin.

The fortunate location of the Skinakas Basin in Figs. 3 and 9 allowed both its halves to be matched. The results of matching the images of the western and eastern parts of the Skinakas Basin were presented previously (Ksanfomality 2004; Ksanfomality *et al.* 2005) and are shown in Fig. 12, where the Skinakas Basin is located near the terminator in both cases. The locations of the sunlit parts of Mercury together with the coordinate grid during the 1998 and 2002 observations are shown in Figs. 12a and 12b, respectively. Figure 12c shows the matched image. Since the matching was performed without coordinate transformation, it definitely cannot be exact. However, the limited resolution of the primary images makes the result quite acceptable even without coordinate transformation.

As can be seen from Fig. 12c, the Skinakas Basin is a typical crater mare with a dark central part and a periphery of complex structure. The scale of the formation is shown on the right. As was estimated above, the sizes of its central and outer parts are ~1000 and ~2000 km, respectively. The image is not sharp enough: large features are identified reliably, but their detailed description requires new observations. It is pertinent to note that the vague dark formation on the scheme by Mendillo *et al.* (2001) denoted by number *3* in Fig. 2c coincides in position with the Skinakas Basin.

PECULIAR REGIONS IN THE LONGITUDE RANGE 210°–285° W

To enhance the edges of the most interesting regions, the contrast of individual image fragments was additionally increased. This actually increases the discernibility of individual interesting regions, but at the expense of the adjacent lighter or darker parts of the images, which do not fall on the selected fragments for such processing. Figure 10a indicates the chosen regions, and the column in Fig. 10b (at the center) shows examples of five such regions in the form of individual fragments. The left column shows enhanced-contrasted areas. Since the printing capabilities are always limited, the right column can be of use. In it, a view of the same areas was obtained with a special image processing code that was used by Ksanfomality *et al.* (2002), but was rejected as suppressing the low spatial frequencies. At the same time, the code proved to be quite acceptable for deriving the bounded image fragments, as can be seen from Fig. 10b on the right. The coordinate grid is shown in Fig. 10c.

The structure of the Skinakas Basin region (*1* and *2* in Fig. 10a) is more complex than can be inferred from Fig. 9a. Its jagged eastern periphery is formed by individual dark regions with two small light objects ~100 and 60 km in size (the approximate coordinates

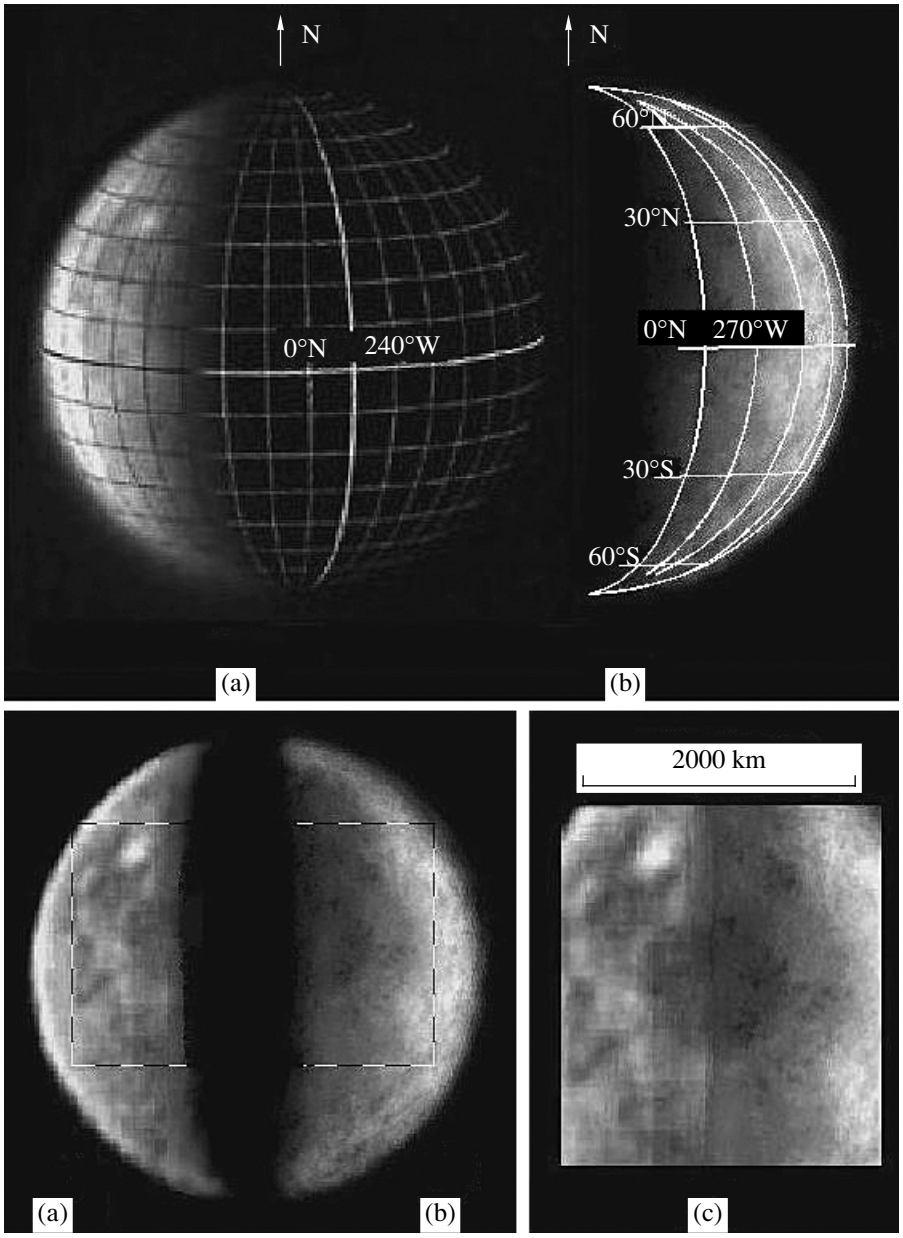

Fig. 12. Phases of Mercury on (a) August 29, 1998 and (b) May 2, 2002. These longitudes were not photographed by Mariner 10. The corresponding synthesized images (a, b). The dashed line indicates the image fragments used for matching. (c) The full image of the Skinakas Basin constructed with a small overlap of the matched parts. The matching was performed without coordinate transformation.

are 12° N, 260° W). Extensive dark regions 400–600 km in size are adjacent to these on the west and on the south. Region *1*, with an increased contrast and with a view of the area processed by the special code, is shown in the central column. A large impact crater ~300 km in diameter (centered approximately at 14° N, 270° W) is located approximately in the middle of the 400-km dark region to the west of the light object. If only this crater is selected, then it is found to have a discernible ray system. The entire eastern periphery of the Skinakas Basin is a superposition of large crater maria and basins, which also suggests that the Skinakas Basin is an old structure. As regards its central part, which is located at the terminator, an object that may be the central hill of this giant basin (Fig. 10b, the left part of fragment *1*) is distinguished at its center. The presence of a central hill is among the criteria that allow the basin to be classified as a crater mare. The central part is better seen in Mercury's image at a different phase, the observations on May 1, 2002. This image

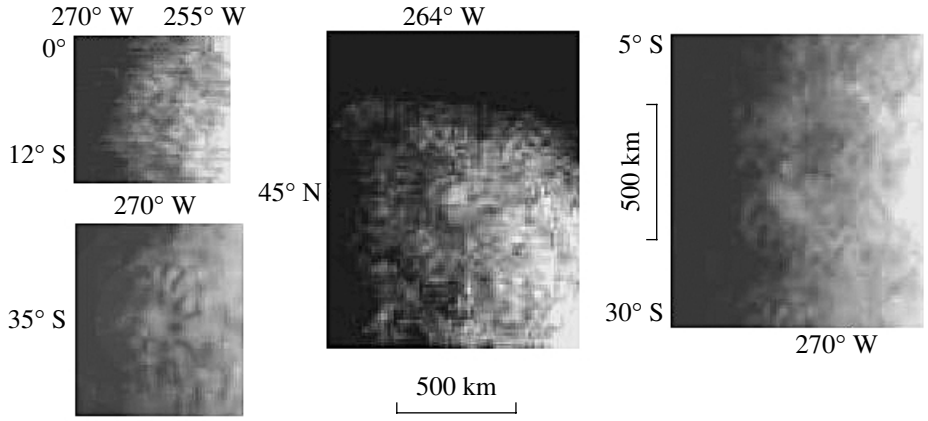

Fig. 13. Large craters with ejecta are most discernible near the terminator. The craters on the left pertain to the synthesized image of Mercury for May 2, 2002; the craters at the center and on the right pertain to the synthesized image for May 1, 2002. The observations were performed in the near infrared, 690–940 nm.

was also synthesized using a base of 7840 primary photographs.

The extensive region of complex structure centered at 32° N, 235° W (*3* in Figs. 10a and 10b) is lightest at Mercury's phase in question (97°) and in this part of the planet. It could have been assumed to be a large young impact crater, but it does not appear as a ray structure in any of the synthesized images. In the high-contrast fragment *3*, the region appears as an 800-km system of disordered very light areas. Some of these are similar to ring structures, but have no rays. However, when specially processed, the entire fragment *3* proves to be a round ~500-km basin of regular shape, which is shown in the central column. At the same time, craters with extended rays are seen in many regions of the planet (e.g., at 8° S, 265° W). The center of the large crater, possibly with a ray system, lies at 7° S, 247° W. It is adjacent to the second-brightest region of this Mercurian hemisphere on the west at the phase in question (*4* in Figs. 10a and 10b). The light areas form here arcs closed into a ring formation 600–700 km in diameter. After a special processing of the image, fragment *4* turns into a typical lunar-type crater mare of regular shape with a double broken rim.

Numerous impact craters become noticeable when selectively increasing the contrast. Fragment *5* in Fig. 10b centered approximately at 21° S, 248° W is such a crater with a diameter of 140 km and a ring of ejecta 450–500 km in diameter around it. The areas that are adjacent to the rim from the outside are probably the ejecta from the crater. Such craters are encountered virtually in all regions of the longitude sector 210°–290° W. Figure 13 shows four other large impact craters that were near the terminator during the observations. The craters centered at 45° N, 264° W and 15° S, 270° W were taken from the image at phase 93° (the observations on May 1, 2002). All these craters have wide terraces of ejecta. Statistically, the impact Mercurian craters are a factor of 1.5 smaller than the lunar ones, which is known to be attributable to a factor of 2 larger gravity. Since our results have a limited resolution, we cannot yet check this dependence based on the results obtained. Large impact crater *6* with an extensive nimbus of ejecta 6° (280 km) in diameter is present at the northern cusp near the pole in all our synthesized images (Figs. 9 and 10). Its central dark region is 2° (90 km) in diameter. The nimbus of the crater is appreciably lighter than the surrounding features and stands out against their background. There is a slightly smaller crater ~60 km in diameter on its northern side at 2°–3° closer to the pole. The latitude of the large crater is 85° N. Recall that the north pole at the time of observations was 1°.5 closer to the observer than the limb; therefore, the polar zone is seen in Figs. 9 and 10. Since the crater is close to the pole and since the limb in the synthesized image of Mercury is slightly blurred, the crater longitude (285° W) is determined with a probable error of no better than 5°. However, we were able to compare the position of the crater with independent data: there is a detailed radar map for the north polar region with a resolution as high as 1.5 km (Harmon *et al.* 2001), with a group of large impact craters. It is these craters that are probably seen in the synthesized images. These are compared with the radar map from Harmon *et al.* (2001) in Fig. 14. The size and position of the crater at 85° N coincide almost completely with those of crater K (centered at 85.5° N, 292° W with a diameter of ~80 km). The smaller crater on the left is object J in the same figure at 87° N, 280° W with a diameter of ~50 km. Interestingly, the nimbus of ejecta is seen on the radar map only on the northern

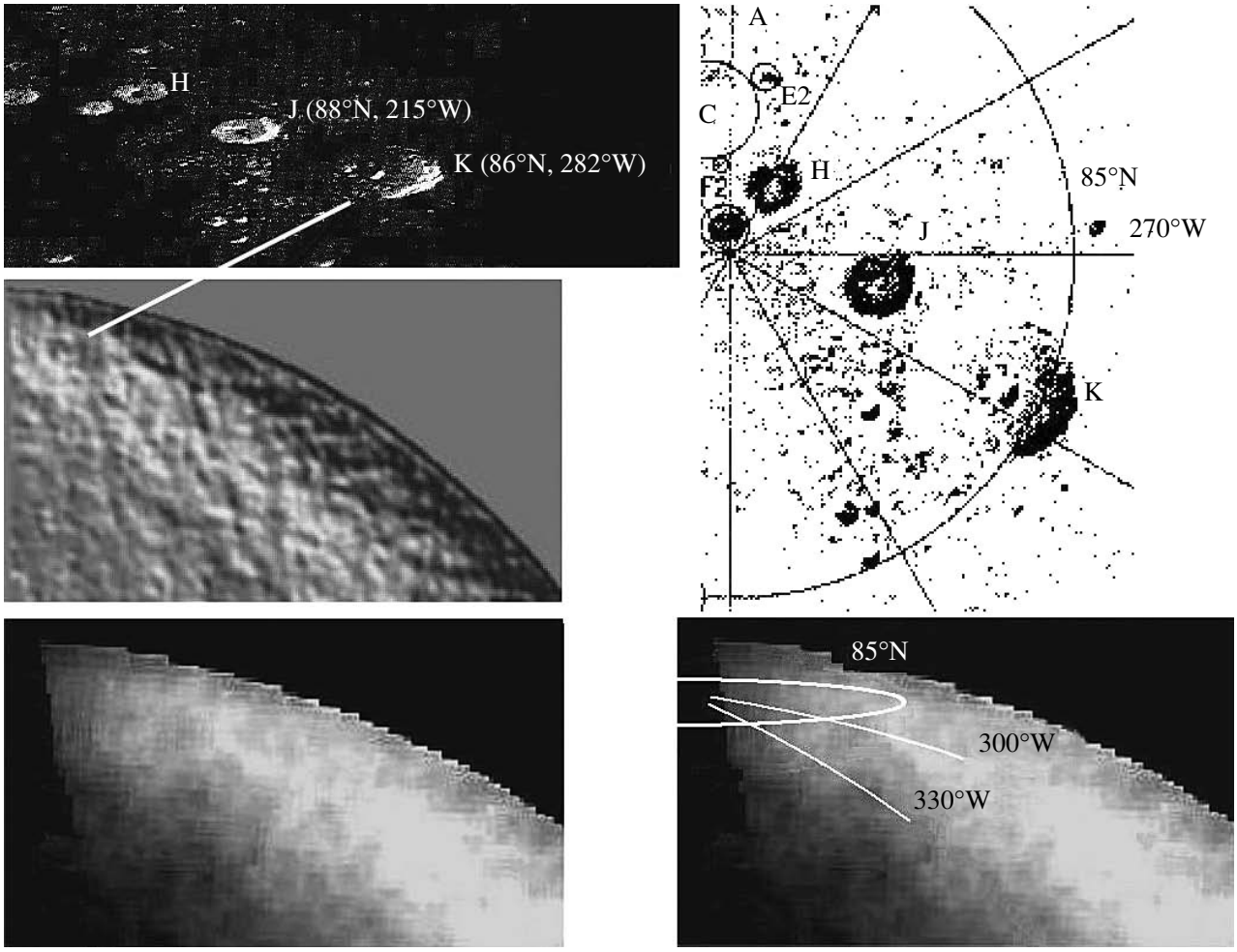

Fig. 14. Comparison of the image features at the northern cusp of Mercury (the middle and bottom panels) with the radar map for the northern polar region (Harmon *et al.* 2001). Craters H, J, and K are shown at the top, as they are seen at the phase in question.

side of crater K as a dark belt without features, while in the optical range, the terrace of ejecta encloses the crater on all sides, with this terrace being seen as a light structure. It can also be noted that the southeastern ray of ejecta ends near a considerably darker object than crater K (the lower panel in Fig. 14 on the left). This dark crater is located in the penumbra zone behind the terminator (centered at 84° N, 320° W with s diameter of ~80 km). It is only outlined on the radar map (on the right in Fig. 14). The high brightness of the ejecta from crater K can be correlated with the crater features shown on the radar map. According to Harmon *et al.* (2001), the polar craters are unusual in nature. Large masses of ice are probably located on their floors beneath a layer of regolith. The floors of the polar craters are always in the shadow of their rims and have a temperature low enough for ice to be preserved on cosmogonic time scales. According to another hypothesis (Sprague *et al.* 1995), there are deposits of sulfur on the crater floors that has scattering properties similar to those of ice in the decimeter range. In our case, a different thing is important: it may well be that the high albedo of the ejecta is related to the nature of the craters.

Since the sizes of the regions identified with craters J and K are small, it is pertinent to remind the remark made in the Advantages of the Short-Exposure Method in Observations of Planets about the discernibility of features with diameters of 40–60 km on the surface of Mercury. Ideally, the point spread function (PSF) described by the expression $y = [2J_1(x)/x]^2$ at a level of 0.85–0.90 allows fairly small features, smaller than the diffraction limit corresponding to 0.7, to be distinguished, but this requires a large number of processed images, which was about 15 000 in the case of Figs. 9 and 14.

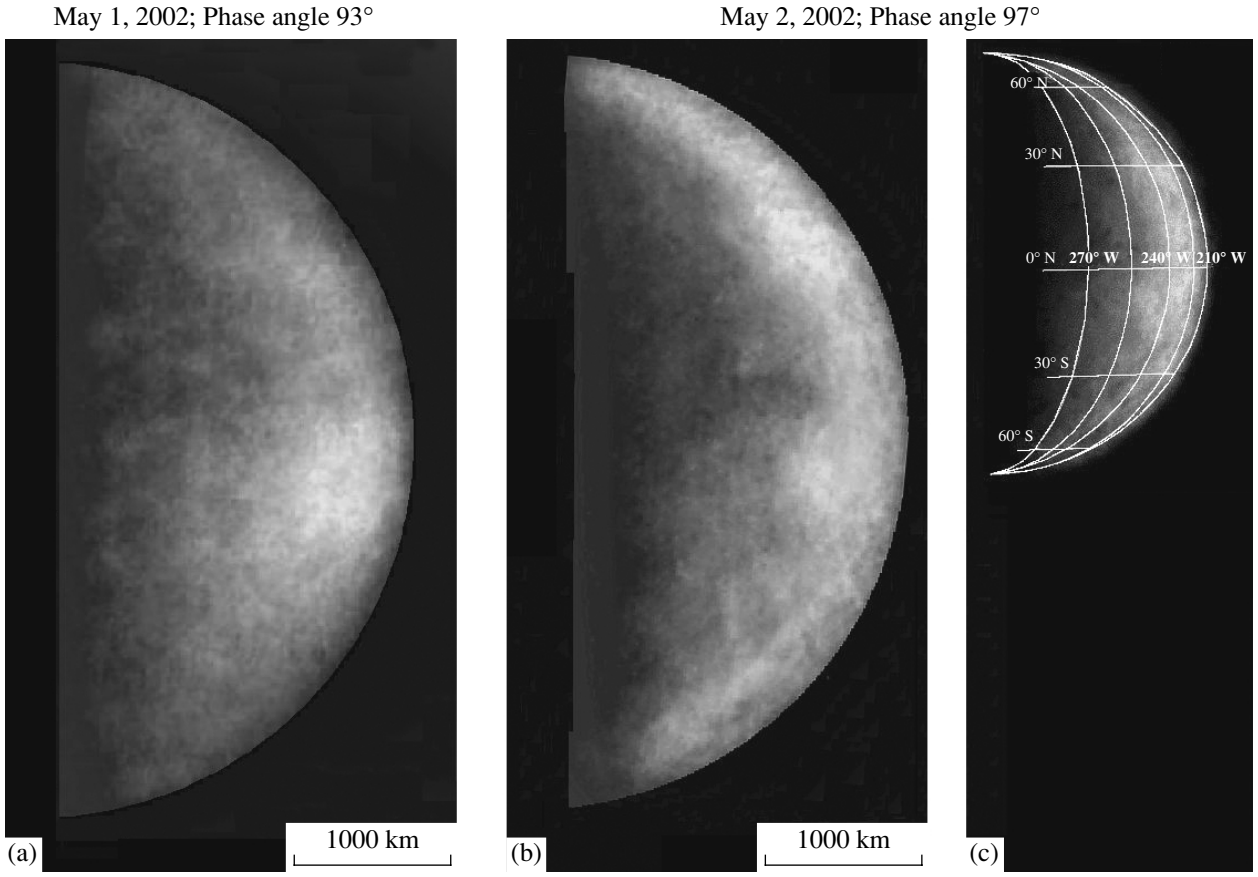

Fig. 15. Mercury's image (a) at phase 93° (the observations on May 1, 2002) and (b) at phase 97° (the observations on May 2, 2002). The images were synthesized from independent primary data. (c) The location of the coordinate grid.

COMPARISON OF THE VIEWS OF THE MERCURIAN SURFACE IN THE LONGITUDE RANGE 215°–290° W AT PHASES 93° AND 97°

It is well known from lunar observations that the view of an atmosphereless celestial body changes rapidly as it passes through its quadrature. It was interesting to trace the pattern of change in Mercury's view at this favorable phase, especially since, in contrast to the Moon, all sides of the planet are observable in principle at any phase. Unfortunately, we were able to obtain images only at two phases, since our observations in May 2002 were limited only to two evenings, May 1 and 2, due to meteorological conditions; the meteorological conditions on May 2 (phase 97°) were appreciably better. The image was synthesized from the observations on May 1, 2002, (phase 93°) using 7840 primary photographs. Despite their large number, the image at phase 93° is inferior in feature distinctness to that at phase 97° precisely because of the less favorable meteorological conditions. The observations themselves on May 1 and 2 were performed at the same time of the day. In one day, the subsolar point on Mercury is displaced, on average, by 6° toward the larger west longitudes, while the phase angle changes, on average, by 4°. Thus, the rate of change in Mercury's phases is half that of the Moon.

Two views of the planet, at phases 93° and 97°, are shown in Figs. 15a and 15b. Figure 15c shows the location of the coordinate grid. Although the phase difference is small and the subterral point in Fig. 15a is displaced rightward, the objects at the terminator are seen much better owing to the earlier phase, as, for example, the craters at 45° N, 264° W and 15° S, 270° W shown in Fig. 13. The structural features of the Skinakas Basin are seen much better. The large dark area that has not yet reached the limb at phase 93° is located northeast of region *3*. As regards region *3* itself, its brightness at phase 93° is appreciably lower than that at phase 97°. It can probably be concluded from the sharp rise in the brightness of region *3* in Fig. 15b as the phase changes by only 4° that region *3* is young. The young Tycho crater on the Moon is known to have the same properties. The lightest region near the limb south of the equator (*4* in Fig. 10), at this phase is the brightest object on the surface of Mercury. In general, the ring outlines of

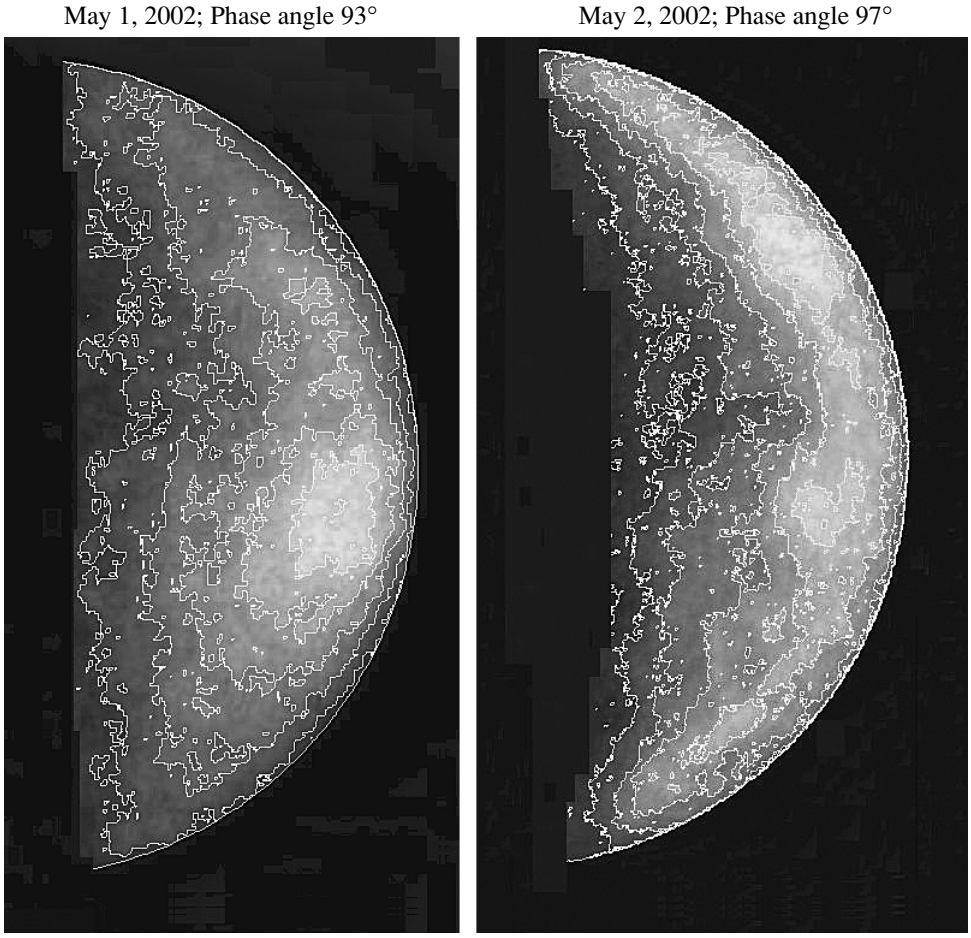

Fig. 16. Photometric profiles of the images at phases 93° and 97°.

region *4* are the same as those at phase 97°; its entire structure reaching 1000 km in diameter appears light, while its western part remains brightest at phase 97°.

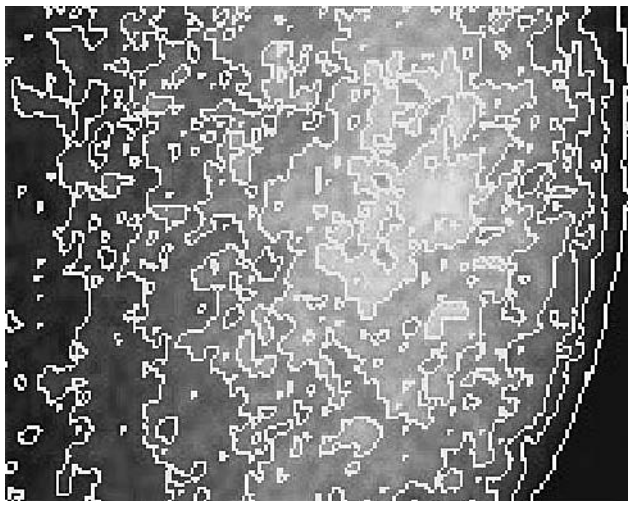

Fig. 17. Photometric profiles of the image of region *4* at phase 93° (7 levels).

At phase 93°, region *4* is considerably brighter than region *3* (Fig. 16), the brightest at phase 97°. This interesting object is indicated in more detail in Fig. 17 by isophotes of seven levels. In addition to the bright core of region *4*, we can see in the figure such large features as the dark arc that passes along the diagonal through the center in the southeast direction. However, we were able to obtain the most interesting results by reconstructing the surface relief.

The brightness of individual features is determined both by the illumination conditions and by the reflective properties of the surface area in question. However, it is well known from the Moon's physics that the boundaries of geological provinces accompany the gradations of brightness. Therefore, the images obtained can in principle contain information about the relief of the planet. We made such an attempt to reconstruct the relief of Mercury in the longitude range 215°–290° W by processing the observations on May 2, 2002, (shown in Fig. 9c) with the data processing code mentioned above that was used by Ksanfomality *et al.* (2002). Owing to the large number of primary photographs and their good quality, the result appears to have exceeded the expec-

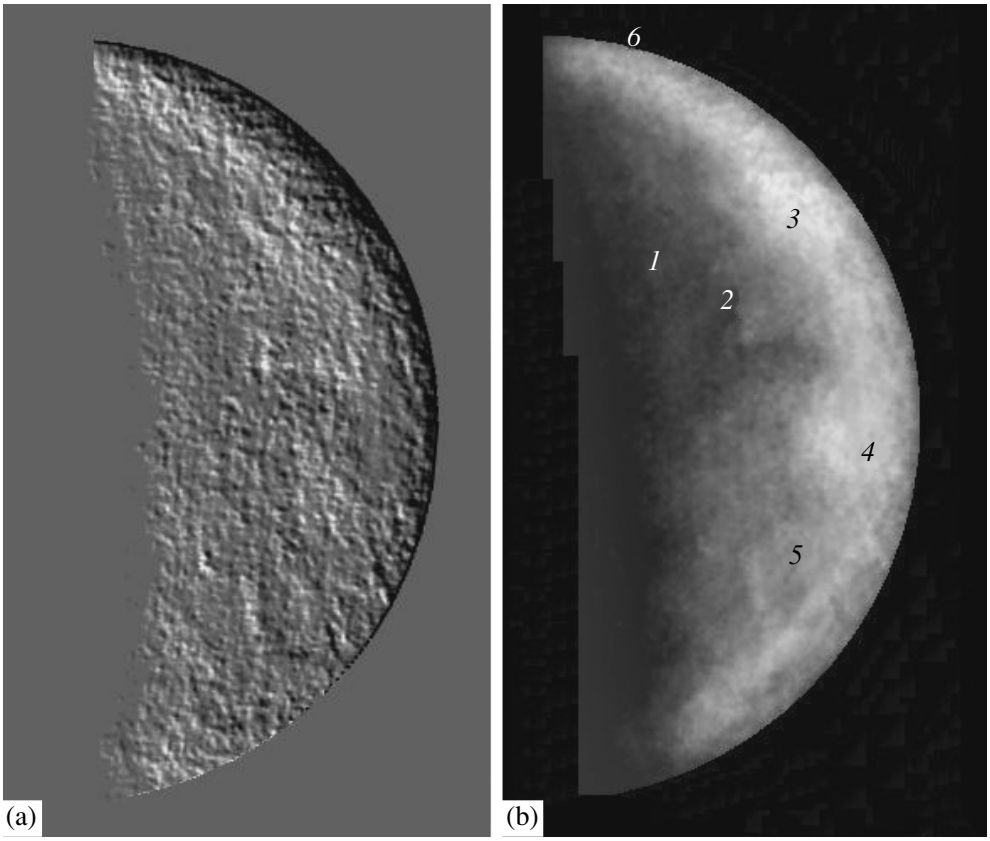

Fig. 18. Relief of the sector 210°–290° W (a) reconstructed from image (b).

tations. It is shown in Fig. 18a without any additional processing and retouching. The direction of the conditional illumination is from the southwest. The phase effects and the shades of gray are suppressed. In the right part (Fig. 18b) in the primary image, the same regions as those in Fig. 10a are marked. Figure 18a allows some of the estimates given above to be improved. Regions *1* and *2* (Skinakas Basin) are actually a superposition of ~500–700-km broken old depressions similar to crater maria with central structures, hills or craters. Region *3* resembles a deformed 800-km crater mare of complex structure. The crater mare *4* (centered at 6° S, 230° W with a diameter of ~700 km) with a double rim has the sharpest edges in the longitude sector 210°–290° W. A more broken large crater mare ~1050 km in diameter with a well-defined center at 7° S, 247° W and a broken double rim is adjacent to it on the west. Depression *5* and other areas are also distinguished. We plan to devote a special paper to a more detailed geological interpretation of the longitude sector 215°–290° W.

Concluding this overview of our results, it is interesting to compare the synthesized images with the *Mariner-10* photographs as a whole. This comparison is shown in Figs. 19a and 19b. Although the longitudes are completely different, the similarity between the views of the surface at them is very convincing. We conclude that the synthesized images roughly correspond in resolution to the photographs taken by the *Mariner-10* camera from a distance of 1 million km (Fig. 19a). At the same contrast, two or three large dark areas similar to those in Fig. 19b can also be distinguished in Fig. 19a. In general, however, the view of the Mercurian hemisphere in the longitude range 15°–190° W known from *Mariner-10* photographs differs markedly from the planet at phase 97° for the longitudes 215°–290° W (Fig. 19b), where larger dark regions are located. At the same time, both the *Mariner-10* photograph (Fig. 19a) and the synthesized images of Mercury much more closely resemble the first quarter of the Moon (Fig. 19c) than the widely known and multiply published mosaic of *Mariner-10* photographs. The main reason is that the mosaic was created manually (Strom and Sprague 2003); the contrast of small features in the primary photographs was enhanced, and the boundaries of the photograph fields required alignment. This led to the suppression of the low spatial frequencies corresponding to the large structures shown in Figs. 15a and 15b. However, it may well be that there is another reason. The onboard memory is known to have failed during the operation of the *Mariner-10*

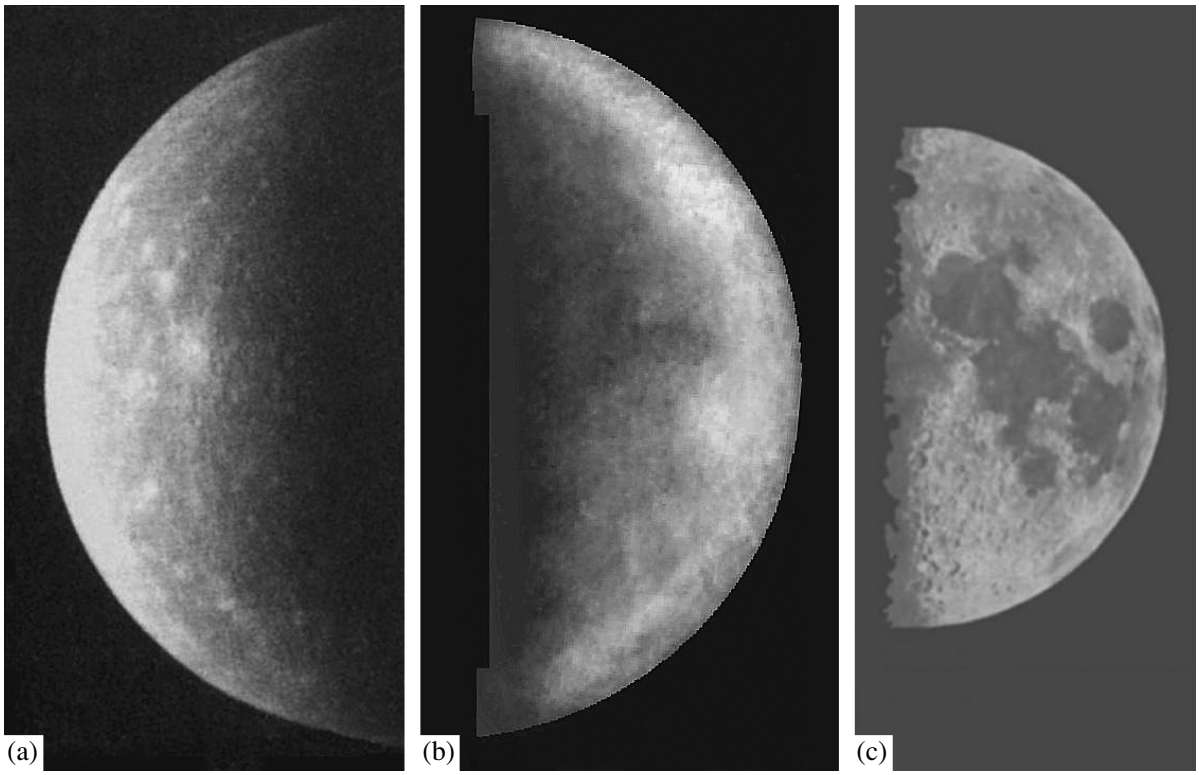

Fig. 19. (a) View of Mercury from the approaching *Mariner-10* spacecraft (from a distance of 1 million km). (b) Synthesized image of Mercury at phase 97°; (c) image of the Moon at phase 86°. The Moon's image was artificially blurred to the nominal sharpness of Mercury's image.

spacecraft near Mercury. Therefore, it was decided to switch over the video output of the Vidicon camera directly to the modulator of the radio transmitter; as a result, the images could be transmitted only in real time (Strom and Sprague 2003). It can be assumed that this led to a certain mismatch of the video channel frequency properties of the *Mariner-10* camera. In any case, the balance of spatial frequencies of the mosaic images was disrupted at least due to the manual processing. At the same time, the similarity of Figs. 15a and Figs 15b to the photograph in Fig. 19a taken by the *Mariner-10* camera at the beginning of its operation near Mercury on March 29, 1974, is quite obvious.

CONCLUSIONS

The above new images of the Mercurian surface together with Fig. 3c cover almost the entire part of the surface of the planet that was not photographed by the *Mariner-10* camera. To a first approximation, we can argue that extended relief features similar to dark basins appear to be distributed asymmetrically over the surface of Mercury. The same asymmetry is known to be observed on other terrestrial planes, on the Moon, and on many satellites of giant planets. On Mercury, dark basins concentrate mainly in the latitude range 210°–310° W.

The origin of the lunar relief asymmetry has peculiarities (Morota *et al.* 2005); nevertheless, it is quite appropriate to compare the Mercurian and lunar reliefs. If the Skinakas Basin and other dark regions in the longitude range 210°–290° W are typical of Mercury and if the nature of their formation and the accompanying thermal effects were actually similar to the lunar ones (Cintala 1992), then it remains unclear why their boundaries differ so sharply from the clear-cut outlines of the lunar lava maria (Fig. 19). The absence of sharp boundaries seems paradoxical. The relative impactor speeds in Mercury's orbit were almost a factor of 1.6 higher than those in the Earth/Moon orbit, while the collision energy was a factor of 2.5 higher. Therefore, one might expect the Skinakas Basin and other large dark structures to have outlines as sharp as the lunar basins and Caloris Planitia to be an exception. However, there are no such boundaries. The differences between Mercury and the Moon appear quite convincing and probably have deep physical causes. It can be assumed that the probable differences in the cosmogonic histories of the Mercurian and lunar surfaces rank first among these. Our synthesized images along with the *Mariner-10* photographs indubitably point to peculiarities of the physical properties of the Mercurian

surface at the maximum of its meteorite bombardment (Strom and Neukum 1988). In some measure, these peculiarities can be associated with the composition and, possibly, structure of the crust and mantle of this celestial body (Sprague *et al.* 2002; Strom and Sprague 2003; Ksanfomality 2001).

Finally, a conclusion that was mentioned previously (Ksanfomality 2002) should be repeated: the millisecond-exposure method in ground-based observations with a telescope with $D = 1.2–1.5$ m and $D/F = 1/10–1/20$ together with currently available data processing programs allow the previously unattainable resolution to be achieved on the surface of Mercury, 80 km or less. However, the PFS at a level of 0.85–0.90 rather than at the usual level of 0.7 should be used for this purpose. But this requires very large data sets and high-quality observational material.

ACKNOWLEDGMENTS

This work was supported by the Russian Foundation for Basic Research (project no. 04-02-16097). N.V. Gorshkova took part in the observational data processing. A number of auxiliary programs were written by E.V. Petrova. The AIMAP-225 code was placed at my disposal by V.O. Kakhiani before its publication. R. Stekelenburg kindly gave advice on using his AstroStack-1 code. G. Papamastorakis allocated me observational time on the telescope of the Skinakas observatory several times, despite the overloaded schedule of the instrument. All of them made a substantial contribution to this work.

REFERENCES

1. J. Baumgardner, M. Mendillo, and J. K. Wilson, Astron. J. **119**, 2458 (2000).
2. L. F. Burlaga, Planet. Space Sci. **49**, 1619 (2001).
3. M. J. Cintala, J. Geophys. Res. **97**, 947 (1992).
4. J. E. P. Connerney and N. F. Ness, *Mercury*, Ed. by F. Vilas, C. R. Chapman, and M. S. Matthews (Univ. Arizona Press, Tucson, 1988), p. 494.
5. R. F. Dantowitz, S. W. Teare, and M. J. Kozubal, Astron. J. **119**, 2455 (2000).
6. D. L. Fried, J. Opt. Soc. Am. **68**, 1651 (1978).
7. R. Grard and A. Balogh, Planet. Space Sci. **49**, 1395 (2001).
8. J. K. Harmon, P. J. Perillat, and M. A. Slade, Icarus **149**, 1 (2001).
9. J. W. Head III, *The New Solar System,* Ed. by J. K. Beatty *et al.* (Sky Publ. Corporation, London, 1981), p. 45.
10. R. E. Hufnagel, Proc. Natl. Acad. Sci. USA **3** (Suppl. 2), 11 (1966).
11. V. O. Kakhiani, *Astronomical Image Processor AIMAP-225* (2003) (unpublished).
12. R. M. Killen, T. A. Bida, and T. H. Morgan, Icarus **173**, 300 (2005).
13. L. V. Ksanfomality, Byull. Abastumansk. Astrofiz. Obs. **34**, 117 (1966).
14. L. V. Ksanfomality, Astron. Vestn. **32**, 133 (1998) [Sol. Syst. Res. **32**, 115 (1998)].
15. L. V. Ksanfomality, Astron. Vestn. **35**, 371 (2001) [Sol. Syst. Res. **35**, 339 (2001)].
16. L. V. Ksanfomality, Astron. Vestn. **36**, 291 (2002) [Sol. Syst. Res. **36**, 267 (2002)].
17. L. V. Ksanfomality, Astron. Vestn. **37**, 514 (2003) [Sol. Syst. Res. **37**, 469 (2003)].
18. L. V. Ksanfomality, Astron. Vestn. **38**, 23 (2004) [Sol. Syst. Res. **38**, 21 (2004)].
19. L. V. Ksanfomality, V. P. Dzhapiashvili, O. V. Kakhiani, *et al.*, Astron. Vestn. **35**, 208 (2001) [Sol. Syst. Res. **35**, 190 (2001)].
20. L. V. Ksanfomality, V. P. Dzhapiashvili, O. V. Kakhiani, *et al.*, Astron. Vestn. **36**, 366 (2002) [Sol. Syst. Res. **36**, 341 (2002)].
21. L. V. Ksanfomality and N. M. Shakhovskoĭ, Izv. Krym. Astrofiz. Obs. **38**, 264 (1967).
22. L. Ksanfomality, N. Thomas, and G. Papamastorakis, Planet. Space Sci. **53** (2005) (in press).
23. M. Mendillo, J. Warell, S. S. Limaye, *et al.*, Planet. Space Sci. **49**, 1501 (2001).
24. T. Morota, T. Ukai, and M. Furumoto, Icarus **173**, 322 (2005).
25. N. F. Ness, Space Sci. Rev. **21**, 527 (1978).
26. M. S. Robinson and G. J. Taylor, Meteor. Planet. Sci. **36**, 841 (2001).
27. C. T. Russel, D. N. Barker, and J. A. Slavin, *Mercury*, Ed. by F. Vilas, C. R. Chapman, and M. S. Matthews (Univ. Arizona Press, Tucson, 1988), p. 514.
28. M. Sarantos, P. H. Reiff, T. W. Hill, *et al.*, Planet. Space Sci. **49**, 1629 (2001).
29. A. L. Sprague, D. M. Hunten, and K. Lodders, Icarus **118**, 211 (1995).
30. A. L. Sprague, J. P. Emery, K. L. Donaldson, *et al.*, Meteor. Planet. Sci. **37**, 1255 (2002).
31. R. Stekelenburg, *AstroStack Manual (v. 0.90 beta)* (1999; 2000), http://www.astrostack.com/.
32. R. G. Strom and G. Neukum, *Mercury*, Ed. by F. Vilas, C. R. Chapman, and M. S. Matthews (Univ. Arizona Press, Tucson, 1988), p. 336.
33. R. G. Strom and A. L. Sprague, *Exploring Mercury the Iron Planet* (Springer Praxis, Chichester, UK, 2003).
34. N. J. Trask and J. T. Guest, J. Geophys. Res. **80**, 2461 (1975).
35. J. Warell, Icarus **156,** 303 (2002).
36. J. Warell, Icarus **161**, 199 (2003).
37. J. Warell and D. T. Blewett, Icarus **168**, 257 (2004).
38. J. Warell and S. S. Limaye, Planet. Space Sci. **49**, 1531 (2001).

Translated by V. Astakhov